

12-2011

# Characterization of Mesoporous Materials Via Fluorescent Spectroscopic Methods

Raymond Russell Kennard

Follow this and additional works at: <http://digitalcommons.library.umaine.edu/etd>

 Part of the [Membrane Science Commons](#)

---

## Recommended Citation

Kennard, Raymond Russell, "Characterization of Mesoporous Materials Via Fluorescent Spectroscopic Methods" (2011). *Electronic Theses and Dissertations*. 1745.  
<http://digitalcommons.library.umaine.edu/etd/1745>

This Open-Access Dissertation is brought to you for free and open access by DigitalCommons@UMaine. It has been accepted for inclusion in Electronic Theses and Dissertations by an authorized administrator of DigitalCommons@UMaine.

**CHARACTERIZATION OF MESOPOROUS MATERIALS VIA  
FLUORESCENT SPECTROSCOPIC  
METHODS**

By Raymond Russell Kennard

B.S. Ithaca College, 1999

A THESIS

Submitted in Partial Fulfillment of the

Requirements for the Degree of

Doctor of Philosophy

(in Chemical Engineering)

The Graduate School

The University of Maine

December 2011

Advisory Committee:

William J. DeSisto, Assistant Professor of Chemical and Biological Engineering, Co-advisor

Michael D. Mason, Assistant Professor of Chemical and Biological Engineering, Co-advisor

Douglas M. Ruthven, Professor of Chemical and Biological Engineering

Carl Tripp, Professor of Chemistry

Benjamin A. McCool, Senior Director of Engineering, Algenol Biofuels, Inc.

## THESIS ACCEPTANCE STATEMENT

On behalf of the Graduate Committee for Raymond R. Kennard, I affirm that this manuscript is the final and accepted thesis. Signatures of all committee members are on file with the Graduate school at the University of Maine, 42 Stodder Hall, Orono Maine.

---

Committee chair's signature, name, and title

(Date)

© 2011 Raymond Kennard

All Rights Reserved

## **LIBRARY RIGHTS STATEMENT**

In presenting this thesis in partial fulfillment of the requirements for an advance degree at the University of Maine, I agree that the Library shall make it freely available for inspection. I further agree that permission for “fair use” copying of this thesis for scholarly purposes may be granted by the Librarian. It is understood that any copying or publication of this thesis for financial gain shall not be allowed without my written permission

Signature:

Date:

**CHARACTERIZATION OF MESOPOROUS MATERIALS VIA  
FLUORESCENT SPECTROSCOPIC  
METHODS**

By Raymond Russell Kennard

Thesis Advisors: Dr. William J. DeSisto & Dr. Michael Mason

An Abstract of the Thesis Presented  
in Partial Fulfillment of the Requirements for the  
Degree of Doctor of Philosophy  
(in Chemical Engineering)  
December 2011

There are three components that need to be understood to create new porous membranes for industrial applications. 1.) To understand appropriate synthesis conditions to create a successful membrane system. 2.) To understand how the microstructures generated in synthesis affect the transport properties of that system. 3) To be able to characterize the heterogeneity of the fabricated membrane's transport and physical structure.

Presented within this manuscript are new characterization methods to increase the understanding in membrane technology. It will be demonstrated that the novel application of standard fluorescent methods and the development of new fluorescent methods techniques allows for the measurement of molecular interactions and transport properties on length scales capable of providing valuable information in the field of membrane science, as well as expanding new applications in fluorescent techniques.

## **DEDICATION**

This thesis is dedicated to my family and friends who have supported me in every step throughout my education, without whose support none of this could be done. To my parents for always pushing me to do my best and not accepting anything less of me. To my all of my children (Alex, Gabby, Rosie, Rowan, and Chris) for their unconditional love, support, and understanding for the times, I had to make school and work a priority over them. To the love of my life (Tam), there are not words that can express my thanks for everything you have done to make my life better. Finally to all of my friends for your support during some of the toughest times in my life,

Thank you

## **ACKNOWLEDGEMENTS**

Prof. William DeSisto, Prof Michael Mason for your mentorship in my academic career and their advice. Prof. Douglas Ruthven for guidance and instruction. Prof. Carl Tripp for your patience and understanding throughout this process. Dr. Benjamin McCool for your mentorship during your time here in Prof. DeSisto's and Prof. Tripp's laboratories. In addition, thank you all for serving on my thesis committee.



## TABLE OF CONTENTS

DEDICATION .....	iv
ACKNOWLEDGEMENTS .....	v
LIST OF TABLES .....	xi
LIST OF FIGURES .....	xii
LIST OF ALPHABETICAL SYMBOLS .....	xv
LIST OF GREEK SYMBOLS .....	xviii
LIST OF SUBSCRIPTS .....	xx
1. INTRODUCTION .....	1
1.1. Thesis Outline .....	2
2. MEMBRANES .....	5
2.1. Inorganic porous membranes .....	7
2.2. Inorganic membrane modification .....	9
3. TRANSPORT PHENOMENA .....	12
3.1. Viscous Flow .....	13
3.2. Molecular Flow .....	13
3.3. Knudsen Flow .....	14
3.4. Surface Diffusion .....	15
3.5. Adsorption Dynamics .....	16
3.6. Capillary Condensation .....	19
3.7. Hindered Diffusion .....	19
3.8. Summary .....	21

4. CHARACTERIZATION .....	22
4.1. Static Methods .....	22
4.1.1. SEM and TEM .....	22
4.1.2. Radiation Scattering .....	23
4.1.3. Infrared .....	24
4.1.4. Porosimetry .....	25
4.2. Dynamic Methods .....	28
4.2.1. Bubble Point .....	28
4.2.2. Gas Permeability .....	28
4.2.3. Wicke-Kallenbach .....	30
4.2.4. Permporometry .....	31
4.3. Limitations .....	33
5. FLUORESCENCE .....	35
5.1. Fluorescent molecules .....	38
5.2. Fluorescence properties .....	40
5.3. Fluorescent Microscopy .....	43
5.3.1. Microscopic resolution .....	43
5.3.2. Kohler Illumination .....	46
5.3.2.1. Fluorescence Recovery After Photobleaching .....	48
5.3.2.2. Fluorescence Photoactivation Localization Microscopy .....	49
5.3.3. Confocal Imaging .....	51
5.3.3.1. Single-Molecule Imaging Spectroscopy .....	53
5.4. Summary .....	54

6. CHARACTERIZATION OF INORGANIC POROUS MEMBRANES VIA SINGLE MOLECULE IMAGING SPECTROSCOPY .....	55
6.1. Chapter Abstract .....	55
6.2. Introduction .....	56
6.3. Experimental.....	59
6.3.1. Sample Preparation .....	59
6.3.2. Preliminary Fluorescence studies .....	61
6.3.3. Instrument .....	66
6.4. Data Handling.....	69
6.5. Model and Simulation.....	73
6.6. Results and Discussion .....	75
6.7. Conclusions .....	90
7. HIGH RESOLUTION SPACIAL MAPPING OF SURFACE FEATURES OF MESOPOROUS SILICA MEMBRANES VIA FLUORESCENT PHOTOACTIVATION LOCALIZATION MICROSCOPY .....	92
7.1. Chapter Abstract .....	92
7.2. Introduction .....	92
7.3. Experimental.....	94
7.3.1. Instrument .....	94
7.3.2. Sample Preparation .....	96
7.4. Analysis .....	97
7.5. Conclusion .....	103

8. DEVELOPMENT OF A TIME-RESOLVED FLUORESCENCE IMAGING	
METHOD TO MEASURE CONCENTRATION PROFILES THROUGH	
POROUS MEMBRANES .....	104
8.1. Chapter Abstract .....	104
8.2. Introduction .....	104
8.3. Experimental.....	108
8.3.1. Instrument .....	108
8.3.2. Software Written.....	109
8.3.3. Photobleaching Nanopure Water .....	111
8.3.4. Sample Preparation .....	111
8.3.5. Method .....	112
8.4. Analysis .....	116
8.5. Discussion.....	119
8.6. Conclusions .....	120
9. BREAKTHROUGH CURVES OF UNMODIFIED ANODICS AND	
ATOMIC LAYER DEPOSITSION MODIFED ANODISC VIA TIME-	
RESOLVED FLUORESCENCE MICROSCOPY.....	121
9.1. Chapter Abstract .....	121
9.2. Introduction .....	121
9.3. Application of the Solution for Transient Diffusion in a Parallel-Sided Slab .....	123
9.4. Hindered Diffusion .....	126
9.5. Experimental Section.....	128
9.5.1. Atomic Layer Deposition of Anodic Alumina Membranes .....	128
9.5.2. Fluorescence Measurements .....	129

9.6. Results and Discussion .....	129
9.6.1. Parallel Sided Slab .....	129
9.6.2. Hindered Diffusion .....	130
9.6.3. Lag-Time Analysis.....	136
9.7. Conclusions .....	137
10. SUMMARY AND FUTURE WORK.....	140
10.1. Summary.....	140
10.2. Future Work.....	141
BIBLIOGRAPHY .....	143
APPENDICES .....	157
Appendix A: Patent Application.....	157
Appendix B: Receipt of Patent Application.....	169
Appendix C: Labview Wiring Diagram.....	172
Appendix D: Mathamatica Code .....	173
Appendix E: Lag-Time Analysis .....	179
BIOGRAPHY OF THE AUTHOR.....	182

## **LIST OF TABLES**

Table 3-1 A summary of some transportive theories important to porous membranes. ....	12
Table 9-1 Summary of all measured and calculated diffusivities. ....	132
Table 9-2 Adsorption capacities predicted by various models. ....	135
Table. E.1 Summary of the lag time analysis. ....	181

## LIST OF FIGURES

Figure 2.1 An example of a symmetric track etch membrane. ....	8
Figure 2.2 Schematic of an asymmetric membrane with a heterogeneous morphology.....	9
Figure 2.3 A schematic depicting the chemical process to create a templated mesoporous membrane. ....	11
Figure 4.1 The dependence of pressure on pore size required for mercury porosimetry.....	25
Figure 4.2 Diagram of a Wicke-Kallenbach cell .....	30
Figure 4.3 Typical permporometry system .....	31
Figure 4.4 Shows the potential pore geometries.....	32
Figure 4.5 Demonstrates the pore size dependence of capillary condensation.....	32
Figure 5.1 A Jablonski diagram. ....	36
Figure 5.2 A Jablonski diagram for fluorescence and phosphorescence .....	37
Figure 5.3 Examples of fluorescent molecules. ....	39
Figure 5.4 Depiction of how the Stoke shift is produced.....	41
Figure 5.5 A point spread function representing a cross-sectional view of an Airy disc.....	44
Figure 5.6 Diagram showing the half angle for two microscope objectives.....	46
Figure 5.7 A ray diagram depicting Kohler illumination.....	47
Figure 5.8 A diagram showing how a FPALM constructs a high resolution image.....	50
Figure 5.9 A cartoon showing the components of a confocal imaging microscope. ....	52
Figure 6.1 The molecular structure of the fluorescent dye used. ....	61
Figure 6.2 A figure showing the two sample orientations for imaging .....	63
Figure 6.3 An example of successive step photobleaching experiments. ....	64
Figure 6.4 An example image showing single molecule features.....	64
Figure 6.5 An example image of a defect area image in two orthogonal polarizations.....	65
Figure 6.6 A 2-D histogram showing the various polarization states of DIIC <sub>18</sub> within a defect area in a silica membrane.....	66

Figure 6.7 Schematic of the two channel laser scanning confocal microscope .....	68
Figure 6.8 An example image via raster scanning to locate single molecule features.....	69
Figure 6.9 Screen capture of the VIs front panel. ....	71
Figure 6.10 An example Polarization time course .....	72
Figure 6.11 A 2-D histogram of the polarization values versus the total counts .....	72
Figure 6.12 A physical picture of the random walk on a sphere model.....	73
Figure 6.13 1D histograms of DiIC18 dry on glass .....	79
Figure 6.14 2D histograms of total intensity in counts. ....	82
Figure 6.15 Normalized polarization histograms.....	85
Figure 6.16 Model generated polarization histograms.....	87
Figure 6.17 Comparison of the average polarization vs. $1/\Delta T$ . ....	88
Figure 6.18 Henry's law fit to data. ....	89
Figure 7.1 Diagram of the FPLAM microscope .....	94
Figure 7.2 Molecular structure of fluorescein.....	96
Figure 7.3 Sample FPALM images. ....	98
Figure 7.4 Shows two surface morphologies of mesoporous silica thin films.....	99
Figure 7.5 The resulting plot for the radial distribution analysis for two samples. ....	100
Figure 7.6 Sample photobleaching response of a fluorescent molecule. ....	102
Figure 7.7 Shows the observed bleaching phenomenon .....	102
Figure 8.1 A suggested analysis and breakdown of an image for quality control. ....	107
Figure 8.2 Diagram of the inverted wide field fluorescent microscope.....	108
Figure 8.3 Shows the of components needed for the creation of a sample to be studied.....	111
Figure 8.4 Show examples of defect areas.....	113
Figure 8.5 Depiction of the fabricated sample system.....	114
Figure 8.6 The mean intensity of each versus time in minutes for 340nM of fluorescein.....	116
Figure 8.7 The observed raw averaged diffusion breakthrough curves. ....	119



Figure 9.1 Depiction of the membrane system. ....	124
Figure 9.2 The plot shows the corrected diffusion data. ....	130
Figure 9.3 Plot showing two breakthrough curves.....	134
Figure 9.4 Theoretical curves showing the increase of equilibrium times.....	136
Figure 9.5 How ALD may increase adsorption site density and reduce surface area.....	138
Figure. E.1 Resulting plot of time-lag analysis for short time approximate solutions.....	180

## LIST OF ALPHABETICAL SYMBOLS

F	viscous permeation ( $\text{mol/m}^2 \text{ s Pa}$ )
J	flux ( $\text{mol/m}^2 \text{ s}$ )
$\Delta P$	pressure across the membrane (Pa)
r	the nominal pore radius (m)
R	the ideal gas constant
T	temperature (K)
L	the thickness of the membrane (m)
$P_m$	mean pressure across the membrane (Pa)
C	the concentration of the diffusing species
Z	the distance the diffusing species travels
D	diffusivity ( $\text{cm}^2/\text{s}$ )
M	the molecular weight (kg/mol)
q	the moles of gas adsorbed per kilogram of adsorbent (mol/kg),
$K_H$	the Henry's constant (mol/Pa kg)
P	number of adsorbate particles
$S^*$	the number of available adsorption sites
SP	the number of occupied sites
$K_{eq}$	the reaction equilibrium constant
$\Delta H$	the change in heat of adsorption from temperature one to temperature two
x	the ratio between the pressure of the adsorbate in the gas phase and the saturation pressure at the experimental conditions
c	the BET constant

$P_r$	reduced vapor pressure (Pa)
$V_m$	the molar volume of the liquid at standard temperature and pressure
$D_\infty$	the diffusivity of a solute particle in a dilute bulk solution
$k$	the Boltzmann constant
$r_s$	the solute's hydrodynamic radius.
$H$	hydrodynamic hindrance factor
$d$	the pore diameter
$t$	the monolayer thickness of the adsorbate
$F$	permeation
$M_w$	molecular weight of a gas
$f(r)$	the number of pores per unit volume with a pore radius from $r$ to $r + dr$
$v$	the Knudsen velocity
$F(\rho)$	the total flux of the inert gas as a function of radii
$l$	the thickness of the membrane
$E$	energy of the adsorbed photon
$h$	Plank's constant
$S_0$	the energy of the ground state
$S_1$	the energy of the unstable excited state
$R$	the minimum resolution
N.A.	Numerical aperture
$n$	index of refraction
$r_0$	standard deviation of the point spread function
$N$	the total number of photons or events
$q$	the size of an image pixel

$b$	the background noise for a pixel
$x, y, z$	vector components of a ray trap within a sphere
$\Delta t$	the observation time
$V$	the molecular volume
$P$	the polarization
$p$	the probability of an occurrence
$\Delta S$	Change in entropy
$L$	length
$t$	time
$A$	cross-sectional area
$I(t)$	the emission intensity observed at time $t$
$I_0$	excitation energy
$A_0$	the molecular quantum efficiency
$y_0$	the background fluorescence of the system.
$EB(t)$	the time-dependent extent of bleaching
$Z_g$	location of the focal plane of the cover slip
$Z_b$	bottom of the Anodisc
$Z_t$	the top of the Anodisc
$r_p$	the pore radii
$M_\infty$	loading capacity

## LIST OF GREEK SYMBOLS

$\varepsilon$	porosity (defined as the void area divided by the total cross sectional area)
$\eta$	fluid dynamic viscosity (Pa s)
$\tau$	tortuosity of the pore (defined as the pore length divided by the thickness of the membrane)
$\theta_k$	Knudsen shape correction factor.
$\theta^*$	the loading of the surface (the surface concentration divided by the saturation capacity).
$\theta$	the contact angle
$\alpha$	the Langmuir constant
$\sigma_s$	the liquid surface tension
$\Psi$	the contact angle
$\Phi$	the partition coefficient $(1-r_s/r_p)^2$
$\bar{\theta}$	angular distribution
$\lambda$	the wavelength of radiation
$\gamma$	the surface tension at the liquid air interface
$\alpha^*$	ideal separation factor
$\lambda$	wavelength
$\nu$	frequency of a photon
$\rho$	pore size
$\nu_{ex}$	the frequency of the excitation photon

$\Theta$	azimuthal angle
$\Phi$	polar angle
$\overline{\Delta\theta}$	angular displacement
$\rho$	molecular surface density
$\tau_r$	anisotropic reorientation times
$\eta(T)$	temperature dependent solvent viscosity
$\Phi_{\text{ext}}$	the external collection efficiency
$\tau$	the emission lifetime of a molecule
$\beta$	a fitting parameter for a stretched exponential (ideally 1)
$\delta$	thickness
$\phi$	partition coefficient
$\lambda$	ratio of the solute radii to pore radii

## LIST OF SUBSCRIPTS

v	viscous flow
m	molecular flow
k	Knudsen flow
eff	effective (usually in regards to diffusivity)
s	surface flow
sat	capacity at saturation
1	refers to species one
2	refers to species two
P	refers to the pore
k	Kelvin radii
v	void volume
g	glass
t	top
b	bottom
a	Anodisc
0	initial
h	estimations using hindered diffusion models
f	fluorescent measured

## 1. INTRODUCTION

Ideal porous membranes have the potential to provide beneficial and significant impact on industrial scale separation and purification systems. They have the ability to reduce energy consumption, and increase efficiency when compared to distillation and cryogenic separations. With the exception of polymer membranes for reverse osmosis<sup>1</sup>, they have been difficult to implement on a large scale. In order for membrane systems to meet the requirement for industrial applications, they must demonstrate highly selectivity, high flow rates, high operating pressures, and long-term stability. Although porous membranes can theoretically meet these requirements, they are not yet been realized. Defect free inorganic porous membranes are difficult to make on industrially significant scales. One of the challenges prohibiting the fabrication of these membranes is the lack of understanding how synthesis conditions affect both the microscale heterogeneity and, the transport properties. Currently, significant amount of research effort has been invested into porous membrane synthesis; characterization, coupled with intensive modeling, to understand how the areas of synthesis, microscale heterogeneity, and transport behavior are linked.

All characterization methods for nanoporous membranes are limited in their ability to measure local heterogeneity and defect quantification on the nanometer scale, while simultaneously monitoring their effect on transport processes. Techniques, such as Scanning Electron Microscopy (SEM) or Transmission Electron Microscopy (TEM) are capable of mapping surface morphologies with theoretical resolution cutoffs down to 42pm<sup>2</sup>. These methods are cost prohibitive and are incapable of measuring transport dynamics. While there are numerous methods to determine the transport properties of porous membranes, they are incapable of simultaneously measuring membrane physical and chemical heterogeneity. Often several characterization techniques are used in conjunction with one another to correlate bulk transport properties to structural features and conclusions are drawn about the membranes' performance and based on its physical structure. Quantification of transport property heterogeneity is not



possible with existing methods yet this information is critical to furthering membrane development and application.

Fluorescent microscopy has been utilized to image and monitor biological systems since the 1970's<sup>3</sup>. It was only recently, fluorescent microscopy has been applied to imaging and characterizing inorganic porous membranes<sup>4-7</sup>. This thesis presents a novel solution to the characterization challenge by developing and implementing fluorescent spectroscopic methods that are capable of simultaneously mapping porous membrane heterogeneity and measuring transport behavior on the nanometer length scale. These techniques are ripe for the development and application to improve our understanding of how surface heterogeneity of porous membranes affects transportive properties.

## **1.1. Thesis Outline**

CHAPTER 2 provides a background summary of membranes. It contains a brief description of the types of membranes based on their chemical composition, with a more detailed discussion of inorganic membranes types and a discussion of classification by pore sizes and the chemical modification of these membranes.

CHAPTER 3 provides a background summary of major diffusion properties; adsorption dynamics, capillary condensation, and hindered diffusion that are known to occur in inorganic membranes used to describe the transport phenomena observed in porous media.

CHAPTER 4 provides a background of the application of transport phenomena and techniques for the characterization of porous inorganic membranes along with a brief discussion of electron microscopy, radiative scattering, and infrared spectroscopy techniques.

CHAPTER 5 provides a background summary of fluorescence. It contains a description of the quantum mechanical explanation for fluorescent behavior, and the application of fluorescent characterization methods.

CHAPTER 6 demonstrates the use of single molecule imaging spectroscopy to characterize, quantitatively, the interaction between a probe molecule and the interior of the pore within mesoporous silica membranes. This approach is radically different from typical membrane characterization methods; in that, it has the potential to sample, spatially, the underlying pore structure distribution, the surface energy, and the transport properties without “averaging”. It allows for the characterization of a membranes’ transport mechanism and the ability to sub divide its bulk transport mechanism into individual components that can be assigned to specific morphologies. The potential use of this new fundamental knowledge can be quantitatively linked to both the preparation and the performance of membranes leading to the advancement of membrane science and technology.

CHAPTER 7 discusses the setup and application of fluorescence photoactivation localization microscopy (FPALM) to measure intrinsic physical properties of inorganic mesoporous membranes. This novel method allows for the spatial mapping below the optical diffraction limit with the use of common instrumentation. Utilizing a specific class of fluorescent probes, FPALM is capable of creating images in the visible spectrum below 100nm<sup>8-10</sup>. Additionally, since the system utilizes a probe molecule to perform the mapping, there is a potential to couple high resolution mapping with molecular and transportive characterization.

CHAPTER 8 discusses the development of a simple fluorescence imaging method for measuring time-resolved concentration of a fluorescent molecule diffusing through an anodic alumina membrane. The membrane used has a pore diameter of 20 nm, allowing the measurement of the diffusion constants of the fluorophore molecules within a liquid-filled pore. The change in signal was correlated to concentrations commensurate with single molecule detection. The ability to measure these parameters, simply, on a microscale has potential applications to further the understanding the link between the intrinsic properties of a membrane and its overall performance. This method can easily be applied in quality control for industrial processes.

CHAPTER 9 expands on the capabilities of the technique developed in chapter 8 by measuring diffusion constants for 20nm, 100nm, 200nm, and ALD modified Anodiscs, as well as improves the mathematical model used to describe the diffusional break through curves for the extraction of adsorption capacities.

CHAPTER 10 is a review of this manuscript and suggested future work for expanding the application of fluorescent techniques to characterization of porous nanomaterials.

It should be noted that chapter 6 and 8 were previously submitted and accepted for publication. Chapter 6 appears in the Journal of Chemical Physics and appears in the Virtual Journal of Biological Physics Research. Chapter 8 appears in Applied Physics Letters. It is also noted that Chapters 8 and 9 are included in patent application number 61/372,593 on 08/11/2010, which is shown in Appendix A and Appendix B. Finally, Chapter 9 will be submitted to the Journal of Membrane Science for publication.

## 2. MEMBRANES

A membrane can be defined as a semipermeable layer of a material which is a separating barrier between two different phases and is permselective to specific particles, molecules, ions or substances when exposed to a driving force, via normal diffusion or facilitated diffusion<sup>11, 12</sup>. Some examples may include biological membranes, such as can be found in the cells of animals or plants, a polymer membrane synthesized using organic polymeric materials, or inorganic metal oxide ceramic porous or dense membranes. Porous membranes have three different classifications based on their nominal pore size; microporous ( $\leq 2$  nm), mesoporous ( $\geq 2$  nm but  $\leq 100$  nm), and macroporous ( $\geq 100$  nm).

Although biological membranes are extremely fragile and require an environment that mimics their natural surroundings to survive and operate, they possess some characteristics and performance capabilities that synthetic membrane technology attempts to achieve. Biological membranes utilize facilitated diffusion and osmosis via enzymatic pumps and controlled pores that are specifically designed to allow, only a specific chemical or class of materials to cross from the outside world into the cytoplasm of a living cell. Generally, an electrical gradient is the driving force for the action of the transport. A well-known example of this transport specificity is the Blood-brain barrier membrane. The blood brain barrier allows only a small group of compounds to cross its barrier, such as monocytes. This barrier forms a virtually impregnable protective layer for the neurological system; unfortunately, there exist cases where the specificity of the blood brain barrier becomes a severe deficit. The challenge with a membrane that is as specific as that of the blood brain barrier is demonstrated when one attempts to treat a viral infection of the central nervous system pharmaceutically; one case where this becomes evident is in the treatment of the Human Immunodeficiency Virus (HIV). Although, currently there are pharmaceuticals available capable of destroying HIV from most of the human anatomy; HIV has the means to cross the blood brain barrier, making it nearly unreachable by pharmaceutical treatments. It is believed that latent HIV can cross the blood brain barrier inside monocytes. This

idea is known as the *Trojan horse theory*<sup>13, 14</sup>. Once inside, the monocytes become active and release the virus into the brain tissue<sup>15</sup>, making it unattainable for eradication. Although, HIV and other nefarious viruses have found intelligent ways to ‘trick’ and take advantage of the specificity of biological membranes; ongoing medicinal chemistry research is looking for compounds that will not only destroy the virus but also be able to transport themselves across the membrane<sup>16</sup>. It is the specificity biological membranes that all industrial synthetic membrane applications attempt to achieve. Ideally, industrial applications would use this to create a membrane process to allow for specific separation of single chemical components from a mixture, like the separation of carbon dioxide gas from methane gas.

Currently, commercial membranes that are as specific as those found in biological systems do not exist. Two other classes of membranes are commercially available: polymeric and inorganic. They have several advantages over classical distillation and bulk liquid and gas phase chromatographic methods for separations, in that they have lower energy operation requirements, can be simpler to use, and have the potential for higher selectivity. However, they also lack the specificity found in biological membranes. There are also distinct disadvantages to each of the two membrane classes.

Polymeric membranes have been available for the last 40 years<sup>1</sup>. These materials still retain the bulk of the industrial market due to the relative simplicity of fabrication and low cost of starting materials<sup>17</sup>. They have successfully been applied to separation processes in areas such as wastewater treatment, seawater desalination, gas separation, and blood serum treatment. In addition, they are used in water filtration systems equipped with a reverse osmosis. membranes have been gathering interest in areas of biomedical and biotechnological applications<sup>17</sup>. One of the deficits of polymeric membranes is that they degrade readily at high temperatures and are limited in their ability to operate outside a small pH range near 7. For some applications, the disadvantages of polymer membranes can be overcome by the use of inorganic and metal oxide membranes.

Inorganic and metal oxide membranes have their own unique limits as well. Although inorganic membranes are thermally and chemically stable compared to polymer-based membranes, they are cost prohibitive to fabricate on a large industrial scale. Physically, they are brittle and lack the mechanical strength to prevent fracturing at high pressures. In this thesis; specific types of inorganic membranes, their transport properties, characterization techniques, and applications and developments of unique fluorescent characterization methods will be addressed.

## **2.1. Inorganic porous membranes**

Inorganic and polymeric porous membranes are broken down into two categories based on the physical architecture of the system, symmetric and asymmetric. Symmetric membranes, also known as homogeneous membranes, have the same physical porous structure throughout the entire material and exhibit the same transport properties within the system<sup>1, 11</sup>. An example of a symmetric membrane is an Anopore® track etched membranes known as an Anodiscs (Figure 2.1). Anodiscs are comprised of straight channel pores with a very narrow pore size distribution. The challenge for these membranes in industrial processes is two competing factors, physical strength to withstand high pressures and high permeability. In order for these materials to be economically sound for industrial applications, the system must be able to operate at high pressures and generate high flow rates of high value products. To have enough mechanical strength for high-pressure separation processes, these materials need considerable thickness. Conversely, to achieve the desired flow rates, i.e. the permeability, the transport flux of material through the membrane per unit driving force per unit membrane thickness; must be high as well. The permeability is indirectly proportional to the path length of the porous structure. To achieve high flow rates, ideal membrane systems should be as thin as possible. These two competing factors are often difficult to balance and make symmetric membranes impractical for large-scale industrial separation processes. One solution to this challenge is to apply an asymmetric membrane.

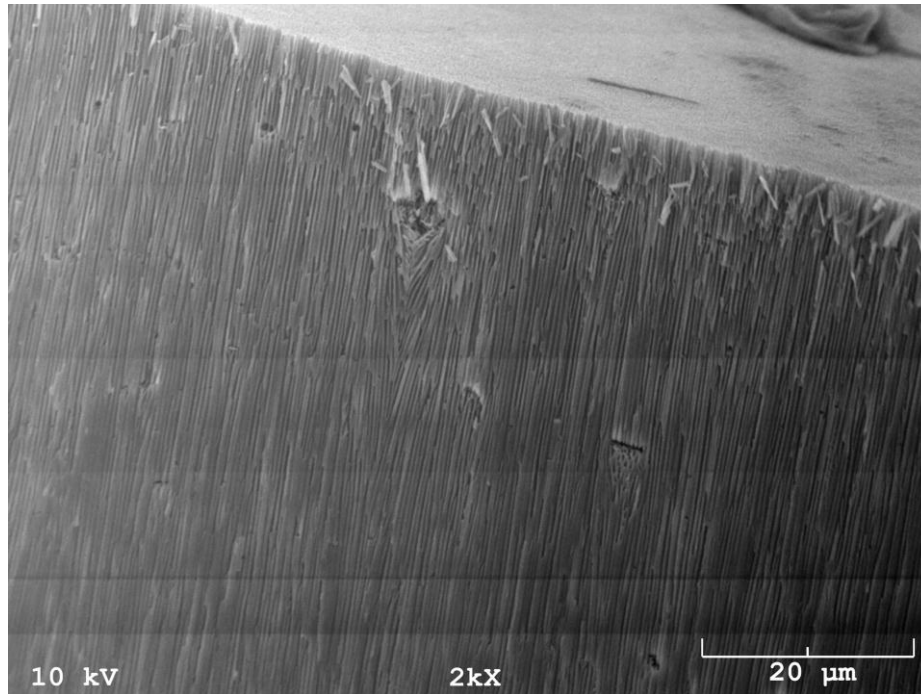


Figure 2.1 An example of a symmetric track etch membrane. With homogeneous morphology. A supporting layer of a 0.02 μm Anodisc.

An asymmetric membrane is defined as a membrane that is made of two or more layers of porous structures that have different morphologies<sup>1, 11</sup> (Figure 2.2). Where the mechanical strength comes from a thick layer of large pore sizes that possess a low flow resistance and where each subsequent layer is decreasing in pore size and thickness and the top layer is the active separation layer.

Asymmetric membranes compensate for the limits of a symmetric membrane giving both low flow resistance and high mechanical strength. The complex structure can be demanding to fabricate. Because of the variability of permeability, understanding the flow dynamics can be equally demanding. Generally the top active layer is assumed to play the dominant role in the expression of the membranes' transport processes. However, this may not always be the case especially when support layers are considerably thick or close to the pore size of the active layer.

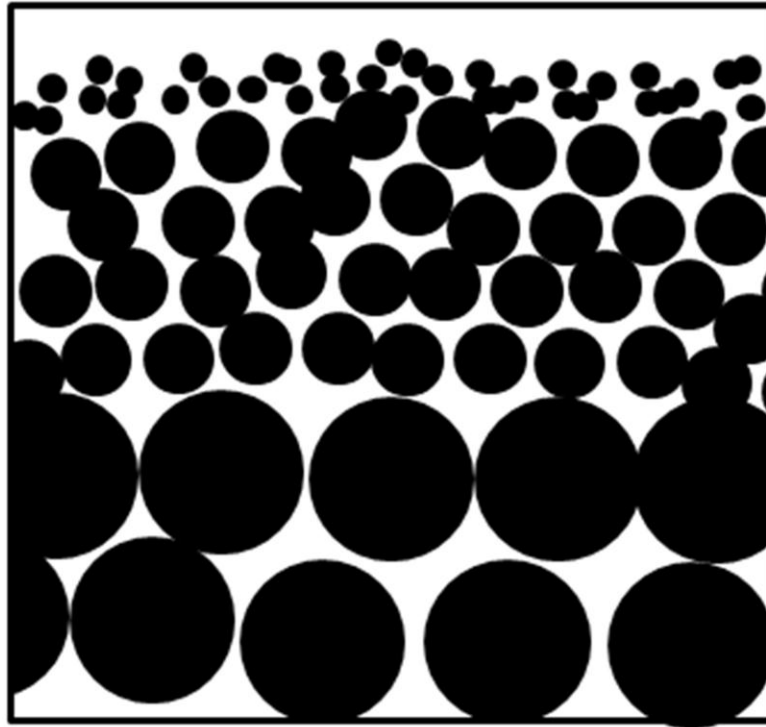


Figure 2.2 Schematic of an asymmetric membrane with a heterogeneous morphology.

Material choices and chemical properties of both symmetric and asymmetric membranes are limited. To obtain a larger selection of materials for separations, modification methods have been developed. These modifications can be as simple as a single coating on the outer surface to change the adsorptive behavior of the system, or as complex as to be repeated to heal defects or physically reduce the average pore size.

## **2.2. Inorganic membrane modification**

Modification methods have been developed to create new surface chemistries to change adsorption/desorption dynamics and the physical structures of inorganic membranes. Chemical Vapor Deposition<sup>18, 19</sup> (CVD), and Atomic Layer Deposition<sup>19-21</sup> (ALD) are two modification methods that are similar in that they change the physical and chemical properties of the whole membrane. CVD and ALD methods are usually performed via gas phase reactions that attach



new chemical surfaces to a preexisting structure. Each method requires careful selection of reactants and control of conditions for the production of the desired modification. The difference between CVD and ALD is that in CVD, the reactants are introduced and continually fed into the system for predetermined amount of time to achieve the desired modification. In ALD, reactants are introduced in a stepwise process, referred to as cycles, to grow one “atomic” layer at a time. The purpose of ALD over CVD is that the modification or reduction of pore size can be better controlled. While each of these can achieve similar results, it can be difficult to control the extent of reaction that occurs with CVD. An appropriate ALD method may have the ability to tune to a specific pore size reduction. It is challenging to find the correct combinations of precursors to avoid self-polymerization reactions. Using the ALD method can also be very time and material intensive.

Another approach to modify an existing membrane for separations is adding a new active layer on top of the preexisting system via sol-gel chemistry<sup>22</sup>. Sol-gel modifications have been proven to be an effective process to modify inorganic membranes and nanoporous materials<sup>23</sup>. General methods begin with formation of the gel, consisting of metal organics or metal salts, to form the backbone structure of the final material. The metal-containing compounds are mixed with solvent, and in some cases, surfactants. The surfactant is added to the sol at a critical concentration to form micelles. Once the sol-gel mixture is complete, the sol-gel can be dip coated or spin coated onto the inorganic membrane. When the supporting membrane is coated, the sol-gel is allowed to age and dry onto its support. It is during this drying process that polymerization of the metal-containing compounds occur and form a new metal oxide layer. If the sol-gel contains surfactants, the micelles collect together to form an organic structure encased in a metal oxide matrix. After the drying process has been completed, this new membrane system is sintered to complete the condensation of any hydroxyl groups present and stabilize the metal oxide backbone further. It is during this sintering step that the organic surfactants are removed via a decomposition reaction. In sol-gels without surfactant templating, a microporous structure

is created within the metal oxide matrix with pore sizes smaller than 2 nm. In surfactant templated sol-gels, the removal of the surfactants from the sol-gel matrix leaves behind a structure with a larger average pore size than that found in the sol-gel matrix itself, Figure 2.3.

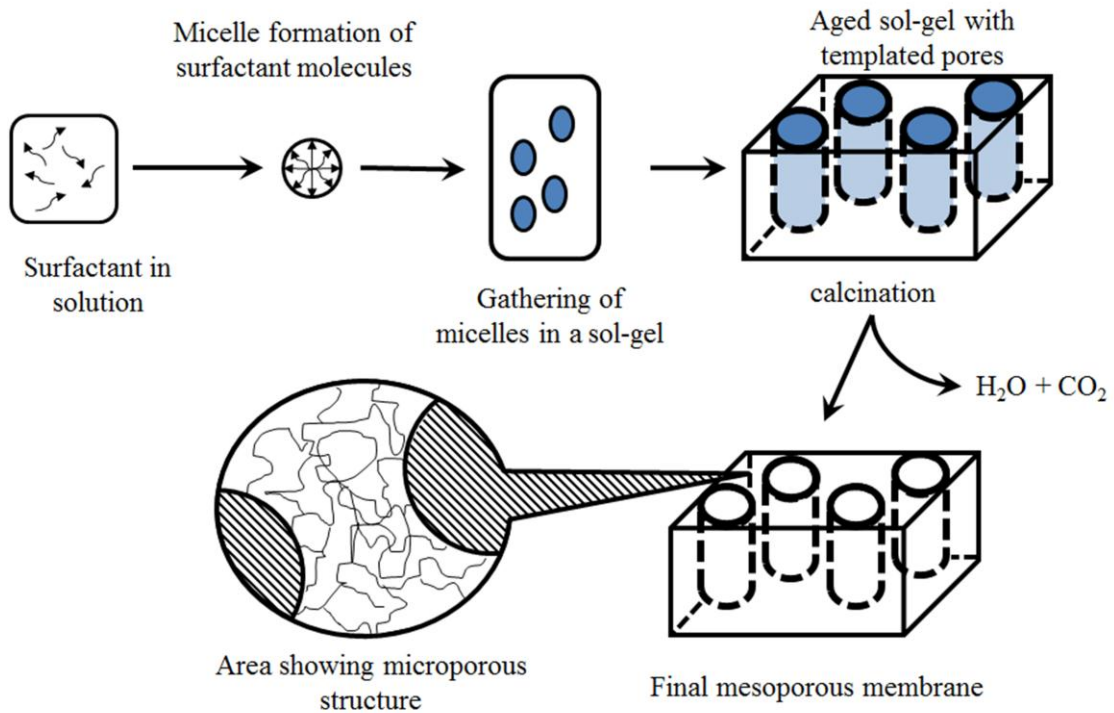


Figure 2.3 A schematic depicting the chemical process to create a templated mesoporous membrane.

While sol-gel chemistry is a very effective method to modify an inorganic membrane for specific needs and applications, defect free and continuous sol-gel layers can be very difficult to achieve. Sol-gel chemistry requires control and monitoring of numerous parameters, i.e. concentrations, purity of precursors, and ambient humidity. They are also dependent upon drying conditions and require a dust free synthesis environment. Unlike track-etched membranes, these active layers can be very heterogeneous with large pore size distributions. A variety of transport properties can be observed in conjunction with one another.

### 3. TRANSPORT PHENOMENA

Inorganic membranes obey transport laws and demonstrate a number of properties based on their pore sizes, physical and chemical composition, and the interactions between the pore wall and the diffusing species. Some of the transport phenomena can be described by the following theories: micropore diffusion ( $\leq 1.5$  nm), Knudsen flow (2 - 100 nm), molecular diffusion ( $\geq 10$  nm), and viscous flow ( $\geq 20$  nm). Each of these theories will be discussed in detail below and a representation of the interactions between the pore wall and the diffusing species is shown in Table 3-1. It is important to note that all membranes studies fall within the Knudsen regime.


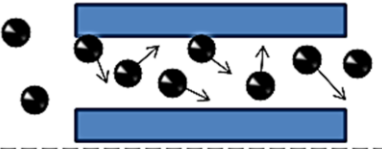
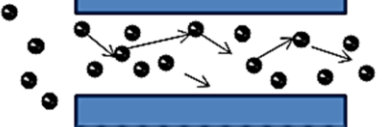
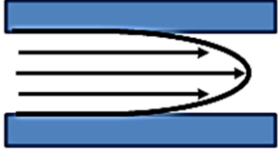
	Nominal pore size (nm)	Representation
Microporous Flow	$\leq 1.5$	
Knudsen Diffusion	2 – 200	
Molecular Diffusion	$\geq 10$	
Viscous Flow	$\geq 20$	

Table 3-1 A summary of some transportive theories important to porous membranes.

### 3.1. Viscous Flow

Viscous flow occurs when the pore radii are much larger than the mean free path of a gas and the gas molecules are treated as a bulk fluid. This allows for no separation of individual components of a fluid mixture. However, accounting for viscous flow can be important within macroporous supporting layers of asymmetric membranes and can have significant impact on the total flow and resistance of the system. At steady state, assuming the fluid velocity within a capillary is laminar and a velocity of zero at the pore walls; no slip boundary condition, the molar flux can be expressed using Hagen-Poiseuille law<sup>24</sup>.

$$\text{Equation 3.1} \quad F_v = -\frac{J_v V}{\Delta P} = \frac{\varepsilon}{8\eta\tau} \frac{r^2}{RTL} P_m$$

Where  $F_v$  is the viscous permeation ( $\text{mol/m}^2 \text{ s Pa}$ ),  $J_v$  is the viscous flux ( $\text{mol/m}^2 \text{ s}$ ),  $\Delta P$  is the difference in pressure across the membrane,  $\varepsilon$  is the porosity (defined as the void area divided by the total cross sectional area),  $\eta$  is the fluid's dynamic viscosity ( $\text{Pa s}$ ),  $\tau$  is the tortuosity of the pore (defined as the pore length divided by the thickness of the membrane),  $r$  is the nominal pore radius (m),  $R$  is the ideal gas constant,  $T$  is the temperature (K),  $L$  is the thickness of the membrane (m), and  $P_m$  is the mean pressure across the membrane (Pa). It is important to note here that viscous permeation is dependent on the mean radius squared and the mean pressure. This is not the case for other phenomena, such Knudsen flow.

### 3.2. Molecular Flow

Molecular flow, or Fickian diffusion, occurs when the number of intermolecular collisions per unit time outweighs the number of molecular collisions with the pore wall. The dimension of the pore and the type and number of molecules require the consideration of intermolecular collisions. When the interactions with the pore wall are at minimal, this type of diffusion creates little or no separation. The driving force for transport is usually coupled with Knudsen diffusion. Under steady state conditions, flux occurring in the molecular flow regime is

generally described using Fick's Law (Equation 3.2), where  $J_m$  is the molecular flux ( $\text{mol}\cdot\text{m}^{-2}\cdot\text{s}^{-1}$ ),  $C$  is the concentration of the diffusing species ( $\text{mol}\cdot\text{m}^{-3}$ ),  $z$  is the distance the diffusing species travels between collisions (m), and  $D_m$  is the molecular diffusivity ( $\text{m}^2\cdot\text{s}^{-1}$ ).

$$\text{Equation 3.2} \quad J_m = -\frac{\varepsilon}{\tau} D_m \frac{dC}{dz}$$

### 3.3. Knudsen Flow

When the diameter of a pore begins to approach the mean free path of the molecules diffusing through the porous network, collisions with the pore wall are just as likely as collisions with one another. The increase of interactions between the porous network and diffusing species change the diffusion dynamics. These changes were first described by Martin Hans Christian Knudsen<sup>25</sup>. Steady state permeation within the Knudsen regime is described in Equation 3.3,

$$\text{Equation 3.3} \quad F_k = -\frac{J_k}{\Delta P} = \frac{2r\varepsilon}{3\tau\theta_k L} \left[ \frac{8}{\pi RTM} \right]^{0.5}$$

where  $F_k$  is the Knudsen permeation ( $\text{mol}\cdot\text{m}^2\cdot\text{s}^{-1}\cdot\text{Pa}^{-1}$ ),  $J_k$  is the Knudsen flux,  $\Delta P$  is the pressure difference across the membrane (Pa),  $M$  is the molecular weight of the gas (kg/mol), and  $\theta_k$  is used as a correction factor. The original derivation assumes smooth pore walls and diffusing molecules' reflections are specular. Generally, this is not the case with most porous solids, as reflections tend to be more random, and  $\theta_k$  is used to account for this behavior. With perfectly smooth walls  $\theta$  is equal to one and increases with roughness. The key observation is that Knudsen permeation is linearly dependent on the average pore radius, the molecular mass of the diffusing species and, most importantly, is independent of pressure. It is also important to note that although both Knudsen and molecular flow have differing dependencies and express themselves as such, they can occur simultaneously in a system (known as the transition region) where the pore dimensions are on the same magnitude as the molecular mean free path of the

diffusing species. For the transition region, the effective diffusivity ( $D_{\text{eff}}$ ) may be expressed using a circuit analogy, as the sum of two resistors in series:

$$\text{Equation 3.4} \quad \frac{1}{D_{\text{eff}}} = \frac{1}{D_{\text{m}}} + \frac{1}{D_{\text{k}}}$$

Described above are the transport processes explaining how molecular species and fluids diffuse through porous media. For all of the previously discussed models, it was assumed that the molecules have only limited interaction with the pore wall. However, once the radius of the pore decreases below a certain level, dependent upon the membrane material and the diffusing species<sup>26</sup>; or operating temperature of the system approaches the condensation temperature, diffusing gas laws may become invalid, and one needs to consider other means in which to describe the transport phenomena observed.

### 3.4. Surface Diffusion

When temperatures and vapor pressures of diffusing species approach the limits where the adsorption of molecules onto the porous structure occur, the diffusing species can be more accurately treated as a moving liquid. At low surface concentrations, the surface flux can be expressed by the rearrangement of Fick's first law and the consideration of the saturation capacity,  $C_{\text{sat}}$  (mol/m<sup>2</sup>) resulting in:

$$\text{Equation 3.5} \quad J_{\text{s}} = -\frac{2\varepsilon^2}{\tau} \frac{D_{\text{s}}}{r} C_{\text{sat}} \frac{d\theta}{dL}$$

Where  $D_{\text{s}}$  is the surface diffusion constant (m<sup>2</sup>/s),  $\theta$  is the loading of the surface (the surface concentration divided by the saturation capacity). It can be noted that as the pore radius decreases, the surface flux will increase. This phenomenon, although counter intuitive at first,

can be described in the following manner: As the pore dimension decreases, the opposite walls get closer, as do the adsorption sites on these walls. It is when these sites begin to approach one another that the energy barrier required for a molecule to leave one adsorbed site for another site is reduced. This reduction in the energy barrier allows for the facilitation of a molecule to “hop” up and down the porous network.

Finally, if the change of base is applied to Equation 3.5 to rewrite the expression as a dependence on pressure instead of concentration one arrives at Henry’s Law<sup>27</sup> of adsorption,

$$\text{Equation 3.6} \quad q = K_H P$$

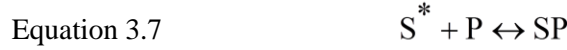
which applies to low adsorption loadings, where  $q$  is the moles of gas adsorbed per kilogram of adsorbent (mol/kg),  $K_H$  is the Henry’s constant (mol/Pa kg), and  $P$  is the pressure of the gas (Pa).

### 3.5. Adsorption Dynamics

There are two types of adsorption that can occur between an atom or molecule (adsorbates) and a surface (adsorbent); physical and chemical. Physical adsorption (physisorption) occurs when a gas below a critical temperature begins to adsorb onto the surface through Van der Waals interactions. For monolayer adsorption, this behavior is dependent upon the attractive forces between the adsorbate and the adsorbent; the number of available adsorption sites on the adsorbent surface, the temperature, and pressure. Chemical adsorption (or chemisorption) is observed when the adsorption energies approach the energies of formation of chemical bonds. In multilayer adsorption, physisorption, the ability of adsorbate molecules to accumulate onto an adsorbed monolayer, depends strongly on adsorbate-adsorbate attractive forces as well as the usual adsorption dependencies.

Adsorption isotherms and kinetic derivation of these isotherms was first developed by Langmuir<sup>28, 29</sup>. Adsorption-desorption dynamics can be described by the 1<sup>st</sup> order equilibrium chemical reaction between the reactants; the number of adsorbate particles ( $P$ ), the available

adsorption sites ( $S^*$ ); and the products; described here by the occupied sites (SP). This relationship is illustrated in Equation 3.7



The 1<sup>st</sup> order equilibrium constant is:

$$\text{Equation 3.8} \quad K_{eq} = \frac{[SP]}{[S^*][P]}$$

In addition [SP] is directly proportional to the ratio of filled sites ( $S^*$ ) to the total number of sites (S); expressed as a fractional coverage,  $\theta^* = S^*/S$ .  $[S^*]$  is proportional to the available sites,  $(1 - \theta^*)$ . For gases, the number of particles can be expressed as a pressure, P as described by the ideal gas law. Rearranging Equation 3.8 for the fractional coverage one arrives at Equation 3.9, as known as the Langmuir isotherm, where  $\alpha$  is the Langmuir constant.

$$\text{Equation 3.9} \quad \theta^* = \frac{\alpha p}{1 - \alpha p}$$

Where the Langmuir constant has a temperature dependence described by the Van't Hoff equation, Equation 3.10, where  $\alpha_1$  is the Langmuir constant at a temperature,  $T_1$ ,  $\alpha_2$  the constant at temperature,  $T_2$ , (given in degrees Kelvin),  $\Delta H$  is the enthalpy of adsorption, and R is the gas constant.

$$\text{Equation 3.10} \quad \ln\left(\frac{\alpha_2}{\alpha_1}\right) = -\frac{\Delta H}{R}\left(\frac{1}{T_1} - \frac{1}{T_2}\right)$$

It is also important to note that  $\theta$  can be expressed as the ratio between the concentrations of the surface adsorbed species ( $C^*$ ) and the maximum loading; saturation capacity ( $C_{sat}$ ). At very low



loadings, Equation 3.9 behaves linearly. As  $\alpha p$  approaches zero,  $1 - \alpha p$  approaches 1, and the Langmuir isotherm can be simplified to Henry's Law shown in Equation 3.6. The Langmuir adsorption isotherm accurately describes the behavior of commonly observed monolayer-favorable adsorption dynamics.

In 1938, by applying the following assumptions along with the original assumptions Langmuir used, Stephen Brunauer, Paul Hugh Emmett, and Edward Teller were able to successfully extend the Langmuir isotherm to include multilayer adsorption<sup>30</sup>, commonly known as BET theory (Equation 3.11).

- 1) The heat of adsorption of the 1<sup>st</sup> layer is different from the subsequent layers.
- 2) The heats of adsorption of the subsequent layers are the same and equal to the heat of condensation of the liquid.
- 3) Adsorption and desorption can only occur on the outer most layer.
- 4) There are no interactions between layers

Equation 3.11 
$$\theta^* = \frac{cx}{(1-x)[1+(c-1)x]}$$

Where  $x$  is the ratio between the pressure of the adsorbate in the gas phase and the saturation pressure at the experimental conditions, and  $c$  is the BET constant with a temperature dependence described by the Arrhenius equation. The Arrhenius equation is shown in Equation 3.12;

Equation 3.12 
$$c = e^{\frac{\Delta H}{RT}}$$

where  $\Delta H$  in this case is the difference between the heat of adsorption of the 1<sup>st</sup> monolayer and the heat of condensation of the liquid adsorbate at that temperature,  $T$  and  $R$  have the usual meaning. Within a porous system, if an adsorbate is below its critical temperature and the vapor phase is high enough for multilayer adsorption, subsequent layers will adsorb until the pore is filled. This is known as capillary condensation.

### 3.6. Capillary Condensation

Capillary condensation occurs within a pore when an adsorbate's vapor pressure is higher than a reduced vapor pressure. This reduction of the vapor pressure ( $P_r$ ) is dependent on the pore radii ( $r$ ), the liquid surface tension ( $\sigma_s$ ), the contact angle ( $\Psi$ ), and the molar volume of the liquid ( $V_m$ ), and described by the Kelvin Equation<sup>31</sup>.

$$\text{Equation 3.13} \quad \frac{RT}{V_m} \ln \frac{P_r}{P_{\text{sat}}} = -2 \frac{\sigma_s \cos \psi}{r}$$

Where  $P_{\text{sat}}$  is the saturation pressure and  $R$ , and  $T$  have the usual meanings. The application of the Kelvin equation with BET theory and diffusion models has allowed for the development of many characterization methodologies for porous materials.

### 3.7. Hindered Diffusion

In cases where the solute concentration is much larger than that of the solvent, and the shape of the solute is assumed to be a hard sphere, the resistance to Brownian motion may be equated to the Stokes-Einstein equation as shown in Equation 3.14;

$$\text{Equation 3.14} \quad D_{\infty} = \frac{kT}{6\pi\eta r_s}$$

where  $D_{\infty}$  is the diffusivity in the dilute bulk solution,  $k$  is the Boltzmann constant,  $T$  is the temperature,  $\eta$  is the solvent's viscosity, and  $r_s$  is the solute's hydrodynamic radius. However, when the solute particle is not spherical, the Stoke-Einstein equation only roughly approximates

the diffusional constant. Better estimates can be achieved with other correlations such as the Wilke-Chang expression shown in Equation 3.15,

$$\text{Equation 3.15} \quad D = 7.4 \times 10^{-8} \frac{T(\psi_w M_w)^{1/2}}{\eta_w V_B^{0.6}}$$

where  $D$  has the usual meaning of diffusivity constant,  $M_w$  is the molecular weight of water (g/mol),  $T$  is the temperature (K),  $\eta_w$  is the viscosity of water (cP),  $V_B$  is the molar volume of the solute at its normal boiling point (cm<sup>3</sup>/mol), and  $\psi_w$  is the association factor for water, which is 2.6 (unitless)<sup>32-34</sup>.

For solute particles whose size approaches the pore radii, hindered diffusion occurs when the chemical-physical interactions between the solute and pore wall cause the molecular friction coefficient to exceed the value of that for a free solution. This hindered diffusion is dependent on size of the molecule, pore size, electrostatic interactions, and shape of the molecule and pore. This phenomenon is largely observed in biological systems such as renal and extrarenal microcirculation<sup>35-44</sup>, with applications to separations for enzyme chromatography and size exclusion<sup>45-49</sup>.

Under steady state conditions and low solvent flow rates (i.e.  $Pe \ll 1$ ); the Peclet number is based on the pore length and the effective diffusivity ( $D_{eff}$ ) for a solute diffusing through a membrane with cylindrical pores orthogonal to the membrane surface. Four components must be considered in the calculation of this number: the porosity ( $\epsilon$ ), the partition coefficient ( $\Phi$ ) which for a pore with a radius of  $r_p$ ,  $\Phi = (1-r_s/r_p)^2$ , the bulk diffusivity from the Stokes-Einstein equation or the Wilke-Chang correlation, and the hydrodynamic hindrance factor ( $H$ ).

$$\text{Equation 3.16} \quad D_{eff} = \epsilon \Phi D_{\infty} H$$

The only component that is unknown for a system under these conditions is the hydrodynamic hindrance factor. Due to the vast sensitivities of diffusional responses to the many other parameters on which this phenomenon depends upon, it is difficult to completely understand and account for the individual components such that an explicit derived expression can be found. A number of numerical approximations have been developed that have fairly accurate predictions<sup>50</sup> compared to the observed phenomenon<sup>50</sup>. A review covering the most widely accepted expressions for the hydrodynamic hindrance factors, along with treatments of hindrance effect of convective diffusion ( $Pe \rightarrow 1$ ), and effect of some electrostatic interactions has been presented by W. M. Deen<sup>51</sup>.

### **3.8. Summary**

All of the theories presented in this chapter build foundations of the characterization techniques used to evaluate a membrane's quality and that are used to predict that membrane's separative power. It is important to note that each of the diffusion and adsorption dynamics apply most accurately to mass transport of the gas phase. These laws should apply to solute transport in a liquid filled pore but liquid diffusion specifically is not as fully understood as those of the gas phase<sup>52</sup>.

## **4. CHARACTERIZATION**

In the successful development of novel membranes, consideration needs to be made of the effect of synthesis parameters to the microstructure and overall morphology as well as the resulting membrane performance. For example, how do the drying conditions affect the microstructure and defect quantity for a sol-gel dip coated membrane? Without careful experimental planning and intensive characterization, it is almost impossible to produce a consistent dip coated sol-gel that is defect free. In order to improve the success of membrane synthesis it is necessary to develop membrane characterization methods that allow one to understand the intrinsic link between the synthesis conditions, the physical heterogeneity of the microstructure, morphology, and its transportive behavior.

### **4.1. Static Methods**

Static methods are characterization techniques that measure the physical heterogeneity of the microstructure and do not monitor transport properties. Generally, there are two types of static characterization methods, direct and indirect. Direct techniques are used to probe the physical or chemical structure via the direct interaction of the measurement with the membrane itself; such as scanning electron microscopy (SEM) and transmission electron microscopy (TEM). Indirect methods require the aid of a liquid. In these cases, the measurement monitors how the pressure required for the liquid volume to intrude into the membrane's porous structure, as in mercury porosimetry.

#### **4.1.1. SEM and TEM**

Electron microscopy has provided bountiful information of surface morphology. With image analysis of the micrographs taken, porosity can be calculated. Defect sizes and quantities can be estimated, along with an estimation of the nominal pore sizes down to the resolution limit of the system. By imaging a cross-sectional slice of the membrane, the morphology of the entire

membrane system can be approximated as well. In order to make that determination for the entire membrane, multiple cross-sectional scans need to be performed. Scanning of the entire membrane is time intensive, and often only, a few cross-sections are taken and assumed representative of the entire membrane. While useful, these techniques are not without their own limitations. SEM and TEM systems are very expensive to purchase and maintain. Scanning microscopy techniques are also destructive to the membrane, having scanned a membrane, it is unusable. Some instruments such as TEM; are only capable of imaging through very thin slices of material, limiting the information one can gather about the whole membranes system in question. These methodologies are also very laborious to characterize the whole surface and virtually impossible to image enough slices to know the entire physical structure of the probe system. Furthermore, they do not provide any chemical information that would aid in predicting adsorptive properties. In other words, a picture maybe worth a thousand words, but is it worth a thousand dollars?

#### **4.1.2. Radiation Scattering**

Unlike electron microscopy, probing porous solids with radiative energy is a nondestructive investigation technique. This method allows for the determination of porosity and surface area by bombarding the material of interest with an incident beam of photons and measuring the angular distribution of the scattered light. The dependence of the angular distribution ( $\bar{\theta}$ ) is indirectly proportional to the pore diameter (d) and directly proportional to the wavelength ( $\lambda$ ) of radiation (Equation 4.1).

$$\text{Equation 4.1} \quad 2\bar{\theta} \approx \lambda/d$$

This technique is able to achieve a spatial resolution of 5-50nm with the implementation of X-rays, although higher resolutions can be achieved with electron microscopy techniques.

Radiative methods are more amenable to a large variety of materials. Coupled with the fact that radiation scattering techniques are non-destructive to the probed material these approaches for characterization are extremely attractive. Unfortunately, radiation scattering measurements are not without their limitations. Due to the nature of the measurement, the entire sample is bombarded and results from this technique depend upon long range ordering of the porous network, and produces results representative of an ensemble average with no spatial information about the material. In addition, like electron microscopy, instruments for radiative scattering can also be very costly to setup and maintain.

#### **4.1.3. Infrared**

Infrared spectroscopy (IR) has proven itself a valuable tool in identifying materials, chemical reactions, and surface chemistry. With direct applications in numerous fields; such as pharmaceuticals<sup>53</sup>, pesticide detection<sup>54, 55</sup>, semiconductor technology<sup>56, 57</sup>, and process control. Specifically Fourier Transform Infrared Spectroscopy (FT-IR) has been used as a characterization method to elucidate chemical composition of inorganic<sup>58-62</sup>, organic<sup>63, 64</sup>, and hybrid organic-inorganic<sup>65-67</sup> membrane compositions. FT-IR has been used as a tool to measure the rates of diffusion<sup>60, 68-70</sup> and to ascertain detailed information about adsorption dynamics and molecular conformations, such as the determination of carboxylic acid functional groups as a means to explain increased adsorptive capacities and stabilization of other organic compounds<sup>71-75</sup>. Most recently methods to estimate surface areas have been presented by McCool, Murphy, and Tripp in 2005<sup>76</sup>. These methods present a relatively simple and quick method to estimate the surface areas of porous silica compounds by calculating the ratio of the free hydroxyl silica peak area found at 3747 cm<sup>-1</sup> to the bulk silica overtone mode found at 1870 cm<sup>-1</sup>. Comparing the ratio of these areas with those from measured calibrants with known surface areas, they created a technique with remarkable agreement with standard BET characterization techniques.

#### 4.1.4. Porosimetry

Pore size distributions for microporous structures can be ascertained by measuring the volume of a noncompressible non-wetting fluid, generally mercury, which enters into the porous network under increasing pressures. The pressure required to force a non-wetting liquid into a pore is shown in Equation 4.2, where  $r_p$  is the pore radii,  $\gamma$  is the surface tension at the liquid air interface (generally assumed to be 0.48 N/m for mercury),  $\theta$  is the contact angle (generally assumed to be  $140^\circ$  for mercury), and  $P$  is the pressure applied. One major hurdle to overcome when implementing this approach is the vast pressure that is required to measure pore sizes in the nanometer scale demonstrated in Figure 4.1. This extreme pressure is difficult to achieve and the micro and mesoporous structures may be destroyed before liquid can enter the pore interior. However, it is noted that this method is very accurate and useful for measuring the pore size distribution in macroporous supports.

Equation 4.2 
$$r_p = -\frac{2\gamma \cos \theta}{P}$$

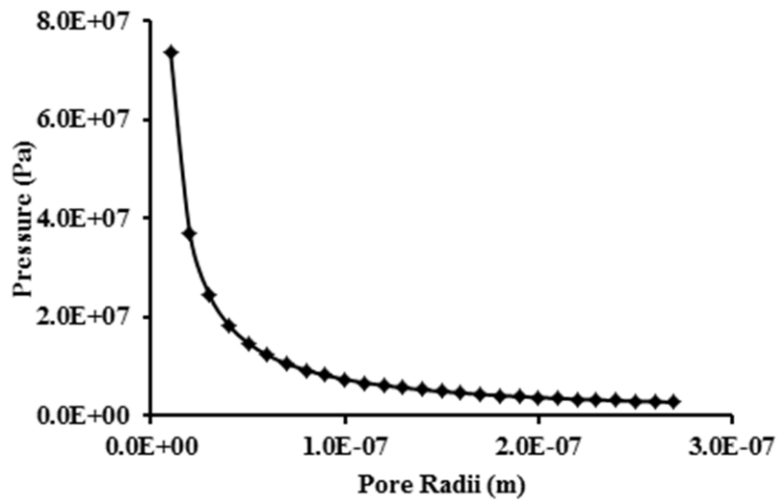


Figure 4.1 The dependence of pressure on pore size required for mercury porosimetry. (2.8 MPa for a pore with a radius of 260 nm)



Physisorption is one of the most widely used techniques for the determination of pore size distributions, surface area, and pore volumes of nanostructured porous membranes and materials. Generally, the substrate needs to be degassed to remove adsorbed vapors on the material surface, usually water vapor adsorbed from exposure to the atmosphere, before accurate measurements using physisorption can be achieved. Commonly this is done by placing the substrate into an evacuated vessel at elevated temperatures for a predetermined amount of time to remove any adsorbed vapors. It is important to note that the temperature for drying needs to be carefully chosen based on the analyte physical properties, i.e. for carbon-based structures like activated charcoal or nanotubes, it should not exceed the materials pyrolysis temperature. In the case of polymer and hybrid membranes, evacuation temperature should remain below the glass transition temperature of the organic matrix.

Once the substrate is dried, it is cooled to a temperature below the condensation temperature of an inert gas used for analysis (usually N<sub>2</sub> at 77K). The substrate is exposed to small doses, much less than the saturation pressure, of analysis gas. The previously degassed substrate is allowed to reach its equilibrium adsorption capacity for the adsorbate introduced. The amount adsorbed is carefully measured either gravimetrically or volumetrically. Once equilibrium is reached, subsequent doses of adsorbate are introduced to generate a multilayer adsorption isotherm. In some cases, it may be beneficial to run the process to create a desorption isotherm. For mesoporous materials knowing the pressures used relative to the adsorbate's saturation pressure and the amounts adsorbed at each step allows for the application of the Kelvin equation shown here; and BET theory discussed in sections 3.5 and 3.6 respectively.

Equation 4.4

$$\ln \frac{P_r}{P_{\text{sat}}} = -2 \frac{\sigma_s}{r_k} \frac{V_m}{RT}$$

Where  $r_k$  is the Kelvin pore radii and  $P_r$ ,  $P_{\text{sat}}$ ,  $V_m$ ,  $R$ ,  $T$  and  $\sigma_s$  are defined in section 3.5 and 3.6 . The Kelvin pore radii can be calculated by Equation 4.3.

Equation 4.3

$$r_K = r_p + t$$

Where  $r_p$  is the pore radii and  $t$  is the monolayer thickness of the adsorbate. Values for  $t$  can be found by testing the amount of gas required for monolayer coverage onto a chemically similar flat surface. Assuming the bulk uptake of the adsorbate is dominated by the pore structure of the adsorbent, the pore size distribution for the material of interest can be calculated by differentiating the amount of gas required to reach equilibrium for each change in pore size. This method is capable of generating vast amounts of valuable information with one technique that only be achieved with combinations of other tests. However, this approach is not without its limitations. It can be difficult and time consuming to ensure the material of interest is completely degassed. Often several assumptions about the materials' interactions with the analysis gas need to be made, such as the molecular interaction on the surface. This measurement is also challenged by materials like track etch membranes. The sensitivity of the measurement is highly accurate with samples of high surface areas and less reliable with low surface area materials. One way to circumnavigate this challenge is to use a larger amount of analyte, but this too can be unrealistic. Finally, for materials intended for membrane application physisorption analysis measures surface area contributions of the entire porous network include dead end pores. For particles and zeolites used in packed beds, this poses very little concern. However in regard to membrane systems, dead end pores are not active and do not contribute to the flow properties of the membrane system. In some cases, this circumstance may lead to significant errors in predicting flow characteristics of the analyte.

## 4.2. Dynamic Methods

Dynamic methods discussed here have been defined as techniques used to characterize porous microstructures and defect quantification based on observed flow characteristics of a fluid (for simplicity usually inert gases) under varying conditions i.e. temperature and pressure.

### 4.2.1. Bubble Point

Bubble point measurements are simple and effective methods for determination of the largest pore size or defects within a membrane system. The top side of a membrane is covered with a wetting liquid, often water, or isopropanol and the bottom is in contact with gas. Applying increasing gas pressure to the underside of the membrane forces gas bubbles into the membrane's pore and through to the other side. The pressure required for the gas to penetrate the membrane's pores is governed by a variation of the Laplace equation, shown in Equation 4.5,

$$\text{Equation 4.5} \quad r_p = \frac{2\gamma \cos \theta}{\Delta P}$$

where  $r_p$ ,  $\gamma$ , and  $\theta$  are described in section 4.1.4, in this application  $\Delta P$  is the change in pressure across the membrane. By monitoring the gas flow through the wetting membrane as function of pressure, from the first pressure that flow begins through the smallest pore measurable and comparing to the gas flow pressure response of a dry membrane, a pore size distribution can be generated.

### 4.2.2. Gas Permeability

Gas permeability measurements and analyses are useful in determining the types of flow regimes, discussed in chapter 3, and potential performance of a membrane. By measuring the flow rate of an inert gas as a function of pressure, calculation can be made describing the relationship between the dependence of permeance upon pressure. If the permeation is found to be independent of pressure, one can deduce that the bulk flow is within the Knudsen regime. If

there is a pressure dependence and the intercept approaches zero, molecular flow dominates. When a pressure dependence of the permeation has a positive intercept, the pore size of the membrane is on the same order of magnitude as the mean free path, known as the transition region. The total permeance,  $F_t$ , is equal to the inverse sum of both the molecular permeance,  $F_v$ , and Knudsen permeance,  $F_k$ , shown in Equation 4.6.

$$\text{Equation 4.6} \quad \frac{1}{F_t} = \frac{1}{F_v} + \frac{1}{F_k}$$

If a membrane is previously characterized by this method before modification via ALD, CVD, sol-gel coating, or any number of modification techniques; the transport dynamics of the modified top layer can be established by subtracting the transportive properties of the pre-modified membrane from the final system's pressure response. Other approaches include changing the permeation gas allowing one to study the effects of  $\sqrt{MW}$ , and determine separation factors for mixtures of gases. Ideally for the Knudsen regime the ideal separation factor,  $\alpha^*$ , is shown in Equation 4.7,

$$\text{Equation 4.7} \quad \alpha^* = \sqrt{\frac{MW_2}{MW_1}}$$

where MW is the molecular weight of each gas studied. Another method for measurements of the separation factors and selectivity of gas combinations can be performed using a Wicke-Kallenbach cell.

### 4.2.3. Wicke-Kallenbach

The Wicke-Kallenbach cell, shown in Figure 4.2, allows for the measurement of separation factors and permeance selectivity of gas combinations at counter current, isobaric conditions. By monitoring the flow rates of the feed and sweep gas and measuring the partial pressure of all of the components in the feed, permeate and retentate one is able to measure the effective diffusivities of each gas component. By varying the concentrations of the feed gases relative contributions of the Knudsen and molecular diffusivities can be determined<sup>52</sup>.

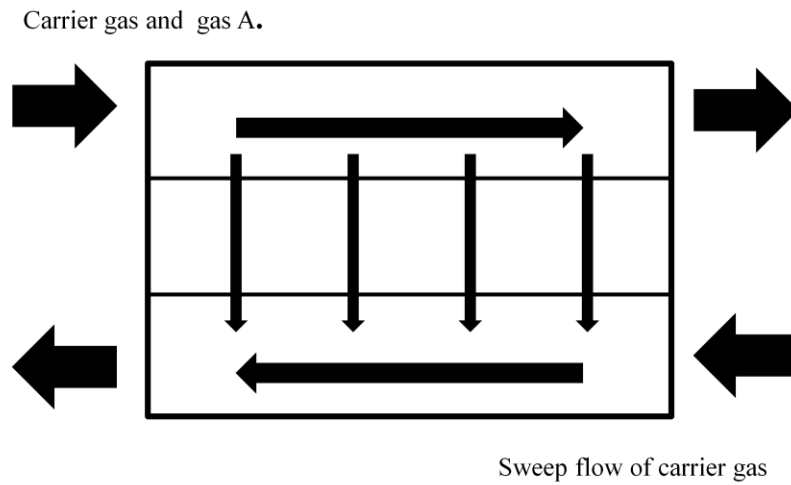


Figure 4.2 Diagram of a Wicke-Kallenbach cell

#### 4.2.4. Permporometry

Permporometry (shown in Figure 4.3,) is a technique developed to measure the pore size distribution of the active pores available for diffusive transport. Since capillary condensation begins at the point of restriction within a pore one has to assume that the pores have a consistent diameter through their entire length, i.e. cylindrical pores, shown in Figure 4.4.

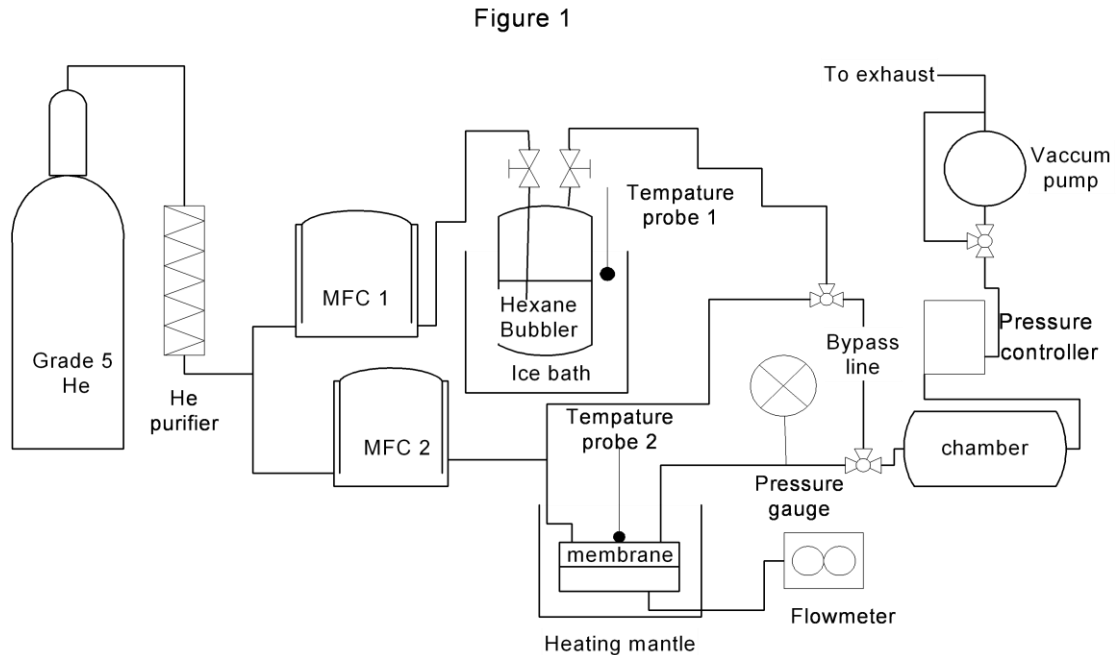


Figure 4.3 Typical permporometry system

The experiment is run by simultaneously measuring the permeance of an inert gas through a membrane system while varying concentrations of a condensable vapor. Carefully controlling the addition of mole fractions of a condensable liquid, such as alcohols or hydrocarbons, capillary condensation occurs within the smallest pores first via the Kelvin equation, Equation 3.13, the permeance response is measured. The vapor concentration is increased until either all of the pores of the membrane are blocked i.e. permeance is zero, or the vapor concentration is equal to the saturation pressure, Figure 4.5.

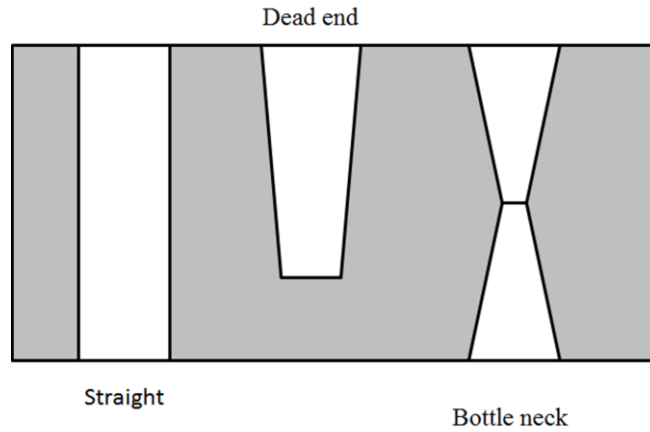


Figure 4.4 Shows the potential pore geometries. These are important to consider implementing permoporometry characterization; straight uniform pores, dead end pores, and bottlenecks.

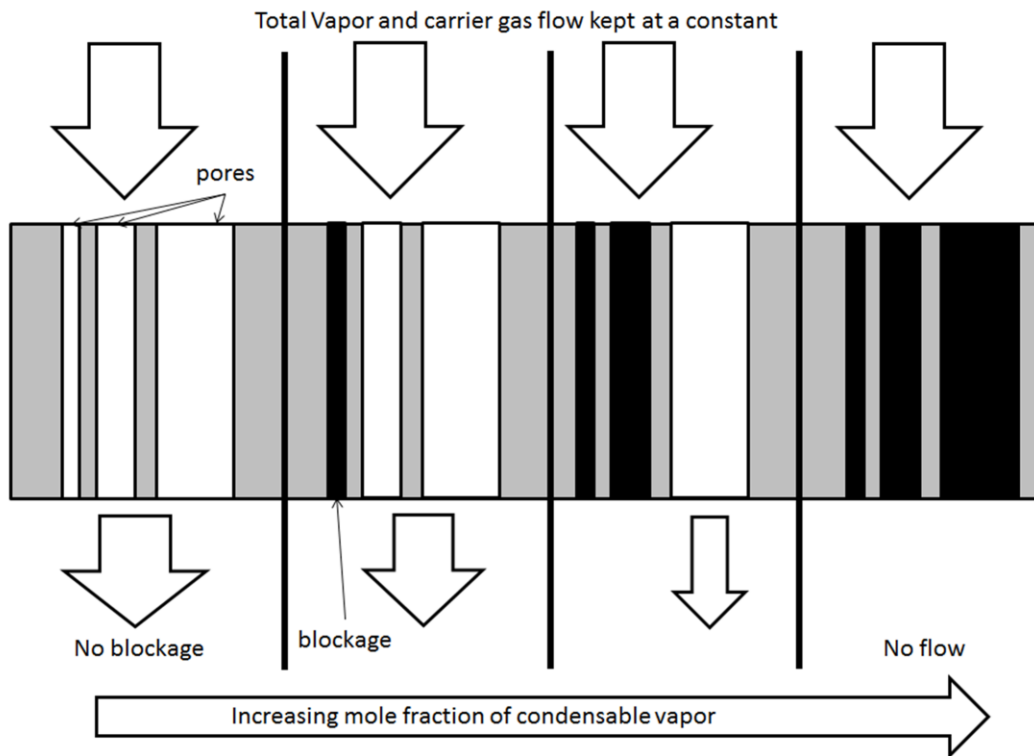


Figure 4.5 Demonstrates the pore size dependence of capillary condensation.

Assuming the flow is through the unblocked pores ( $\rho$ ) the permeance of the inert gas is shown<sup>77</sup> in Equation 4.8, where  $f(r)$  is the number of pores per unit volume with a pore radius from  $r$  to  $r + dr$ ,  $v$  is the Knudsen velocity  $F(\rho)$  is the total flux of the inert gas as a function of radii,  $l$  is the thickness of the membrane,  $R$  and  $T$  have the usual meanings. Differentiating both sides by  $r$  and rearranging the expression Equation 4.8 the pore size distribution can be calculated as a function of filled pores and permeance, Equation 4.9.

$$\text{Equation 4.8} \quad F(\rho) = \frac{2\pi v}{3RTl} \int_{\rho}^{\infty} r^3 f(r) dr$$

$$\text{Equation 4.9} \quad f(\rho) = -\frac{3l}{2\rho^3} \sqrt{\frac{MRT}{8\pi}} \frac{dF}{d\rho}$$

Generally the system is run at very low or no pressure across the membrane to avoid “stripping” of the condensed liquid from the pores. This also allows for the characterization of membranes with low mechanical stability. It is important to mention that this method based on capillary condensation is not capable of accurately measuring pore radii less than 2nm due to the monolayer thickness of most vapors that cause these pores to fill immediately.

### 4.3. Limitations

The current capabilities of characterization methods of nanoporous membranes and nanoporous materials tend to take a macroscopic approach or are ensemble-averaged measurements. In statistical mathematics, an “ensemble average” is defined as the mean that is a function of the microstate of a system according to the distribution of the microstates. The implication is that an ensemble-averaged measurement produces a value that is representative of a system and provides no detail of the real distribution. In most cases, membrane characterization is based on measuring the total response of a diffusing or condensing vapor/gas within the entire



microstructure environment. These methods are very effective at predicting the membranes' bulk performance. However, they do lack the capabilities to measure the specific heterogeneity that may exist on the molecular scale, i.e. pore roughness, adsorption site densities, and the variation of these properties across the membrane surface and through the pore. They are incapable of measuring single interactions at the interior of the pore, one molecule at a time (sub ensemble). An important challenge in membrane development is the lack of techniques to directly measure the intrinsic heterogeneity of the physical and chemical properties within membrane system<sup>1</sup>. The application and development of sub ensemble characterization methods will allow for the direct measurement of heterogeneity (i.e. the distribution of the microstates) within the porous network. These techniques have the capability to measure the distribution of the microstates that will enable the direct link to specific synthesis conditions to changes in the chemical and physical distributions of the microstates. It is this kind of detailed information that will allow the creation of successful inorganic membrane systems for industrial applications. Currently fluorescent techniques have been developed to measure materials and environments on a sub ensemble level capable to advance the understanding this interplay and further the use of inorganic membranes. Although only recently applied to inorganic membranes, success has been achieved<sup>4, 78-84</sup>.

## 5. FLUORESCENCE

Formally, luminescence is the emission of electromagnetic radiation (photons) from an atom or molecule that is occupying an excited electronic state, and is a form of cold body radiation as opposed to incandescence, or other forms of black body radiation, which emits electromagnetic radiation from a body due to elevated temperatures. Luminescence is broken down into many different subsets based upon their energy sources. Some of these types are: electroluminescence, a response to electrical currents; chemiluminescence caused by chemical reactions; and photoluminescence, the re-emission of photons from previously adsorbed electromagnetic radiation.

Quantum mechanically, the energy levels available to an electron within an atom or molecule have discrete values and are said to be quantized. The implication of the quantized energy levels is that only specific packets of energy can cause a shift of an electron from the ground state to an excited state. Figure 5.1 depicts the discrete energy levels available for electronic transitions. In order for a transition to occur, the energy of the photon adsorbed,  $E$ , must match the difference between the two levels. Equation 5.1 illustrates this point; where  $h$  is Planck's constant and  $\nu$  is the frequency of the photon.

$$\text{Equation 5.1} \quad E = h\nu$$

Some of these transitions are changes in rotational energy (arrow 1) and occur in the microwave region; and vibrational energy states (arrow 2) important in the Infrared region. A transition from the ground electronic state to the 1<sup>st</sup> or higher excited states, shown by arrow 3, is the type of transition due to the adsorption of photons within the visible spectrum to ultraviolet spectrum and result in photoluminescence. In this figure, only the first two levels are shown but many higher states may exist. Photoluminescence is separated into two categories based upon the type of excited state occupied by the atom or molecule; fluorescence, and phosphorescence<sup>85, 86</sup>.

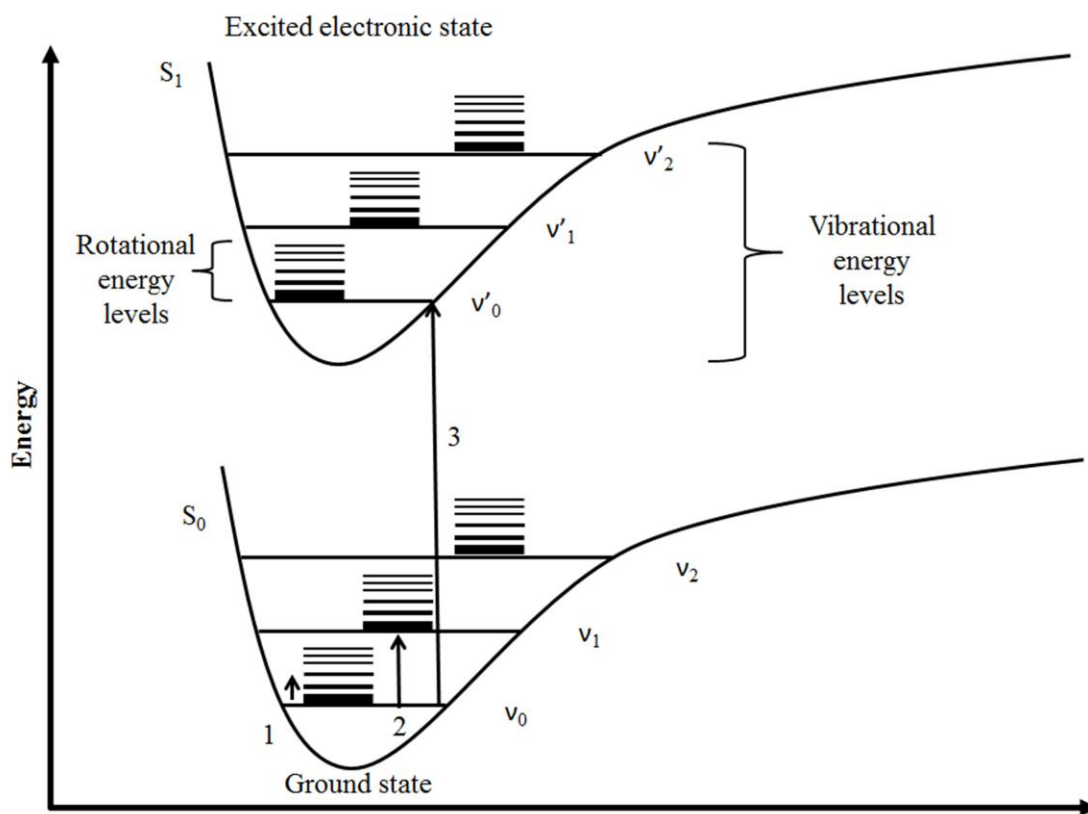


Figure 5.1 A Jablonski diagram. Showing the discrete energy levels allowed for transitions from the ground state,  $S_0$ , to the first excited state,  $S_1$ .

Fluorescence occurs when an electron inhabiting a singlet excited state, which is paired by opposite spin to an electron in the ground state that returns to the ground state. Because the spin state of the transition is allowed, the return to the ground state happens rapidly ( $\approx 10$  ns) and emits a photon with an energy that matches this transition. Phosphorescence is relatively slower (1ms to hours) and occurs when the electron enters an excited triplet excited state via a spin flip. In the excited triplet state, the spin of the excited electron is the same as that of an electron in the ground state. Therefore, the transition back to the ground state is not allowed and occurs slowly. These processes are shown in Figure 5.2; where the adsorption of a photon is shown, in step one. Once the electron is in an excited state, the electron releases some energy that it absorbed into the environment as non-radiative heat (step 2) and drops down to a lower level in the excited singlet

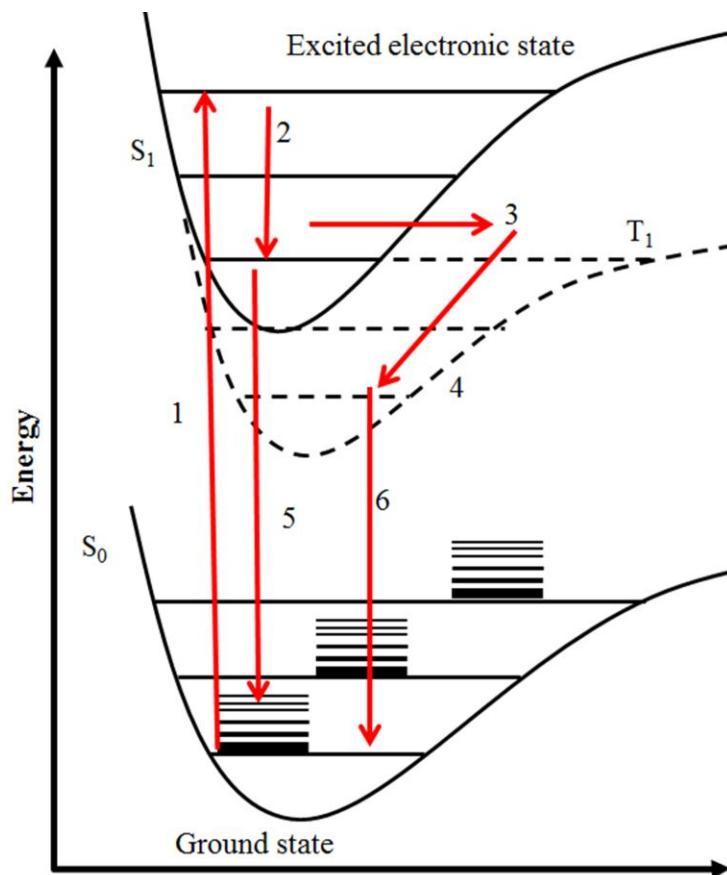


Figure 5.2 A Jablonski diagram for fluorescence and phosphorescence.

state ( $S_1$ ). In this diagram, there exists a triplet state ( $T_1$ ) with intersystem crossing. It is at this point that the electron can enter a fluorescent process and drop down the ground state ( $S_0$ ) and emit a photon (step 5); or move over to the triplet state (step 3). At this point, the electron continues to release non-radiative energy (step 4) and moves down the ladder. However, this is the triplet state ladder and the electron becomes trapped because the electron is in a state where a direct transition to the ground state is not allowed quantum mechanically due to spin multiplicity. However, this quantum mechanical rule can be relaxed by interactions between the magnetic dipoles generated by the spin of electron and the orbital motion. These interactions lead to coupling between the singlet and triplet states and provide a small probability for a transition back to the ground state (step 6). It is this small probability for the transition back to the ground state that is responsible for the increased phosphorescent lifetimes. It is important to note that this also causes a reduction in emission intensity and is not always seen in liquids at room temperature<sup>85</sup>. For these reasons, phosphorescence was not utilized as a spectroscopic method here and will not be discussed further.

### **5.1. Fluorescent molecules**

Although all molecules and atoms adsorb energy, not all molecules fluoresce. In order for a molecule to be fluorescent, it must have certain qualities. The energy gap between the ground state and the first singlet state must match the energy of photons within the visible spectrum. Secondly, the molecules must be able to transition back to the ground state from the first excited ground state. Thirdly, the molecule must have an electronic configuration that allows electrons to move freely between levels. Commonly, dyes that have these properties are organic molecules which contain an extended system of conjugated bonds giving them both planar and rigid structural mobility<sup>87</sup>, see Figure 5.3. The delocalized electrons in these conjugated systems stabilize the system and narrow the energy gap between the ground state and the first excited

singlet state, while the planar and rigid mobility reduces non-radiative decay by limiting rotational and vibrational motion. The larger the conjugated system is, the smaller the energy band gaps become and shift the emission to longer wavelengths.

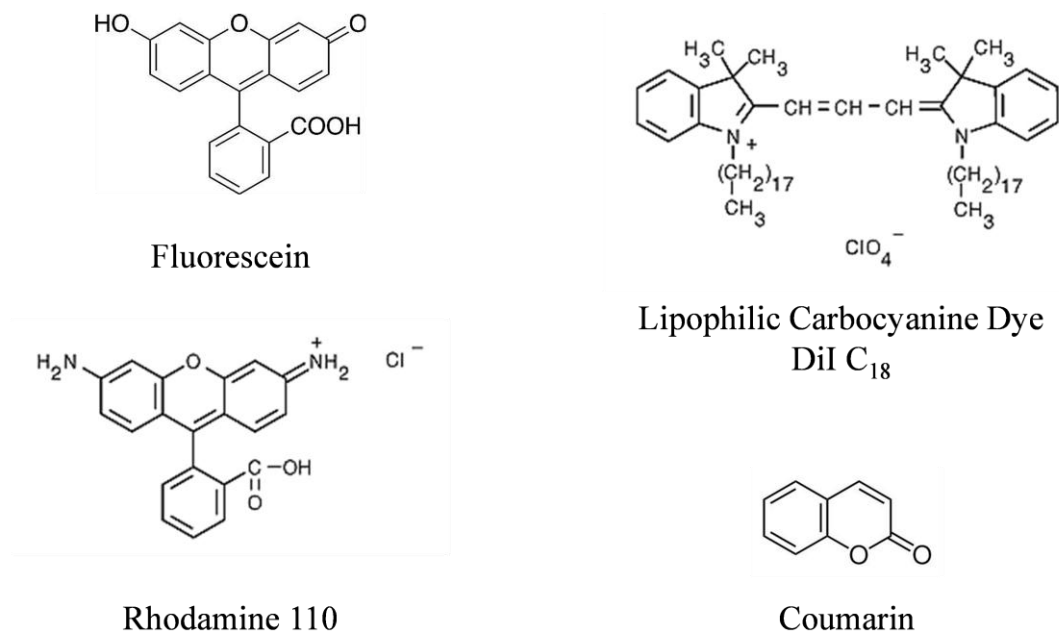


Figure 5.3 Examples of fluorescent molecules.

In order for a fluorescent molecule to be amenable to spectroscopy, it must also be chemically stable enough to survive the stress imposed on it by the excitation source, i.e. resistant to photobleaching<sup>88</sup>. Photobleaching can be subdivided into two types: reversible and irreversible. Reversible photobleaching occurs when a fluorescent molecule, in an excited state, becomes trapped into a triplet state. Since the lifetime of a triplet state is much longer than that of a singlet state, this molecule is no longer capable of emitting a fluorescent signal until it escapes the dark triplet state through a phosphorescent emission. Irreversible photobleaching is a process that photochemically destroys the fluorescent molecule's chemical structure. Once the chemical structure is changed, the electronic manifold that produces fluorescent emission no longer exists. Although photobleaching is usually problematic, some methods such as single molecule

spectroscopy can use this property advantageously to achieve low enough concentrations to resolve single molecule features<sup>85</sup>.

Two other important parameters that one must consider when choosing a fluorescent molecule are the extinction coefficient ( $\epsilon$ ) and the quantum yield ( $\phi$ ). The extinction coefficient is the direct measure of a dye's ability to absorb light at a given wavelength. For efficient fluorescence, high extinction coefficients are desired. However, most dyes with high extinction coefficients have small Stokes shifts. The extinction coefficient is measured at the maximum of the adsorption spectrum for the molecule and allows one to correlate the amount of material present based on the amount of light absorbed. Most dyes have extinction coefficients in the range of 5000 to 200,000  $\text{cm}^{-1}\text{M}^{-1}$  at  $\lambda_{\text{max}}$ , the wavelength at which the highest global peak is observed for that system.

The quantum yield is essentially the measure of fluorescent efficiency. It is the ratio of the number of photons emitted to the number of photons absorbed by the molecule. The range of values for quantum yield is generally between 0.1 and 1.0. Any values less than one is the results of energy loss through non-radiative decay.

## 5.2. Fluorescence properties

Fluorescence emission has several properties that are important to understand for the correct implementation of spectroscopic techniques. Although they are not steadfast rules, they are generally applicable to most cases. The first of which is known as Kasha's Rule. Kasha's rule states that; "the emission spectrum is independent of the excitation source<sup>89</sup>, as long as the excitation provides enough energy to promote an electron to the 1<sup>st</sup> excited state or higher." Once in an excited state, the electron quickly decays ( $10^{-12}$  s) down to the lowest vibrational energy in the first excited state. This rate is thought to be the result of many overlapping states with very closely related energies<sup>85</sup>. Since fluorescence emission generally occurs from the lowest state in the  $S_1$ , the emission spectrum is independent of the excitation spectrum. The implication of this

phenomenon concerning spectroscopy is that one can use any number of excitation sources to produce the same result, although with diminished efficiency. This consistent result means that it be used to reduce the cost of spectrometers and increase reproducibility.

Secondly, Fluorescence emission usually occurs at lower wavelengths or lower energy than the excitation source, known as the Stokes Shift<sup>85</sup>. This phenomena was first observed by Stokes in 1852 with his studies of Quinine<sup>90</sup>. The Stokes shift, shown in Figure 5.4, occurs when a molecule absorbs a source of electromagnetic radiation and electrons move to an excited electronic state. Some of the electronic levels available to them include states with higher vibrational energy levels than the lowest one in the first excited state,  $S_1$ . Since the lifetimes of excited vibrational energy states (picoseconds to nanoseconds) are shorter than the lifetime for transition between the electronic states, the electrons decay to the lowest vibrational level of  $S_1$ . This decay is emitted as non-radiative energy imparted to the environment, usually as heat.

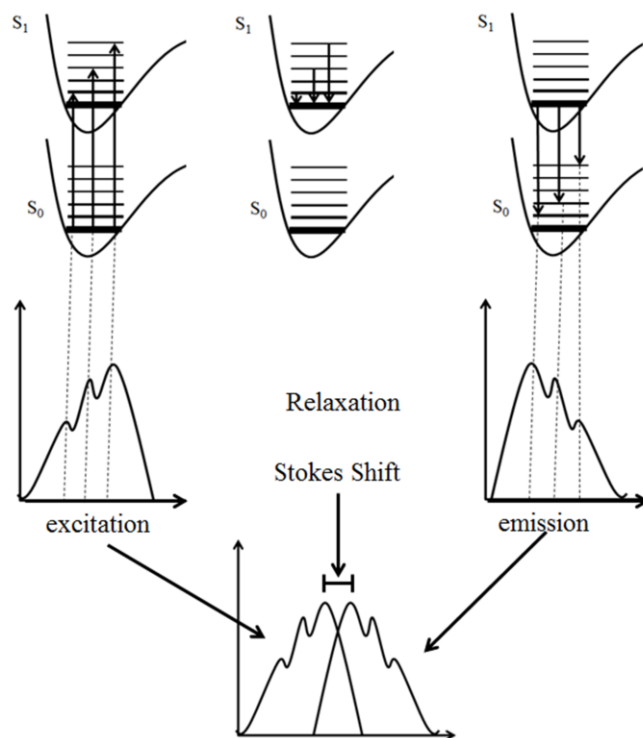


Figure 5.4 Depiction of how the Stoke shift is produced.



Often on returning to the ground state, these electrons drop down to higher vibrational levels of the ground state ( $S_0$ ). This results in a further loss of energy. It is important to note that the band gaps between the vibrational states in the ground state and 1<sup>st</sup> electronic state are very similar and generally follow similar selection rules for transitions, resulting in an emission spectrum similar to the mirror image of the adsorption spectrum.

Unlike vibrational and rotational spectroscopic methods, such as infrared spectroscopy, fluorescent spectroscopy has a distinct advantage due to the Stokes shift. Vibrational and rotational transitions from excited state to the ground state release energy to the environment in the form of heat. Because emission spectra are not generated by these transitions, the spectrum of the excitation beam through the material in question must be monitored for absorptive losses. Often the transmitted spectrum is compared to the spectrum of the unperturbed beam. Several distinct disadvantages arise from this approach. First, the amount of sample material present must absorb enough energy from the excitation source such that the change in the spectrum can be differentiated from the noise of the unperturbed source. It is important to note here that due to the nature of the experiment, increasing the excitation power cannot solve this problem. Conversely, too much sample material can absorb the excitation source entirely producing a loss of spectral information. Although these challenges can be overcome by changing the quantity of the sample, the former can be problematic for rare samples.

Due to the Stokes shift, these disadvantages are limited and usually easily overcome in fluorescent spectroscopy. Fluorescent spectroscopy measures the emission spectrum produced by the transition from an excited electronic state to the ground state. This transition releases energy in the form of photons, not heat; and as discussed above, the emission spectrum is shifted to lower energy and longer wavelengths than the excitation spectrum, Stokes shift ( $\Delta\nu_{st}$ ). The presence of the Stokes shift allows the one use an optical filter so that the system's detector only measures a specific region of the emission spectrum. Unlike vibrational and rotational methods, increasing the excitation power does not significantly contribute to the background signal and can

cause more electronic state transitions to occur and the increase of electronic state relaxations increase the emission intensity. Secondly, removing the signal from the excitation source and any fluorescence due impurities, can reduce the background signal to levels that allow for the measurement of the fluorescent spectrum produced by a single molecule.

### **5.3. Fluorescent Microscopy**

The implementation of fluorescent molecules has made significant improvement to microscopic and spectroscopic methods and has been utilized in both confocal imaging and wide field imaging. Generally, fluorescent molecules are used as a stain or tags for enhancing features or processes of interest that cannot be imaged directly. In biological systems different fluorescent dyes have been used so that they specifically bind to different areas of interest, such as cellular structures, so that inter and intra cellular interactions can be observed<sup>91</sup>. The efficiency of modern fluorescent dyes has allowed the analysis of many biological processes such as embryonic growth, mitosis, cytokinesis<sup>92-94</sup>, and the rapid field detection of bacteria and viruses with relatively inexpensive equipment<sup>95, 96</sup>. Most methods that implement fluorescent molecules are based on two imaging techniques; confocal imaging, or wide field imaging via Kohler illumination. Before either of these topics is discussed, it is important to address one of the most important parts of any microscope, the objective, and the effects it has on image resolution. It is also important to note, that when discussing these topics, it is assumed the illumination beam is the excitation source for the fluorescent molecules.

#### **5.3.1. Microscopic resolution**

The resolution of a microscope is defined as the shortest distance two points can be detected as separate entities by an observer or detector. The imaging system's resolution is often limited by aberrations or fundamentally by the diffraction limit. Aberrations are caused by optics of poor quality and can be improved upon by replacing the optical components with those of higher quality. In 1882 Ernst Abbe first observed diffraction limit, and the affects it has on

resolution<sup>97</sup>. Since it is caused by the nature of light, it cannot be removed. Assuming optics of perfect quality are used to create an image, as the light passes through the small aperture of the objective the light waves begin to light spreads out through the aperture. The individual waves begin to interfere with one another causing a diffraction pattern, known as Airy Disc. An Airy disc is commonly represented as a point spread function shown in Figure 5.5. A system is diffraction limited when two point spread functions overlap such that the maximum of one point spread function corresponds to the minimum of the second, this is known as the Rayleigh criterion<sup>98</sup>. The Rayleigh criterion states that an image is diffraction-limited when the first diffraction minimum of the image of one source point coincides with the maximum of another, and generally corresponds to the full width half maximum of one of the point spread functions. If the maxima of the two point spread functions are closer that this they are said to be unresolved. Mathematically, the Rayleigh criterion, the minimum resolution (R), for a microscope is calculated using Equation 5.2, where  $\lambda$  is the wavelength of light imaged, and N.A. is the numerical aperture of the objective used to create the image.

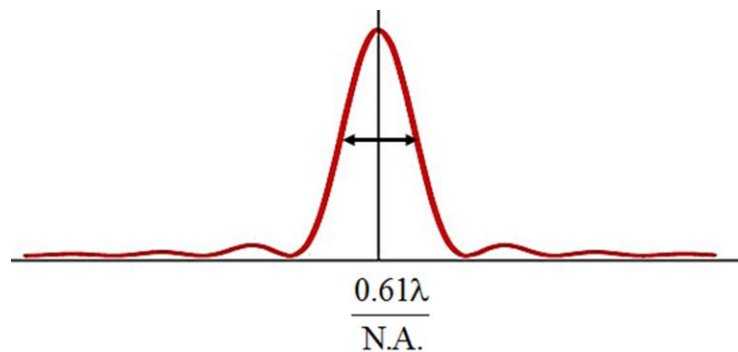


Figure 5.5 A point spread function representing a cross-sectional view of an Airy disc.

Equation 5.2 
$$R = \frac{0.61\lambda}{\text{N.A.}}$$

The objective of a microscope is found at the end of the optical train and is the optical element closest to the sample of interest. In its basic form, it is a high-powered magnifying glass with a very short focal length. Objectives have two parameters that are important to understand, magnification and numerical aperture. The numerical aperture, N.A., of an objective is described by, Equation 5.3, where  $n$  is the index of refraction of the medium between the objective and the sample, and  $\theta$  is the measure of the half angle subtended by the objective's lens and the focal point, shown in Figure 5.6. In Figure 5.6 the larger the half angle, the more light can be collected by the objective, which means that the N.A. not only is a measure of resolution but also the objectives' ability to collect light<sup>98</sup>. Most air objectives have typical N.A.s ranging from 0.1 to a maximum of 0.95; this is because the index of refraction of air is 1.0 and  $\theta$  is always less than unity. In order to achieve a N.A. beyond 1.0, index matching to the sample and lens must be accomplished by replacing the medium between the two surfaces. This is typically done with special oils. Utilizing oil objectives, N.A. values up to 1.6 can be achieved.

Equation 5.3                       $N.A. = n * \sin(\theta)$

The magnification determines the size of an image at the detector. It is calculated as the negative ratio of the distance of the image divided by the distance of the object, the negative accounts for the inversion of the image. When referring to an objective, the image distance is given by the tube length of the lens<sup>98</sup>.

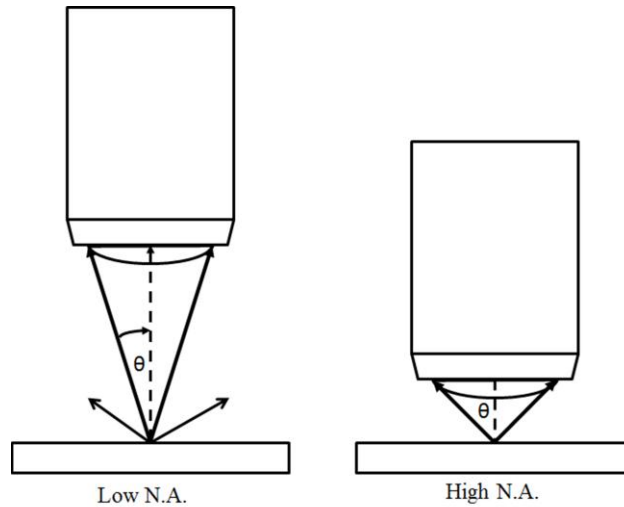


Figure 5.6 Diagram showing the half angle for two microscope objectives. Each with different half angles used to calculate the numerical aperture.

### 5.3.2. Kohler Illumination

Kohler illumination is used to generate a uniform illumination of the sample surface. In the case of fluorescence imaging, the illumination is an excitation source matched to the peak of absorbance in a fluorescent molecule. The fluorescent molecules can be used as stains to enhance the contrast of sample materials in question or to probe the sample's environment by monitoring fluorescent molecule's behavior. As mentioned above, band-pass filters are used to prevent the detectors from collecting photons from the excitation source, thus increasing the fluorescent imaging contrast.

The uniform illumination achieved by focusing the illumination source onto the backside of the objective is shown in Figure 5.7. Once the focused illumination source passes through the objective, a parallel beam is produced that has a uniform intensity. This beam is used to excite fluorescent

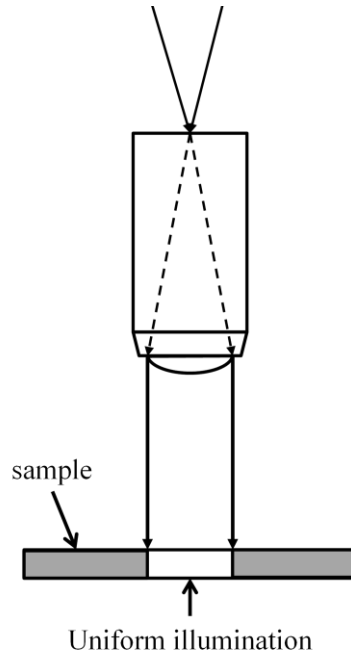


Figure 5.7 A ray diagram depicting Kohler illumination.

molecules within the entire illuminated sample area. The fluorescent emission and reflected and excitation is collected back through the objective and passed through a band-pass filter prior to imaging onto a detector. Fluorescent imaging systems utilizing Kohler illumination have several advantages. Since the whole sample area is uniformly excited, the entire area can be repeatedly imaged on to a CCD array, with the number of signal photons required and frame rates limited only by the camera (as high as 1000 fps). This is crucial for dynamic measurements, such as Fluorescence recovery after photobleaching (FRAP), which measure molecular diffusion of the fluorescent molecules. Secondly, these systems can easily achieve diffraction-limited images by matching optical components to the number of pixels in the CCD array. This advantage is important to systems that utilize Fluorescence Photoactivation Localization Microscopy (FPALM) by sequentially measuring the locations of fluorescent molecules to construct high-resolution images.

However, this uniform illumination can be problematic for some samples. If the sample area is optically transparent, the area out of the plane of interest can be excited and the emission

of the fluorescent molecule below the top surface will be added to the background; obscuring the information gathered at the top surface. This can be overcome by reducing the fluorescent molecule concentration. In samples that are sufficiently opaque, the background signal can be reduced or eliminated by diffusing or absorbing the background signal.

### **5.3.2.1. Fluorescence Recovery After Photobleaching**

Fluorescence recovery after photobleaching (FRAP) was developed to monitor molecule mobility within living cells. A sample is loaded with a chemically compatible fluorescent dye at a concentration sufficient to give a uniform fluorescent signal. At some time (t), the sample is bombarded with a high intensity source to irreversibly photobleach a small area within a larger image area. After the bleaching pulse, the signal of the previously bleached area is monitored to measure the fluorescent recovery. The recovery is the response from the unbleached fluorescent dyes diffusing into the bleached area. By knowing the extinction coefficient and quantum yield of the dye chosen for the study, the fluorescent signal can be associated to the molecular concentration of the diffusing species.<sup>5, 99-101</sup> Monitoring this response over time allows one to measure a diffusion rate, mobility, and any molecular binding rates that may be present for the molecules within the probed environment. Currently, this method is widely used due to the simplicity and the lack of need of specialized expensive equipment.<sup>6</sup>

One limitation that FRAP does encounter is how to consider the remains of the irreversibly photo-bleached fluorescent molecules. Most first order approximations assume once the molecule is bleached it does not exist at all and each molecule interacts only with its environment, not one another. If the bleached molecules or their individual components remain, they may inhibit the active fluorescent molecules by lowering the concentration gradient and slow the effective diffusion rate when compared to an empty system.

### 5.3.2.2. Fluorescence Photoactivation Localization Microscopy

Fluorescence Photoactivation Localization Microscopy (FPALM) is a relatively new technique emerging within the world of microscopy. FPALM is a method that generates an image made by localizing large numbers of molecules, imaged as small subsets at a time<sup>9, 10</sup>. This is achieved by carefully controlling the number of fluorescent molecules that are active during each image shown in Figure 5.8. In order to achieve this control, a special class of dye molecules that are photoactivatable are used. These dyes are not reporters of their environment unless effectively turned on by a pulse of activation source. Typically, this source has a different wavelength than the activated absorption and emission bands of the active fluorescent dye. The activation source is used to “turn on” a small number of fluorescent molecules. The number of molecules activated must be small enough such that they have a spatial density that allows their positions to be resolved from one another when imaged. Once activated, the molecules are imaged via Kohler illumination with an excitation source and sequential images are recorded until the activated population has become photobleached. This process can be repeated until the fluorescent molecule population is depleted or sufficient data has been acquired<sup>9, 10</sup>. Once all of the images have been recorded, each image is analyzed to determine the location of all molecules within the series of images. The localization precision ( $\sigma_x$ ) for point sources, imaged in two dimensions, by fluorescent microscopy can be calculated by Equation 5.4, where  $r_0$  is the standard deviation of the point spread function,  $N$  is the total number of photon collected,  $q$  is the size of an image pixel, and  $b$  is the background noise per pixel. Equation 5.4 suggests that if enough molecules can be localized, their positions and intensities can be used to generate an image with resolutions below the diffraction limit; with final image with resolutions as low as to 10 to 20nm<sup>10</sup>.



Equation 5.4

$$\sigma_x^2 = \frac{r_0^2 + q^2 / 12}{N} + \frac{8\pi r_0^4 b^2}{q^2 N^2}$$

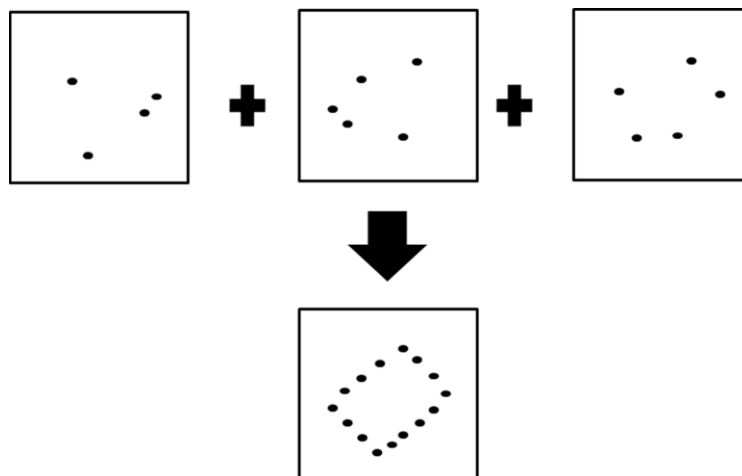


Figure 5.8 A diagram showing how a FPALM constructs a high resolution image.

One requirement that must be met in order to localize a molecule successfully is that the magnification of the imaging microscope must produce an image whose length per pixel is less than half of the full width half max of the point spread function. In effect, the point spread function of a single molecule must be imaged on to at least three pixels of a CCD array to accurately locate its center<sup>10</sup> and is related to the Nyquist limit.

The capability of this method to generate high-resolution images by circumventing the diffraction limit has quickly gathered considerable attention. However, FPALM is not without its limitations. The varieties of photoactivatable fluorescent probes are limited. In addition, like Single Molecule Imaging Spectroscopy, sample preparations and dye loading can be tricky and labor intensive. Although it is possible to measure molecular orientation and rotation rates, it is also important to mention that currently FPALM has not yet been used to measure molecular diffusion.

### 5.3.3. Confocal Imaging

Confocal microscopes differ from conventional microscopes in that it images the sample area one point at a time. A collimated excitation beam is passed through an objective and focused as a diffraction-limited spot on the sample area, demonstrated in Figure 5.9. Like Kohler illumination, the fluorescent emission is then collected back through the objective passed through a band-pass filter and imaged onto a detector. Since the excitation beam is focused to a diffraction limited volume the flux of the excitation source drops dramatically outside of the focal volume. Therefore, the background emission signal that may be present in Kohler illuminated systems is eliminated. This improves the signal to noise ratio and allows for single molecule spectroscopy. Unfortunately, imaging the small spot size is also the root cause for most of the disadvantages in confocal instruments. Since the emission from one spot is collected, the beam must be raster scanned and the image must be built one pixel at a time<sup>98</sup>. This process is slow, especially compared to Kohler illuminated imaging, and requires expensive scan stages that are incapable of achieving resolutions that match CCD arrays.

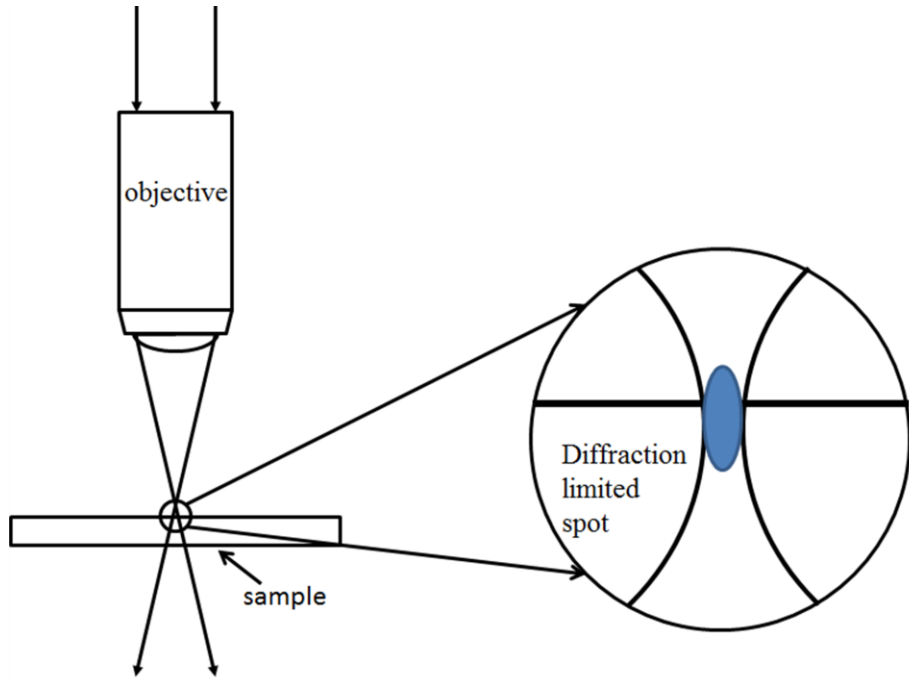


Figure 5.9 A cartoon showing the components of a confocal imaging microscope.

### 5.3.3.1. Single-Molecule Imaging Spectroscopy

Single Molecule Imaging Spectroscopy (SMIS) is a confocal imaging technique that raster scan a sample area. Once the raster scan is complete, single molecule features in the image are identified. Once a single molecule is located, the confocal microscope can return to initial location and monitor that molecule's behavior over time. Monitoring how the fluorescent molecule interacts with local environmental factors can provide a detailed picture of heterogeneity within the probed sample that cannot be achieved with many other spectroscopic and microscopic characterization techniques, such as ensemble averaging like FRAP and similar techniques<sup>85</sup>. By monitoring an individual molecule's behavior, SMIS allows for the direct measurement of local heterogeneity that is present in the sample of interest that is lost in ensemble averaged measurements<sup>7</sup>. SMIS also capable of measuring molecular rotation, orientation, and rotation rates by either exciting the sub population with a known polarized source or separating the emission signal into polarized sub sections. This allows thermodynamic and chemical interaction to be monitored.

Although SMIS seems to be the most obvious choice in probing environment to elucidate structural and chemical properties of a system of interest, there exist several fundamental hurdles to overcome in order for this methodology to be successful. It is not without its limitations. One of the challenges that must be surpassed is the lack of signal that is emitted from one molecule. Careful, and sometimes laborious, sample preparation must be performed to remove and reduce any, if not all, of the background fluorescence that maybe present and capable of swamping out the emission of the probe molecule. It can also be difficult to achieve loading density of the probe molecules such that they can be spatially resolved. Due to the low signal to noise ratios that are present, these methods generally require specialized and often expensive detectors and optical equipment that reduce noise and efficiently collect as much of the signal as possible. Although it is theoretically possible to create an ensemble measurement by compiling individual

responses of a large number of molecules, it is often very impractical to do so based on the time requirements and the large number of samples required.

#### **5.4. Summary**

Many Fluorescent techniques have the ability to measure molecular interactions and probe environmental heterogeneity while simultaneously imaging areas of sample materials. These capabilities show promise in characterizing nanostructured materials in ways to provide information about the internal structure and dynamics to scale that have been previously unattainable for porous membranes.

## **6. CHARACTERIZATION OF INORGANIC POROUS MEMBRANES VIA SINGLE MOLECULE IMAGING SPECTROSCOPY**

### **6.1. Chapter Abstract**

Mesoporous silica membranes fabricated by the surfactant templated sol-gel process have received attention because of the potential to prepare membranes with a narrow pore size distribution and ordering of the interconnected pores. Potential applications include ultrafiltration, biological separations, and drug delivery, as well as separators in lithium-ion batteries. Despite advancements in synthesis and characterization of these membranes, a quantitative description of the membrane microstructure remains a challenge. Currently the membrane microstructure is characterized by the combination of results from several techniques, i.e. gas permeance testing, XRD, SEM, TEM, permoporometry. The results from these ensemble methods are compiled and the data fitted to a particular flow model. Although these methods are very effective in determining membrane performance, general pore size distribution, and defect concentration, they are unable to monitor molecular paths through the membrane and quantitatively measure molecular interactions between the molecular species and pore network. Single molecule imaging techniques enable optical measurements that probe materials on nanometer length scales through observation of individual molecules without the influence of averaging. Using single molecule imaging spectroscopy, we can quantitatively characterize the interaction between the probe molecule and the interior of the pore within a mesoporous silica membrane. This approach is radically different from typical membrane characterization methods in that it has the potential to sample the underlying pore structure distribution spatially, the surface energy, and the transport properties. This new fundamental knowledge can be quantitatively linked to both the preparation and the performance of membranes, leading to the advancement of membrane science and technology. Fluorescent molecules, 1, 1-dioctadecyl-3, 3, 3, 3-tetramethylindocarbocyanine perchlorate (DiIC-18), used to interrogate the available free

volume in their vicinity, were loaded into the mesoporous silica membranes at subnanomolar concentrations. The mesoporous silica films were prepared using a non-ionic ethylene oxide-propylene oxide-ethylene oxide tri-block copolymer surfactant, Pluronic P123, on single crystal silicon substrates using dip coating of a silica sol. Membranes were prepared resulting in an average pore diameter of approximately 5 nm as measured by helium, nitrogen permeance, and porosimetry. Fluorescent images and time transient experiments were recorded using a custom-built single molecule scanning confocal microscope at differing temperatures (10°C, 20°C, 30°C, 40°C, and 50°C). Time dependent polarization anisotropy was used to obtain the enthalpy of adsorption and Henry's law constant of the probe molecule.

## **6.2. Introduction**

Porous materials research is critical for the advancement of important technologies such as catalysis, adsorption, and separation. Inorganic membranes, a subset of porous materials, offer a promising replacement for current energy-intensive separation processes like distillation. In addition, the combining of separation and reaction into a one-step process via a membrane reactor is promising for increasing yields in thermodynamically limited reactions, such as hydrogen production from steam reforming. Examples of applications for separating lighter molecules include CO<sub>2</sub> separation from flue gas exhaust and from natural gas wells, separation of oxygen from air, and separation of ortho- and para-xylene for use as polymer feedstock<sup>102-105</sup>. It is further expected that membrane-based separations will play an important role in the biochemical industry as it continues to grow. A variety of inorganic membranes have been synthesized, characterized, and evaluated for a number of separations. An element of inorganic membrane research that has been lacking is the direct measurement of intrinsic membrane properties to include both thermodynamic (adsorption equilibrium) and kinetic (diffusivity) terms. The permeability of a species defines the ability of that species to permeate through the membrane, and is viewed as a critical parameter, in determining the species selectivity of a membrane. The permeability

coefficient is measured experimentally and reported as a “bulk” or averaged number. Careful experimentation, along with a physical model for diffusion and adsorption within the pores, can lead to the determination of bulk diffusion and adsorption constants through the membrane<sup>106-111</sup>. While this approach is useful in assessing the overall performance of a given membrane, it does not provide a detailed picture of the distribution of intrinsic diffusion and adsorption properties in a sample system, which is known to be spatially heterogeneous. In order to improve the specificity and performance of these promising membranes further, a detailed understanding of the underlying distribution of intrinsic properties is required. This level of detail mandates the development of new experimental approaches, along with improved physical models of the system. Understanding the distribution of intrinsic properties, both structural and thermodynamic, of membranes and linking this information to synthesis procedures and membrane performance is critical for further progress in this field.

Single molecule imaging techniques enable optical measurements that probe materials on nanometer length scales. These techniques obviate the need to average over large ensembles (bulk), making experiments highly sensitive to spatial or temporal heterogeneities. In particular, small variations in the local environment surrounding a probe molecule can induce dramatic changes in the observed fluorescence properties<sup>112, 113</sup>. These methods have found increasing application in the study of systems ranging from biology to solid-state materials where the observation and spatial correlation of static and dynamic disorder is of particular interest. For example, recent studies have demonstrated that single molecule methods can be used to visualize molecular level transport and local physical-chemical heterogeneities in uncalcined surfactant-filled and non-porous silica sol-gels. There has been increasing interest in extending the capabilities of single-molecule techniques to include the ability to determine surface dependent kinetic and thermodynamic quantities such as conformational exchange rates, free energies, and activation barriers.<sup>4, 78-84</sup> One area, however, which has not been widely explored by these methods, is the study of calcined porous silica thin film systems such as those being investigated



specifically for use as advanced membranes for chemical separation. Single molecule methods may be especially significant when pore sizes approach the molecular length scale, and typical gas permeance methods approach the limits of usefulness. On these length scales, single molecules become highly sensitive to both spatial confinement (pore geometry), and thermodynamic surface properties. Hence, working in the single molecule regime provides an avenue to correlate local environment with structural and thermodynamic properties (such as surface free energy), directly measuring the individual contributions to the distribution of intrinsic properties.

To achieve this goal, we have begun studying the dynamic behavior of individual fluorescent molecules confined within porous thin-film membranes using single molecule imaging spectroscopy (SMIS). Measurement of the intrinsic behavior of molecules on a local level will allow us to examine behavior that is washed out in typical ensemble measurements, directly obtaining and spatially correlating the distribution of molecular interactions with a distribution of physical properties, such as the probe molecule's heat of adsorption dependence on pore size, or pore shape. These measurements are expected to yield critical information that is useful in the design and synthesis of new classes of membranes as well as providing predictive information regarding their performance.

The physical system we chose to study consists of a mesoporous silica membrane prepared using a surfactant-template similar to MCM class of materials.<sup>114</sup> The synthetic procedure for this system is well developed and the resulting membranes have been thoroughly characterized for permeation of light gases and pore size distribution using standard membrane characterization techniques. These membranes, with pore sizes in the ~ 5 nm range, have applications in separating large molecules or acting as a support membrane to prepare hybrid organic-inorganic membranes with tailored surface properties for adsorption-enhanced separations<sup>4, 115, 116</sup>, however there is currently only limited information regarding the distribution of local intrinsic properties of these calcined mesoporous surfactant templated silica membranes.

In this study, we examined the molecular interactions of a commercially available dye molecule (DiIC<sub>18</sub>) within a mesoporous silica membrane with a mean pore size of 5 nm. To a good approximation, the optical transition dipole of this molecule lies along the molecular axis and is not expected to vary significantly. This allows for a simple correlation between optical dipole and molecular orientations. Molecular rotational dynamics were observed for three cases at varying temperatures using SMIS: in water (no molecular restriction), on a non-porous surface (strong surface interaction), and in the mesoporous membrane (pore confinement and surface interaction). Data were collected for the time-dependent orientation of individual molecules within these three environments. The orientation was correlated to a model that restricted both dipole rotation through pore confinement and dipole jump frequency through temperature reduction. The molecular rotational restriction (measured as the polarization) was correlated to Henry's Law describing adsorption equilibrium at low loadings within the pore. Intrinsic Henry's law constants for individual molecules were determined for the two solid surface experimental conditions. As expected, the strongest thermodynamic interaction of the molecule was within the pore. This application of SMIS towards studying intrinsic properties for individual molecules in membranes holds promise for further studies of intrinsic thermodynamic and kinetic properties of membranes.

### **6.3. Experimental**

#### **6.3.1. Sample Preparation**

Silica membranes were synthesized using tetraethylorthosilicate (TEOS) silica sol-gel templated with the non-ionic tri-block copolymer Pluronic P123 (EO<sub>20</sub>PO<sub>70</sub>EO<sub>20</sub>, MW = 5800, BASF).<sup>114</sup> The synthesis of the mesoporous silica thin films was performed in a two part solution series. A mixture of 2.7 mL of deionized H<sub>2</sub>O, 2.7 mL diluted HCl (pH 2.0), 6 mL EtOH (200 Proof), and 5.55 mL TEOS were stirred for 20 minutes. Then a solution consisting of 3.05 gm P123 and 24 mL EtOH (200 Proof) was added to the previous TEOS solution and aged for 20

minutes to produce the final sol (molar ratio of 1 TEOS: 20 EtOH:12 H<sub>2</sub>O: 0.0015 HCl: 0.021 P123) for dipping.<sup>114</sup> The silica sol-gel was then dip coated onto Fisher Premium cover slips (25mm x 25mm -1). Prior to dip coating, the substrates were ultra-sonically cleaned in subsequent baths of pentane, acetone, EtOH for 5 minutes respectively and blown dry with nitrogen between each treatment. The cover slips were boiled in a 10% by volume H<sub>2</sub>O<sub>2</sub> (30%) and 90% NH<sub>3</sub>OH (30%) solution for 10 minutes. After boiling, the solution was diluted with running water and the cover slips were blown dry with nitrogen. The resulting surfaces were left free of surface adsorbates, and sufficiently hydroxylated to ensure compatibility with the sol-gel film chemistry. After dip coating, the films were allowed to dry in atmosphere for 24hrs before being calcined to complete the hydrolysis of the silica precursors and to remove all of the templating surfactant, yielding an unobstructed silica porous network. This was accomplished in a humid environment at 400°C for a period of 4hrs with a ramp rate of 1°C/min.

The final as-synthesized samples were doped, by drop wise addition, with picomolar concentrations of 1, 1-dioctadecyl-3, 3, 3, 3-tetramethylindocarbocyanine perchlorate (DiIC<sub>18</sub>), (Figure 6.1), an amphipathic fluorescent dye, in spectroscopic grade pure n-hexane. The capillary forces within the membrane systems are such that hexane solution has been known to wet the membranes<sup>114, 117</sup>. This dye has previously been used as a probe of lateral diffusion in both model and cellular lipid membranes. The samples were washed twice with pure n-hexane and blown dry between each wash to remove any excess dye from the surface of the samples. Finally, the samples were inverted and mounted on a temperature-controlled xyz stage of the confocal imaging microscope.

In addition to the mesoporous membrane films, DiIC<sub>18</sub> molecules were studied in two other environments; in solution, and dry on a clean cover slip. These samples were used to establish the behavior of DiI under two limiting conditions; (1) where molecular rotation is not influenced by surface interactions and (2), in a pore of infinite radius where rotational hindrance is only a result of surface interaction. Sample solutions were prepared using sub-nanomolar

concentration of DiI<sub>18</sub> in 18 MΩ water in 100 micro liter well glass slides (Fisher Brand) covered with size #1 glass coverslips and sealed using Cytoseal-60 mounting medium. Dry samples were prepared by spin casting (3000 rpm maximum) a 30 μL aliquot of ~1 pm DiI in pure hexanes onto clean dry coverslips. In all cases, the cover slips were cleaned with multiple washes of pure ethanol and blown dry in nitrogen.

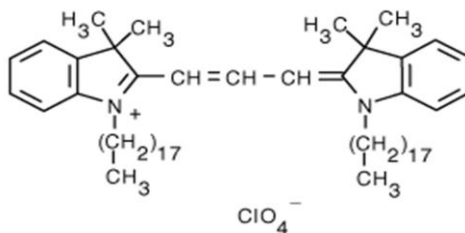


Figure 6.1 The molecular structure of the fluorescent dye used. 1, 1 - di(3,3,3,3 - tetramethylindol - 5 - yl)ethane perchlorate; Molecular Weight = 933.88 gm/mol

### 6.3.2. Preliminary Fluorescence studies

Initial experiments were performed on loaded samples synthesized by the procedure described above. The primary goals of these basic experiments were to determine whether single molecule imaging could be carried out on a mesoporous silica membrane. As very few single molecule studies had been attempted prior to these studies with these materials, we were unsure of the success and quality of the information that could be obtained. Several questions need to be answered in order for single molecule spectroscopy techniques to be successfully applied to mesoporous silica membranes.

1. What was the intensity of intrinsic fluorescent signals that are present in mesoporous silica membranes? If the silica membranes exhibited a fluorescent signal it could contribute to the background fluorescent signal and potentially swap the single molecule signals.

2. What were the protocols for loading the membrane to achieve an areal density required for single molecule imaging?
3. Could these membranes be loaded with fluorescent molecules at concentrations low enough to produce single molecule features?
4. Would the membrane surface make the fluorescent probe inactive via such routes as, quenching or chemical reaction?
5. Finally, would fluorescent molecules be reliable reporters of the membranes local environments?

To answer these questions, mesoporous membranes were loaded with varying concentrations of DIC<sub>18</sub> ranging from micromolar down to picomolar levels as described above in section 6.3.1. The as synthesized loaded samples were then inverted and placed in a scanning confocal microscope with a focal depth of approximately 1  $\mu\text{m}$ ; the specific components and operation of the microscope are discussed below in section 6.3.3. The sample was inverted to ensure all studies were monitoring fluorescent molecules that had penetrated the porous network. Even with careful washing and meticulous protocols without inversion of the sample, there is no way to discern that the probe molecule monitored was inside the porous network and not on the surface of the membranes, see Figure 6.2.

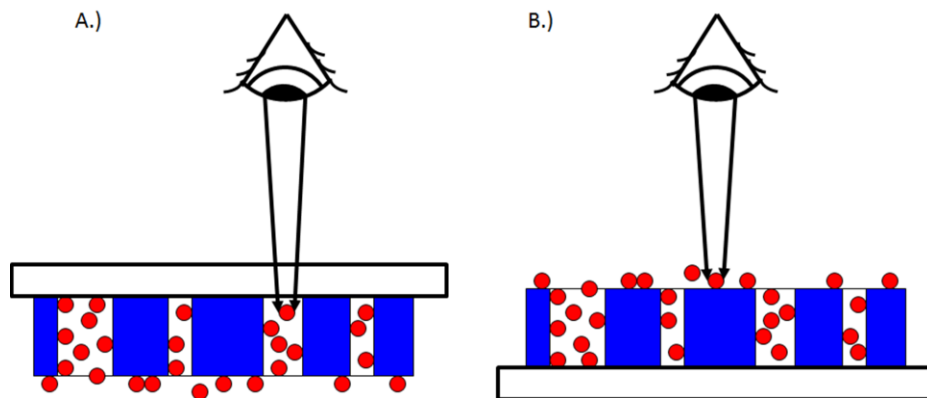


Figure 6.2 A figure showing the two sample orientations for imaging. A.) Is inverted and the detector is focus just below the quartz glass. B.) is upright and is focused on the top of the sample membrane. As shown by the two opposing orientations figure B.) is incapable of ascertaining whether the probe molecule is within the pore or on top of the membrane. The membrane is shown in blue, the fluorescent molecule is red, the quartz slide glass is shown in white/ black boarder and the detector is depicted as an eye.

Once placed into the microscope, areas of the samples were scanned to measure the areal density of the  $DIC_{18}$  to determine the optimum loading concentration to achieve single molecule features that are spatially resolved. At higher loading concentrations, step photobleaching experiments were performed to qualitatively measure the appropriate loading concentration and robustness of the fluorescent probe within the silica membrane, Figure 6.3. The loading concentration of the probe molecule was reduced until single molecule features were observed, Figure 6.4.

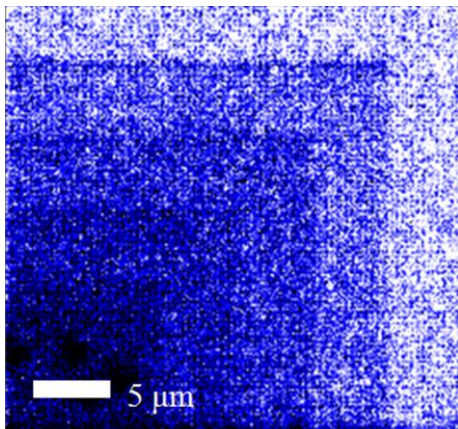


Figure 6.3 An example of successive step photobleaching experiments.

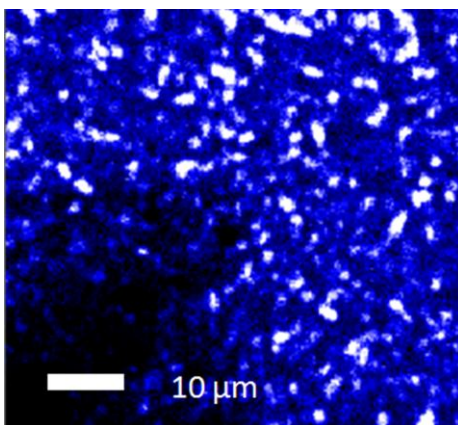


Figure 6.4 An example image showing single molecule features.

Once the loading concentration that produces a doped sample exhibiting single molecule features was determined, picomolar levels, membrane defect areas were imaged and treated as analogous to large pores. The fluorescent emission was split into orthogonal polarizations and imaged independently by raster scanning the sample area, Figure 6.5. It was required to remove the background signal before preliminary analysis to quantify the probe molecules sensitivity to the local environments within the porous membrane. To remove the background due to stray fluorescence and digital noise, every point from each raw image that was greater than the mean

plus one standard deviation (known due to the use of APD) was removed. A new mean was calculated for each resulting data set. This process was continued until the mean no longer changed. The final unchanging mean was used to generate a mask of each channel, through which the raw images are then processed to remove the underlying background signal, any point in the image below the mean. Finally, the polarization of each pixel within the images was calculated using Equation 6.1, where  $\bar{x}_i$  and  $\bar{y}_i$  are the x and y coordinates of the  $i^{\text{th}}$  pixel in each image, to generate a 2-d representing the calculated polarization of the fluorophores present in the system, Figure 6.6.

Equation 6.1 
$$P_i = \left| \frac{\bar{x}_i - \bar{y}_i}{\bar{x}_i + \bar{y}_i} \right|$$

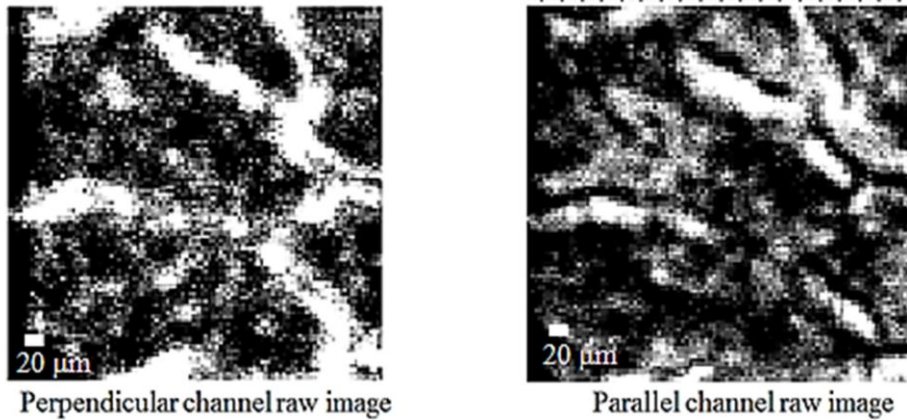


Figure 6.5 An example image of a defect area image in two orthogonal polarizations.



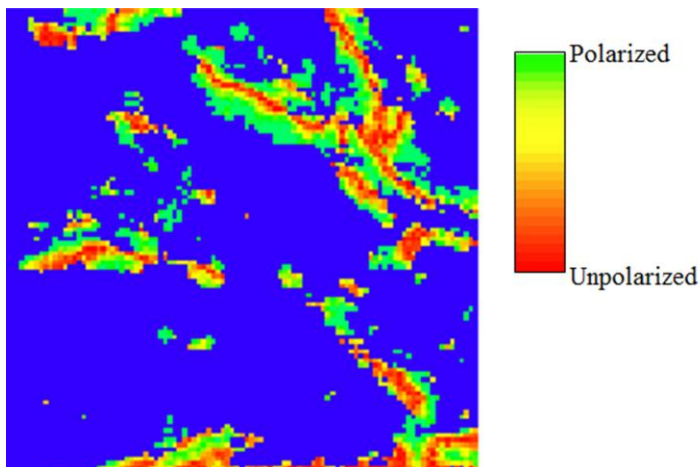


Figure 6.6 A 2-D histogram showing the various polarization states of DiIC<sub>18</sub> within a defect area in a silica membrane.

As can be seen in Figure 6.6, area in the middle of the defects appear as red and correlate to molecules that emit signals in both channels equally, up and down and side to side. This observation is indicative of molecules that are freely rotating. However, molecules along the edges of the fissures are polarized, shown in green, meaning that these molecules are stationary. This observations and preliminary tests demonstrate that DiC<sub>18</sub> can be loaded at concentrations appropriate for single molecule imaging, Figure 6.4, and they are sensitive reporters of the local environments within a porous silica membrane, Figure 6.6, as such, have warranted further studies.

### 6.3.3. Instrument

All fluorescence data were collected in a custom-built laser scanning confocal microscope (LSCM) (Figure 6.7). Uniform excitation of DiIC<sub>18</sub> molecules having arbitrary orientation in the sample plane (XY) was accomplished by passing the linearly polarized output of a 532 nm solid state diode laser through a quarter wave plate (Melles Griot) yielding circularly polarized light. This light was directed towards the sample using a 532 nm long-pass dichroic

beamsplitter (Chroma, Inc.) and focused to a near diffraction limited area on the sample using a high numerical aperture (1.3 NA) oil-immersion objective. Fluorescence emission was collected in reflection using the same objective. After passing through the dichroic beamsplitter, the fluorescence signal was split using a broadband polarizing cube beamsplitter (Newport Inc.) directed into two orthogonal detection channels. The resulting signals were detected with two low dark count (<25 dark counts/second) avalanche photo diodes (APDs) operating in Geiger mode, providing single photon sensitivity. Samples were mounted on a thermoelectric heater/cooler allowing the temperature of the samples to be varied from 5 to 80°C ( $\pm 1$  °C).

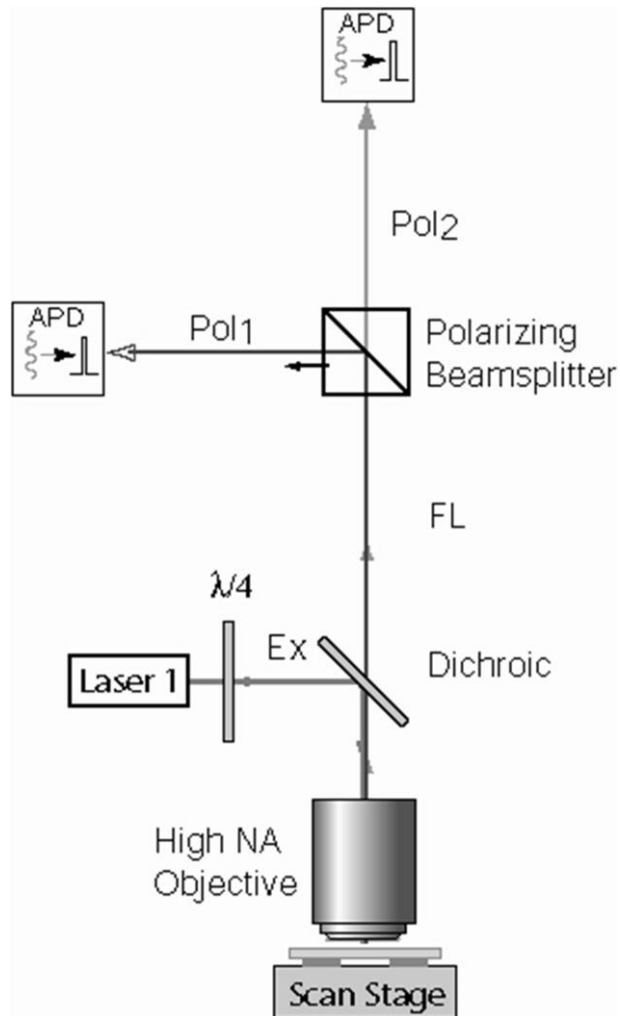


Figure 6.7 Schematic of the two channel laser scanning confocal microscope.

Images were obtained point-wise by raster scanning (Figure 6.8) the sample relative to the excitation and collection optics. While in theory, this instrument is able to obtain a series of photon timestamps at each image pixel, the spatial disparity of the single molecule samples makes this time-consuming and unnecessary. In practice, a 2-dimensional image ( $20\mu\text{m} \times 20\mu\text{m}$ ) is obtained with pixel dwell times just long enough to resolve individual fluorescence features ( $100\ \mu\text{s} - 1\text{ms}$ ). The positions of single molecule features were identified and the scan stage directed to interrogate each feature separately. Polarization-dependent single molecule data, in

the form of individual photon arrival times (timestamps), were obtained for a period of 10 seconds with 12.5 ns temporal resolution. This raw data can be binned in time, generating the familiar intensity trajectories.

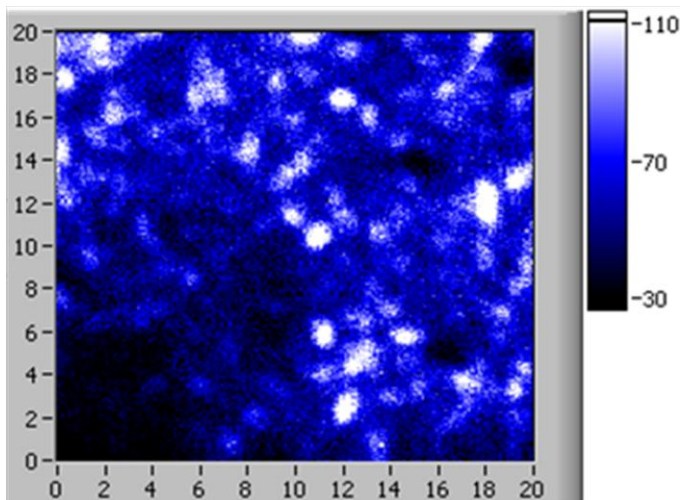


Figure 6.8 An example image via raster scanning to locate single molecule features

We refer to this method as point-probe mode (PPM). Here, relatively long bin times ( $100\mu\text{s}$ ) were used to improve the signal-to-noise ratio, and to verify the sensitivity of our approach under typical sampling conditions. All scanning and data acquisition operations were controlled using a custom LabView (National Instruments) interface. Ten images of the dyed samples were recorded at varying temperatures (10, 20, 30, 40, and  $50^\circ\text{C}$ ). Within each image, at least three sequential timestamp records (maximum of 10 seconds or 200,000 counts) were obtained for each of ten single molecule features.

#### 6.4. Data Handling

All of the timestamp records for the single molecule features were saved into a text file with the photon arrival times recorded for each APD recorded as grouped pairs. The handling and calculation steps of all of the recorded data sets were performed with a number of LabView

VIs and Mathematica programs written specifically for this project. Attempts were made to create a single program package to perform all of the data manipulations and analysis. However, the volume of data proved to be too large for the available computers to handle such a task.

The paired timestamps were converted into time courses with 100  $\mu$ s bin width using a written LabView VI, the user interface panel is shown in Figure 6.9. The resulting time courses were grouped with all other time courses recorded at a given temperature and saved as text files and for importing into another LabView VI for the calculation of Polarization Values. Polarization was calculated using Equation 6.1, for each pair of timecourse files shown in Figure 6.10, and then binned into a 2-D histogram. The 2-D histogram counted the number of occurrences that a polarization value occurred at a specific value of total counts shown in Figure 6.11, with the wire diagram show in Appendix C.

Once the 2-D histogram had been created, it was saved as a matrix text file. It was imported into a second Mathematica program; code shown in Appendix D; for thresholding and condensing into a 1-D histogram discussed in section 6.6.

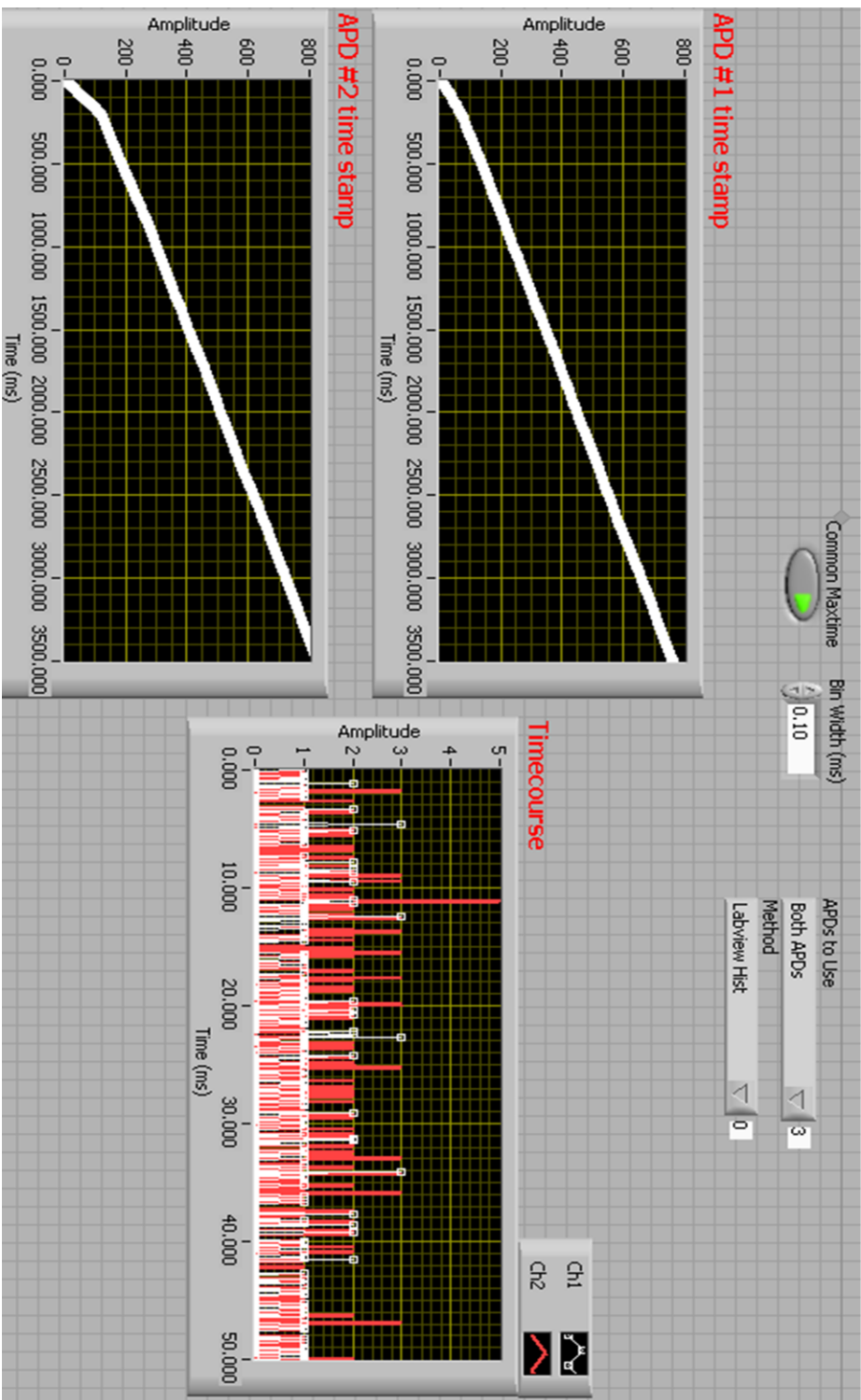


Figure 6.9 Screen capture of the VIs front panel. The VI used to convert the timestamped photon arrival times into binned time courses. Rotated for readability

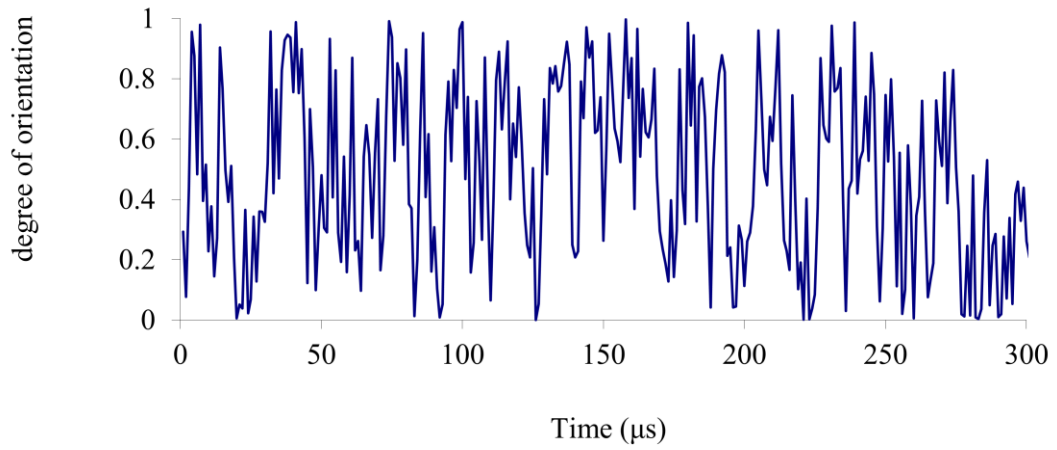


Figure 6.10 An example Polarization time course

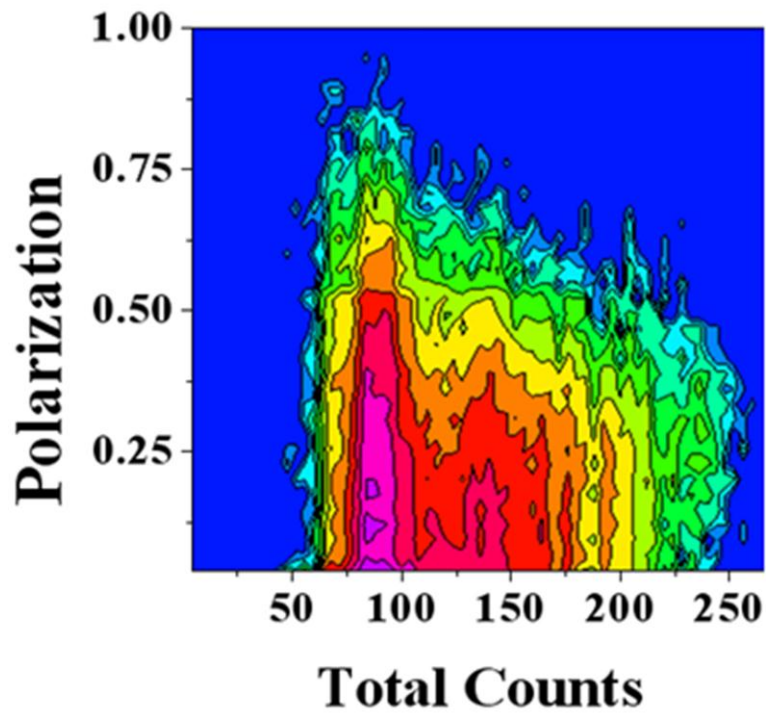


Figure 6.11 A 2-D histogram of the polarization values versus the total counts. With the lightest colors show areas of the highest occurrence of a specific polarization and count combination

## 6.5. Model and Simulation

The physical picture used as the basis of the mathematical model consists of a rigid molecular dipole entrapped in a cylindrical pore oriented normal to the membrane surface with a diameter of the same approximate magnitude as the dimensions of the molecule, shown in Figure 6.12. A Monte Carlo random walk on a sphere model was created in Mathematica, code found in Appendix D, to generate simulated instantaneous 3D dipole orientations, and subsequently the time dependent polarization under various conditions.

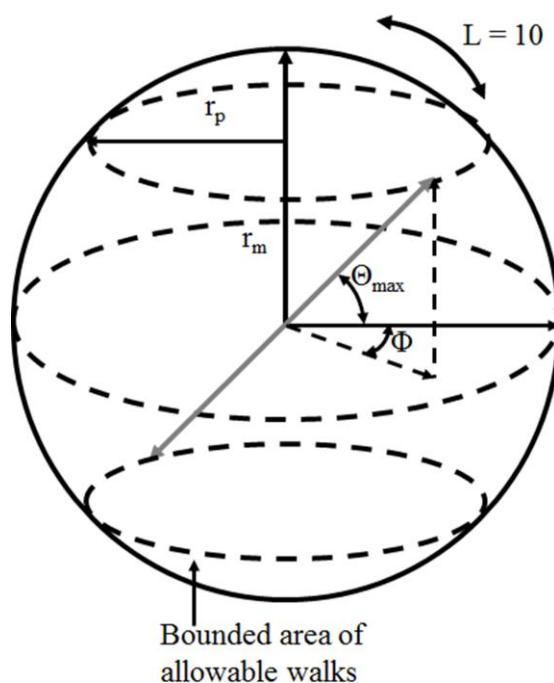


Figure 6.12 A physical picture of the random walk on a sphere model. For pore size-dependent molecular dipole orientation demonstrating the bounded area for allowable orientations,  $\Theta_{max}$ , and the walk distance,  $L$ .

To simplify this picture it is assumed that: 1) the dye concentration is low enough that there are no interactions between neighboring dye molecules, 2) all collisions between the molecule and pore walls are elastic, and 3) there is no translational motion. Under these conditions, the rotational motion of a molecule with dimension  $r_m$ , moving in a pore of radius  $r_p$ , can be described by following the relative magnitudes of the x and y components of transition



dipole projected onto the xy-plane. Using the random walk on a sphere model, a series of positions on a sphere were generated randomly in spherical coordinates ( $R$ ,  $\Phi$ , and  $\Theta$ ) which were converted into  $x$ ,  $y$ , and  $z$  magnitudes using the spherical transforms, Equation 6.2, consistent with the experimental geometry, it was assumed that the intersecting plane used to bind the point's walk is in the xy- plane, and the imaging objective is oriented along the z-axis.

$$\begin{aligned} \text{Equation 6.2} \quad x &= R \sin(\phi) \cos \theta \\ y &= R \sin(\phi) \sin(\theta) \\ z &= R \cos(\phi) \end{aligned}$$

While the random walk model allowed  $\Phi$  and  $\Theta$  to vary randomly, the step length ( $L$ ) on the surface was fixed for each step and corresponded to a total angular displacement of  $\pi/4$  radians. In the case that a molecule is free to rotate in solution or in a large pore where  $r_p \gg r_m$ , the range of motion encompasses all displacement angles ( $0 \leq \Phi \leq \pi$ , and  $0 \leq \Theta \leq 2\pi$ ). The effect of pore confinement on rotational motion was modeled by reducing  $r_p$ , relative to the molecular dimension ( $r_m$ ), represented by restricting the maximum value of  $\Theta$  to  $\Theta_{\max} = \arcsin(r_p/r_m)$  (Figure 6.12). The effect of temperature on the rotational rate was represented by increasing the number of steps per unit time with increasing temperature.

For a given pore size ( $r_p$ ), and temperature, the simulated  $x$  and  $y$  magnitudes were scaled to account for loss of amplitude into the  $z$ -axis when passing through a high numerical aperture objective during imaging<sup>118, 119</sup>. To convert these values into timecourse, the  $x$ , and  $y$  amplitudes were averaged over multiple steps; the number of which is determined by the temperature dependent reorientation time of the free molecule. For example, based on the literature values for comparable dyes, the time interval for each step ( $L$ ) can be estimated from the anisotropic reorientation times ( $\tau_r$ ), for DiIC<sub>18</sub> to be  $\sim 6 \times 10^{-10}$  s at 10°C<sup>120, 121</sup>. From this value, the root-mean-squared angular displacement ( $\overline{\Delta\theta}$ ) can be calculated, in radians, using the relationship:

Equation 6.4

$$\langle \overline{\Delta\theta^2} \rangle^{1/2} = \left( \frac{2\Delta t}{\tau_r} \right)^{1/2}$$

where  $\Delta t$  is the observation time. This corresponds to approximately 20 steps of length  $L$  ( $\pi/4$  radians) in the experimentally relevant 1 ms integration period. At elevated temperatures, we expect the reorientation time to decrease according to the well-known Stokes-Einstein-Debye (SED) relationship:

Equation 6.3

$$\tau_r = \frac{\eta(T)V}{kT}$$

Where  $\eta(T)$  and  $V$  are the temperature dependent solvent viscosity and the molecular volume, respectively,  $k$  is the Boltzmann constant, and  $T$  is the absolute temperature. The number of steps per 1 ms window increases non-linearly to approximately  $2 \times 10^4$  at  $50^\circ\text{C}$ , due to the additional dependence of the viscosity on temperature.<sup>122</sup> After binning over the appropriate number of steps per 1 ms interval, Poisson distributed noise is added to each bin, resulting in model generated data analogous to the two channel time binned data recorded by the SMIS technique.

## 6.6. Results and Discussion

As with most methods involving labeling at single molecule levels, optimal labeling must be determined iteratively. As such, a series of mesoporous films were systematically loaded with serial dilutions of  $\text{DiC}_{18}$  in hexanes and imaged in the LSCM until the desired concentration density of  $\sim 1$  molecule/ $\mu\text{m}^2$  was achieved. The presence of individual molecules was confirmed by the observation of diffraction limited features in the LSCM images and rapid single step bleaching or fluorescence intermittency to the background level.<sup>123</sup> This corresponded to a solution concentration of 500 pM.

Once the appropriate concentration was established; at each temperature, ten separate 20  $\mu\text{m}$  x 20  $\mu\text{m}$  areas were imaged and ten single molecule positions were identified for PPM acquisition in each image. At each of these points, three sequential timestamp records were collected, allowing for the eventual observation of single step photobleaching, confirming that only a single molecule was present. Each time stamp record consisted of 2 orthogonal polarization channels (x and y) recorded for a maximum of 10 seconds.

The raw data generated by the SMIS method consists of individual photon arrival times, (time stamps), recorded with 12.5 ns precision for both the x and y channels. Because the fluorescence lifetime of DiIC<sub>18</sub> is approximately 1 ns, the probability of measuring a photon in both channels in each 12.5 ns window is low, making an accurate determination of the *instantaneous* molecular orientation impossible. To account for this issue, the individual instantaneous values of x and y were binned for a period of 100  $\mu\text{s}$ . This time was chosen to improve photon-counting statistics in both channels and in all sample types including those where pore confinement and surface interactions lead to slow reorientation times. After temporal binning, the intensities of the two time courses provide the time averaged x and y components ( $\bar{x}$ ,  $\bar{y}$ ) of the dipole orientation in each 100  $\mu\text{s}$  window. The degree of orientation, represented by the polarization (P), was then calculated for each bin period for both the simulated and experimental data using the relationship shown in Equation 6.1, where  $\bar{x}_i$  and  $\bar{y}_i$  are the  $i^{\text{th}}$  elements of each binned time series. For convenience, the absolute value was applied to the polarization creating single sided data. The rotational behavior of each sample type can then be represented as a histogram over all P values, with characteristic mean ( $\bar{P}$ ) and width ( $\Delta P$ ). Generally, large values of  $\bar{P}$  indicate that the molecules within the sample remained aligned in either the x or y channel during the observation time. Individual values of P and values of  $\bar{P}$ , approaching zero, occur when the molecules present rotate so rapidly relative to the bin interval, as to sample all orientations with equal probability, or alternatively just happen to remain fixed at

an angle lying equidistant between the x and y axes. While the latter case is highly improbable for solution samples, or where signal is averaged over extended periods, the former case is consistent with Equation 6.4 and indicates that P is proportional to  $\tau_r/\Delta t$ , where  $\Delta t$  represents the single molecule observation time.

As is the nature of all single molecule measurements, the photon count rate is severely limited, making calculations like Equation 6.1, highly subject to the effects of noise. For example, if the molecule is freely rotating ( $P = 0$ ), but the signal-to-noise is low in both channels, a positive statistical noise fluctuation in  $\bar{x}_i$  ( $+\sigma \bar{x}_i$ ) and a corresponding negative fluctuation in  $\bar{y}_i$  ( $-\sigma \bar{y}_i$ ) could result in a relatively large value of P. If a significant number of 100  $\mu\text{s}$  bins fall into this category (where the signal-to-noise ratio is small), then a resulting distribution of P-values, and consequently its average value ( $\bar{P}$ ), would not accurately represent the single molecule data. An example of this is shown in Figure 6.12, where the distributions of polarization values for DiIC<sub>18</sub> dry on glass, are compared. Little difference between the two distributions is observed, whereas for a significant increase in temperature (where kT is of the same order of magnitude as the surface interaction potential) some shift in P due to complete or partial desorption might be expected. This suggests that an understanding of the sampling noise is necessary to interpret the polarization data properly.

For single photon counting measurements, like those described here, the measurement noise for each counting period is very accurately represented by Poisson statistics. A Poisson process is defined as a continuous time counting process and has the following requirements; there is a zero probability that two arrivals occur at the same time, the number of arrivals in the future is independent of the past, and finally the number of arrivals in any time interval is only dependent upon the length of the time interval. In a Poisson process, the probability, p, of a number of events (n) occurring in N trial is given by the limit of a binomial distribution, illustrated in Equation 6.5.

Equation 6.5 
$$B(n | N) = \frac{N!}{(N-n)!n!} p^n (1-p)^{N-n}$$

If one knows only the number of expected events ( $\lambda$ ) that occur within a given time frame but not the number of individual trials ( $N$ ), or the probability of an event occurrence ( $p$ ), within a trial, the binomial distribution must be redefined based on the number of expected events<sup>124</sup>, Equation 6.6;

Equation 6.6 If  $\lambda = Np$  substituting  $\frac{\lambda}{N}$  for  $p$  into Equation 6.5 and taking the limit as  $N \rightarrow \infty$ .

$$B(n | N) = P(n) = \frac{\lambda^n e^{-\lambda}}{n!}$$

where  $\lambda$  is a positive real number representing the expected mean number of occurrences within a given time interval,  $n$  is a positive integer representing the number of real occurrences in that time interval. Poisson distributions possess a unique property. The parameter,  $\lambda$ , not only represents the mean expected value for events; in this case the number of photons arriving in a time interval, but is also equal to the variance of number photons arriving in total observation time, Equation 6.7

Equation 6.7 
$$\text{var}(X) = E(X^2) - (E(X))^2$$

If the distribution is Poisson in nature the expected distribution is:

$$E(X) = \lambda$$

Therefore 
$$\begin{aligned} \text{var}(X) &= (\lambda^2 + \lambda) - \lambda^2 \\ \text{var}(X) &= \lambda \end{aligned}$$

The implication is that the number of photons arriving fluctuates around the value of  $\lambda$  with a standard deviation equal to  $\sqrt{\lambda}$ . It is this unique correlation of Poisson distributions that is useful in single molecule spectroscopy<sup>125</sup>. By monitoring how the fluctuation varies with the mean signals generated by different populations, one can estimate the contribution of subtle changes between each population even if that contribution is too small to be detected directly<sup>126</sup>. Conversely, these properties can be used to determine theoretical minimum detection limits and the identification of suspect data.

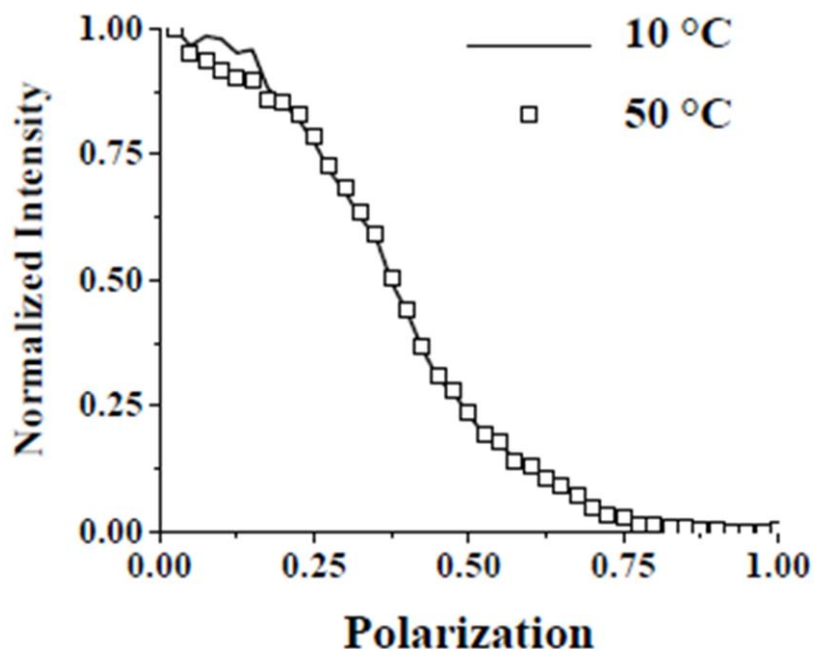


Figure 6.13 1D histograms of DiIC18 dry on glass. The data was recorded at 10 and 50 °C and is shown without an applied threshold.

For a Poisson distributed variable, such as the average number of counts in each 100  $\mu\text{s}$  time bin ( $N$ ), the standard deviation is equal to  $N^{1/2}$ . If we let  $N_x = \bar{x}_i$  and  $N_y = \bar{y}_i$ , then the total number of photons counted is  $N_T = N_x + N_y$ , and the difference is  $\Delta N = |N_x - N_y|$ , corresponding to the denominator and numerator of Equation 6.1, respectively. Applying the

usual rules for error propagation to the calculation of P, and assuming that  $N_x$  and  $N_y$  are largely independent, we obtain the following function relating the expected standard deviation in the distribution of P values,  $\Delta P$ , to the total number photons counted in both channels.

$$\text{Equation 6.8} \quad \Delta P = \frac{\sqrt{N_T^2 + \Delta N}}{N_T^{3/2}}$$

If we consider the limiting case that a molecule is freely and rapidly rotating ( $P = 0$ ) such that  $\Delta N = 0$ , then Equation 6.8 simplifies to  $\Delta P = N_T^{-1/2}$ . At the other extreme, if we consider the case of a molecule fixed along the x-axis ( $P = 1$ ), then  $N_y = 0$ ,  $N_T = N_x$ , and  $\Delta N = N_x$ , and we obtain  $\Delta P = \sqrt{2}N_T^{-1/2}$ . Due to the presence of constant and randomly oriented background fluorescence ( $\sim 20$  kHz), in addition to dark counts arising from the detectors (50 Hz), the latter case is never observed in practice. Hence, we conclude that the uncertainty in the average polarization ( $\bar{P}$ ) for a given system is inversely proportional to the square root of the average total number of counts ( $\bar{N}_T$ ) in 100  $\mu$ s. To visualize the dependence of the range of observed P values on the expected signal-to-noise ratio, the polarization data, at  $T = 10^\circ\text{C}$ , are plotted as a 2D histogram (Figure 6.14 A). Here the variance in the observed values of P clearly decreases as the number of photons counted in each 100  $\mu$ s time bin increases. In order to remove any suspect data, a statistical threshold is applied based on the average total counts ( $\bar{N}_T$ ) is obtained from the mean of all  $N_T$  values. A threshold of  $\bar{N}_T + 2\sqrt{\bar{N}_T}$  was then applied to the individual polarization timecourses. Any data stream with a mean value less than the threshold was removed in its entirety from the data set, yielding a data set with 99% confidence interval as shown in Figure 6.14 B. Once all of the data were thresholded, each data set for an environment at a given temperature is summed along  $N_T$  into a 1-D polarization histogram (Figure 6.15). It should be noted here that the while the thresholding technique significantly reduces the presence of large

individual  $P$  values resulting only from noise fluctuations, it also potentially removes from the  $P$ -histogram large  $P$  values associated with real single molecule events occurring with low signal-to-noise (small  $N_T$ ). This effect, combined with that due to use of a high NA objective (described above), results in  $P$ -histograms with smaller average values of  $P$ , than one might expect from a simple physical picture of randomly oriented dipoles<sup>84</sup>.



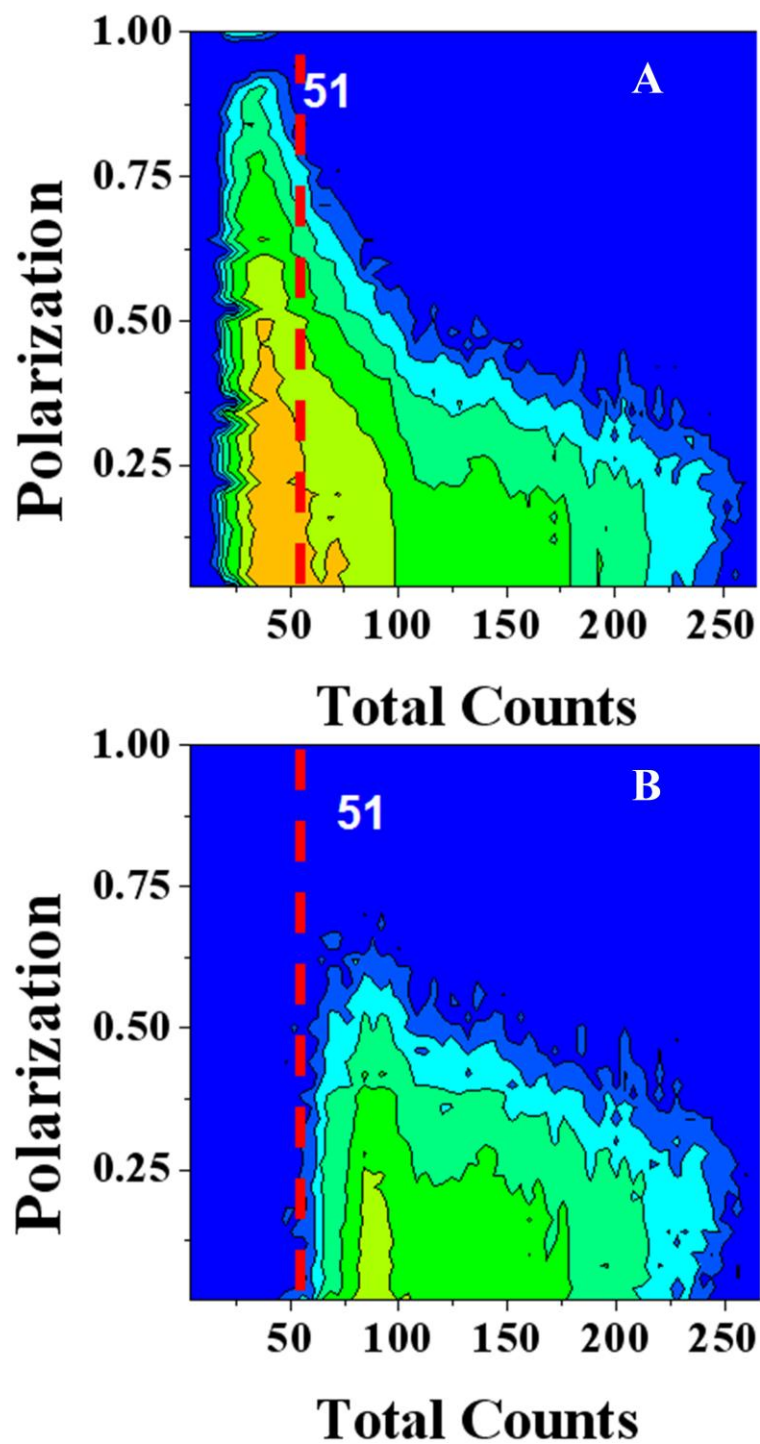


Figure 6.14 2D histograms of total intensity in counts.  $N_T$  vs. degree of polarization  $P$  for  $\text{DiIC}_{18}$  deposited on glass at  $10^\circ\text{C}$  before, A) and after, B) statistical thresholding is 51 counts.

A comparison of thresholded data for the three environments is shown in Figure 6.15. The average number of photons counted per 100  $\mu\text{s}$  bin ( $\bar{N}_T$ ) after applying the statistical threshold was approximately 125 kHz for all samples (slightly lower on the glass coverslip) and relatively constant across all temperatures used. This value includes a relatively large constant background level of  $\sim 20$  kHz in each channel. This background could in practice be subtracted from the signal before calculating the individual values of  $P$ . Due to the Poisson dependence of the uncertainty on the total number of photons counted, including background, there is no statistical advantage in doing so.

In Figure 6.15A, the polarization histograms of DiIC<sub>18</sub> rotating freely in water at three different temperatures are shown. As one would expect, increasing the solution temperature results in a decrease in the rotational time constant (Equation 6.3). Since the rate of reorientation of individual molecules, increases within the 100  $\mu\text{s}$  bin interval, the molecule can sample many more positions, resulting in a decrease in  $\bar{P}$  with increasing temperature. Though the apparent sensitivity of  $\bar{P}$  to relatively small changes in temperature is somewhat surprising, it is consistent with previously reported results,<sup>122</sup> and is likely due to the strong temperature dependence of the solvent viscosity (1.68 cP and 0.4 cP at 10°C and 50°C, respectively) and solute-solvent interactions. While difficult to correlate with a specific physical property, the observed behavior provides a baseline for temperature dependent changes in  $\bar{P}$ , in the absence of all surface interactions.

The polarization histograms for DiIC<sub>18</sub> deposited on glass as a function of temperature are shown in Figure 6.15 B. In this case, the dry glass surface is used to demonstrate the rotational behavior of an adsorbed molecule in a pore of infinite radius (plane), where deviations in rotational kinetics are due only to surface interactions and not by pore confinement. Unlike the freely rotating molecules in solution, even at elevated temperatures, the average polarization remains nearly constant at  $\bar{P} = 0.061 \pm .006$ . This indicates that there is little temperature-induced

change in molecular motion on the surface. The lower average polarizations observed for glass, relative to the other sample systems, is the result of a slightly lower average count rate in this system and the use of the statistical threshold. In fact, before applying the threshold, the relative number of measured orientations with large P values (Figure 6.13, and Figure 6.15 A) are greater on glass than that observed for the other sample types (not shown), as one would expect for a sample of randomly oriented dipoles. These larger polarization values appear to be a result of a lower total count rate ( $N_T$ ), and are removed by the threshold (Figure 6.14B). While this implies that we cannot directly compare the average polarizations between sample types, the statistical thresholding does allow for a quantitative assessment of the temperature dependence within a sample type.

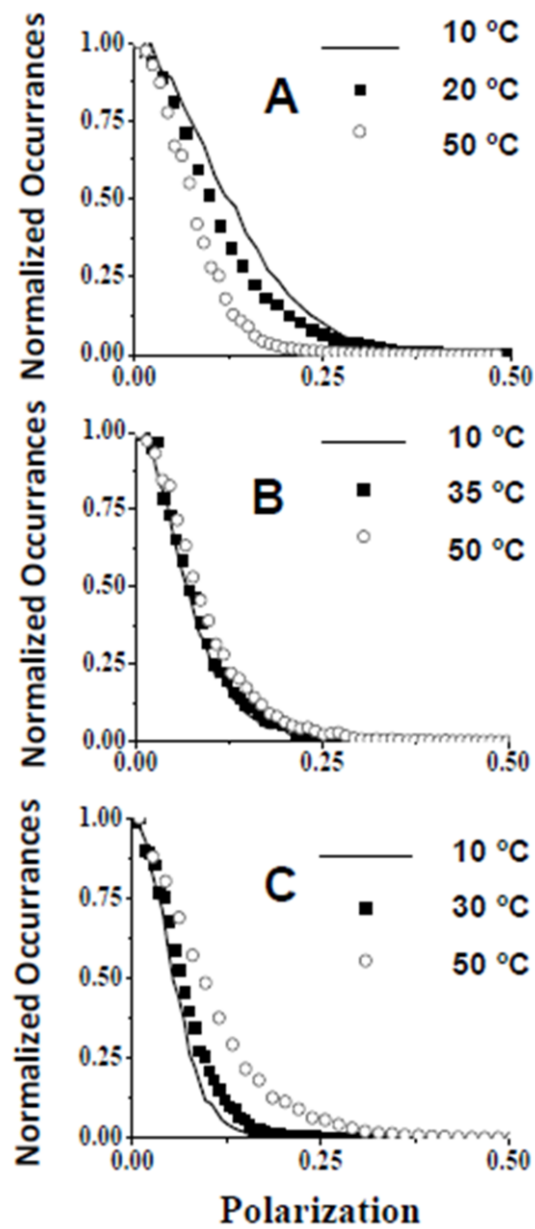


Figure 6.15 Normalized polarization histograms. A) is H<sub>2</sub>O, B) is dry on glass, and, C) is dry in a silica pore at three different temperatures. The thresholded instantaneous polarization values calculated from 10 s time stamp runs are binned into 100  $\mu$ s, indicating the reversal of temperature dependence of a dye molecule going from free in solution to an adsorbed state.

The polarization histograms for DiIC<sub>18</sub>, adsorbed within the pore structure of a silica membrane, as a function of temperature are shown in Figure 6.15 C. The average pore radius for this sample determined using porosimetry<sup>117, 127-129</sup> was found to be  $r \sim 2.5$  nm; a factor of only about 2-4 times larger than the molecular dimension of DiIC<sub>18</sub>. To a good first order approximation, the nature and energetics of each adsorption site (isolated silica hydroxyl) for the slide glass surface and the mesoporous film should be of the same approximate magnitude, owing to their chemical similarity. The chemical interaction between DiIC<sub>18</sub> and silica likely occurs between the amino groups on DiIC<sub>18</sub> and the isolated surface hydroxyls on the silica surface. In fact, this interaction has been used previously for the covalent attachment of aminosilanes on silica surfaces<sup>130, 131</sup>. While hydrogen bonding is highly likely, the magnitudes of the calculated enthalpies suggest that covalent interactions are dominant. For the porous silica film, the observed DiIC<sub>18</sub> rotational behavior is expected to be characteristic of both strong surface interactions and restricted rotational motion due to pore confinement. In stark contrast to the other sample types, a significant increase in  $\bar{P}$  is observed at elevated temperatures. Unlike the case of DiIC<sub>18</sub> deposited on glass, where strong uni-directional surface interactions are expected to inhibit motion, the observed temperature dependence in the pore suggests that there is at least some rotational motion present. However, when the molecule is free to sample all orientations with equal probability, as is the case for DiIC<sub>18</sub> in water, a reduction in  $\bar{P}$  with increasing temperature is observed. While these data do suggest an interplay of pore confinement and surface interactions, more information is needed to determine the relative magnitudes of the two competing affects. To identify the general influence of pore geometry on the observed temperature dependence of  $\bar{P}$ , in the absence of surface interactions, the rotational model described above was employed.

The simulated data shown in Figure 6.16 were obtained in the absence of pore restriction ( $r_p \gg r_m$ ) but where the number of steps per 1ms bin was varied to represent rotational rates consistent with 10, 20, and 50 °C (an effective temperature increase). After scaling, to be consistent with experimentally observed average photon count rates, the simulated data agree remarkably well with those obtained for the freely rotating dye (Figure 6.15 A), confirming that  $\bar{P}$  does decrease with increasing temperature, and validating the model's accuracy.

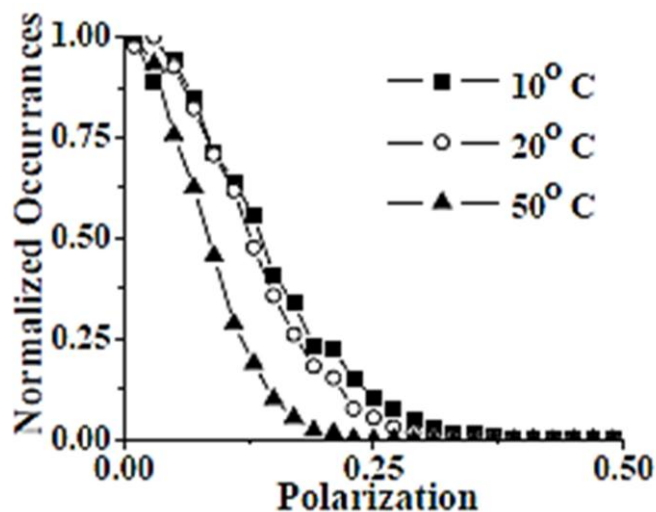


Figure 6.16 Model generated polarization histograms. The temperature ranging from 10 to 50 °C.

To model the influence of pore geometry on the temperature dependence of  $\bar{P}$ , a series of simulated data were generated where  $r_p$  was increased relative to  $r_m$ , while the step rate was held constant. A plot of  $\bar{P}$  versus  $1/T$  comparing the simulated and experimental data is shown in Figure 6.17. The results show that in the absence of surface interactions,  $\bar{P}$  consistently decreases with increasing temperature, regardless of the extent of geometric confinement. Based on their relative magnitude and slope the entire data set can clearly be differentiated into two groups. Only in the case where  $DIC_{18}$  is adsorbed on glass is the behavior exhibited representative of that observed in the mesopore. As such, it is reasonable to conclude that the temperature response

observed for the dye in the mesoporous film cannot be attributed to simple geometric rotational confinement of the molecular dipole. Therefore, the observed temperature response of the  $\bar{P}$  within a silica pore must be the result of molecule-surface interactions.

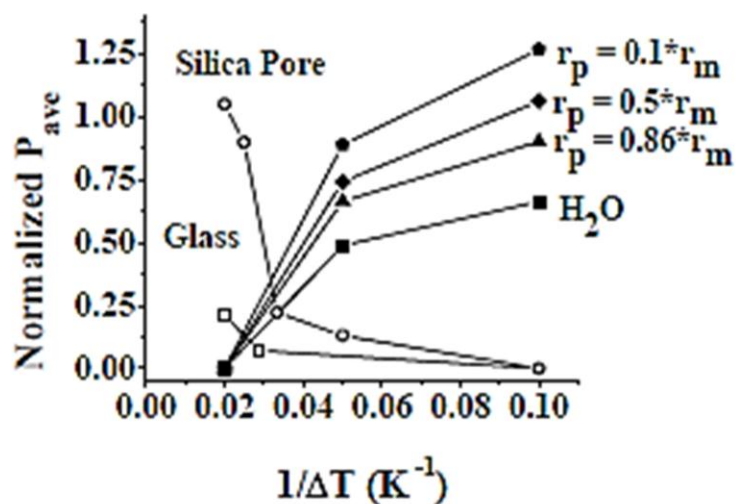


Figure 6.17 Comparison of the average polarization vs.  $1/\Delta T$ . For the experimental data collected for DiIC18 free in solution, dry on glass, in a silica membrane pore, and model generated. The results indicate that the model can mimic the data recorded for DiIC18 in solution but is an inaccurate depiction of the dye on a surface and within a mesopore.

In an attempt to quantify the nature of the molecules' interaction with the pore surface, a simple thermo-kinetic analysis was used. Henry's law is often used to describe simple adsorption behavior at low molecular loading, or partial pressure, which is consistent with our physical picture of the single molecule, which interacts dynamically with individual adsorption sites, on the pore surface. For the temperature dependent data described here, larger values of  $\bar{P}$  were consistently reflected as a decrease in the slope of the leading edge of the polarization histogram. Therefore, as a reasonable first order approximation, an effective rate ( $k$ ) could be obtained for each histogram by fitting to an exponentially decaying function ( $y = a + be^{-kx}$ ). Here we have

assumed that a decrease in  $\bar{P}$  results directly from an increase in the rotational rate (a decrease in the rotational time constant  $\tau_r$ ), which is proportional to  $1/k$ . These  $k$  values are then equated to the Henry's law constant ( $K$ ), the temperature dependence of which can be described by the Van't Hoff equation:

$$\text{Equation 6.9} \quad \ln(K) = -\frac{\Delta H}{R} \left[ \frac{1}{T} \right] + \frac{\Delta S}{R}$$

A plot of  $\ln(K)$  versus  $1/(RT)$ , shown in Figure 6.18, demonstrates the expected linear relationship. Fitting the Van't Hoff equation to both the DiIC<sub>18</sub> on glass and mesoporous silica data yields values for the heats of adsorption ( $\Delta H$ ) of 8.7 and 25.8 kcal/mol, respectively.

The calculated heat of adsorption on glass (8.7 kcal/mole) is consistent with that reported for similar molecular systems<sup>132, 133</sup>, and is larger than expected for pure physisorption (~1-6 kcal/mole). This suggests that the formation of chemical bonds may be occurring, but with a reduced likelihood. Nonetheless, because induced rotational motion in the temperature range applied here remains unlikely, these bonds are sufficient to fix the adsorbed molecules on the surface.

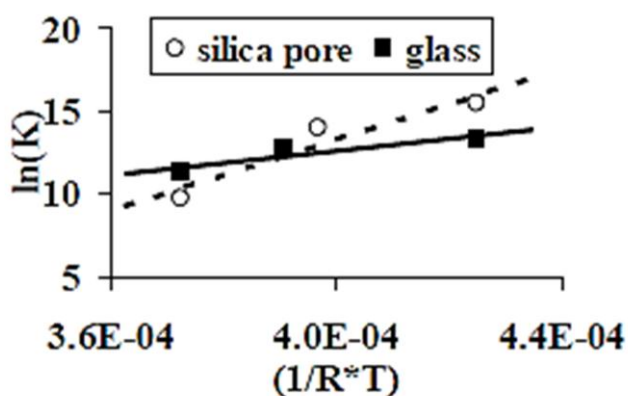


Figure 6.18 Henry's law fit to data. Shows that the heat of adsorption  $-\Delta H_0$  for the molecule on an infinitely large pore wall to be 8.7 kcal/mol and for the molecule in a 2.5 nm pore to be 25.8 kcal/mol.



The larger calculated value for the heat of adsorption (25.8 kcal/mol) in the mesopore suggests that chemisorption may be playing a greater role in the surface interactions. Although the cover slip glass surface adsorption site density is assumed analogous to the areal density found within a silica membrane pore, the irregularity of the geometric shape and high surface area of the pore itself, places adsorption sites at closer proximity to one another. The structural symmetry of DiIC<sub>18</sub>, and the delocalized charge along the molecular dipole make it possible for both ends of molecule to sample adsorption sites in the high surface area site density in the pore interior. As such, molecular binding energies larger than expected for a single chemisorption event are possible. At low temperatures, the dye molecules are randomly oriented and held fixed, due to strong surface interactions, exhibiting relatively low values of  $\bar{P}$ , consistent with the case of DiIC<sub>18</sub> deposited on glass. These interactions may include a combination of both physisorption and chemisorption. As the temperature is increased, the low energy interactions are overcome and the molecule begins to sample neighboring adsorption sites in the pore, which only slightly increases  $\bar{P}$ . Further increasing the temperature overcomes higher energy interactions dramatically, increasing rotational diffusion, and increasing the frequency with which adsorption sites are sampled. The molecule will continue to exhibit rotational motion until it encounters single or multiple neighboring sites where strong chemisorption overcomes the induced thermal motion and traps the molecule at the surface. The significant increase in  $\bar{P}$  at elevated temperatures suggests that this trapped state reflects some underlying degree of short-range order within the mesopore.

## 6.7. Conclusions

Surfactant templated sol-gel mesoporous silica membranes have received attention because of their narrow pore size distribution and ordering of the interconnected pores. Potential applications include ultrafiltration, biological separations, drug delivery, and separators in lithium-ion batteries. Despite advances in synthesis and characterization of these membranes, a

quantitative description of the membrane microstructure remains a challenge. Although current characterization methods are very effective in determining membrane performance, general pore size distribution, and defect concentration, they are unable to monitor individual molecular behavior within the membrane and quantitatively measure molecular interactions between the molecular species and pore network.

Single molecule imaging techniques enable optical measurements, which probe materials on nanometer length scales, through observation of individual molecules, without the influence of averaging. Using single molecule imaging spectroscopy, we can quantitatively characterize the interaction between the probe molecule and the interior of the pore surface within mesoporous silica membranes. The technique described here utilized DiIC<sub>18</sub> as the molecular probe in three environments; in a free solution, on glass cover slip, and in a mesoporous membrane. From these investigations, we have been able to demonstrate the sensitivity of single molecule techniques in this material system and, by comparison to model systems, quantify local binding energies within individual pores. We believe this is the first example of an application of single molecule methods to the determination of thermodynamic surface parameters in these novel mesoporous systems.

Currently, efforts have been devoted to the improvement of the mathematical model to include more thermodynamic and kinetic processes found within the system studied. These improvements are; to allow the model molecule to interrogate a pore size distribution available to the probe molecule, to investigate this membrane and others with probes having different chemical structures, and to study the effect of surface treatment has on the thermodynamic and kinetic interaction between the pore and probe molecule.

## **7. HIGH RESOLUTION SPACIAL MAPPING OF SURFACE FEATURES OF MESOPOROUS SILICA MEMBRANES VIA FLUORESCENT PHOTOACTIVATION LOCALIZATION MICROSCOPY**

### **7.1. Chapter Abstract**

Fluorescent Photoactivation Localization Microscopy (FPALM) was applied to inorganic mesoporous membranes to produce sub diffraction limited images (<20nm) for measuring surface heterogeneity. The molecular positions of fluorophores within amorphous mesoporous silica membranes were analyzed using 2-D radial surface distributions. These experiments demonstrated the ability to identify molecular clusters of caged fluorescein that suggested sub-micron defects were present (<15nm). Preliminary data spurred the construction of a new FPALM system to increase sample analysis throughput. During the construction and testing of the new system for mesoporous membrane characterization, a secondary characterization technique was discovered that has the potential to measure diffusional behavior below the diffraction limit directly. Below presents these findings and the evolution to a novel diffusional characterization method.

### **7.2. Introduction**

With the increasing demand for reducing energy consumption and independence of fossil fuels there is an increasing interest in efficient separation/purification processes. Porous materials are currently successfully utilized in many separation and purification processes, such as; reverse osmosis<sup>134</sup>, drug delivery, drug purification<sup>102, 135-138</sup> microfiltration, ultrafiltration, nanofiltration, and many others<sup>139</sup>. Porous membranes have the potential to replace energy intensive processes such as cryogenic distillation<sup>1</sup>. Currently there is a lack of understanding of the links between synthesis conditions, intrinsic properties, and the overall membrane performance. Research in these areas is critical for the advancement of these materials and promoting their application to these technologies.

Often sub-micron surface features of porous membranes are measured by scanning electron microscopy (SEM) and transmission electron microscopy (TEM)<sup>140, 141</sup>. Although these techniques have achieved resolution as low as 50 pm<sup>142</sup>, it very difficult and time consuming to image large areas of material. Often strict sample preparation must be performed, some materials cannot be imaged or break down due to the energy imparted by the electron beam. These systems also operate under vacuum and are unable to measure molecular interaction between the membrane and diffusing species. Fluorescent Photoactivation Localization Microscopy techniques, simultaneously developed by Eric Betzig<sup>8</sup> and Professor Michael Mason and Professor Sam Hess<sup>10</sup> in 2006 is a technique that utilize a photoactivatable fluorescent probe that has achieved resolutions below 25 nm<sup>9</sup> by selectively activating a small number of specially resolved molecules. The emitted photons are recorded in an image. Over time the activated molecules irreversibly photobleached. At that point, a new population of molecules can be activated and their positions can be recorded. The point-spread function of a point emission source is used to locate the center of the spatially resolved molecules in each image. By compiling the results of many images, a high-resolution image of the sample material can be generated.

FPALM can be used to measure intrinsic properties of porous membranes without the need for specialized equipment, which is cost prohibitive. This technique, coupled with those described above in chapter 6, allows for the measurement of molecular dynamics.

## 7.3. Experimental

### 7.3.1. Instrument

All fluorescence data were collected in a custom built inverted laser microscope (ILM) using an Inverted Olympus IX71 (Figure 7.1). Uniform far field Kohler illumination of the constructed sample and excitation of fluorescein molecules was accomplished by the output of a 473 nm 100 mW (maximum) solid-state diode laser (LaserGlow technologies). A calibrated circular continuously variable metallic neutral density (ND) filter (Thorlabs) was used to adjust excitation power as necessary. Photo activation was achieved by pulsing a 100 mW 405 nm laser for 1 to 5seconds. Great care was taken to ensure the focal spot of both the 405 and 473 laser was aligned within the field of view by use of an iris during alignment procedures.

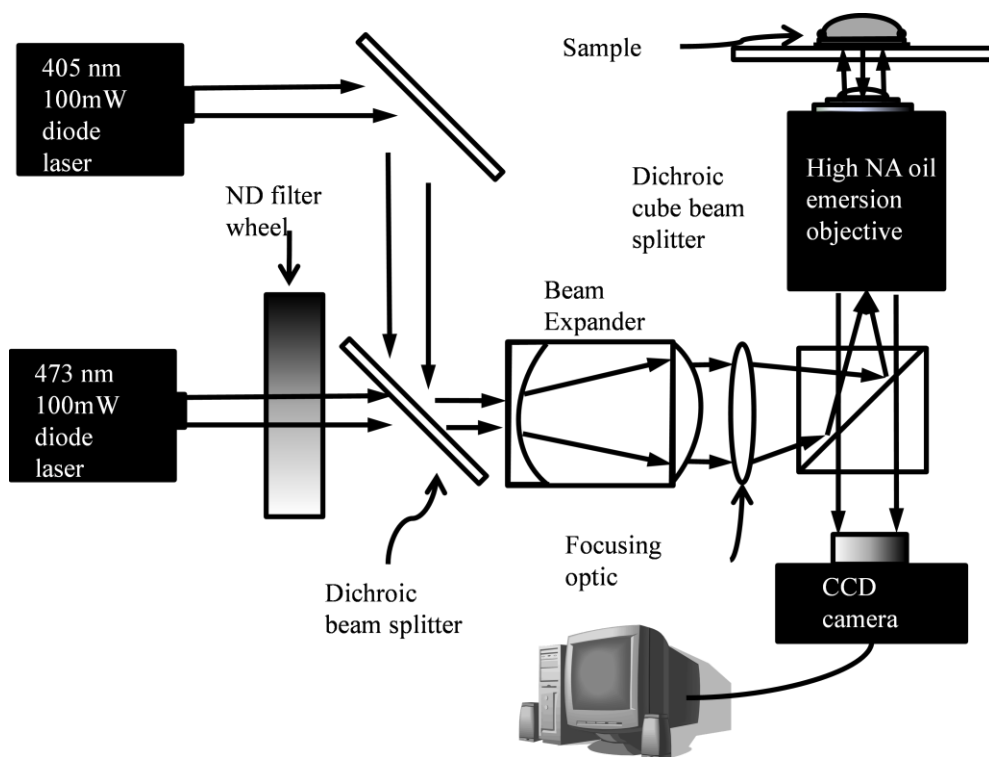


Figure 7.1 Diagram of the FPLAM microscope

The excitation and photoactivation incident beam passed through a Galilean beam expander constructed with a Ø 25.4mm, -25mm EFL plano concave from Newport optics and a Ø 25.4mm, f – 100mm plano convex lens from Thorlabs. The parallel expanded beam was directed to a focusing optic (Ø 25.4mm, 150mm EFL from Newport optics) with the focal length selected to match the distance to the back of a high NA oil emersion objective (Olympus PlanApo N 60X/1.42 oil) through a dichroic beam splitting cube (u-mf2 Olympus). To determine that the magnification of the sample area was appropriately matched to the CCD for FPALM, which has been reported to be less than  $\approx (100 \times 100) \mu\text{m}^2/\text{pixel}^9, 10$ , images of a NE18 (01B21213 5mm long cross hairs with 0.05mm divisions) reticle from Pyser SGI were taken. At this size, bright molecular features occupy 4 to 7 pixels. This number is crucial when discriminating molecular features from background noise. The pixel area was calculated by Equation 7.1;

$$\text{Equation 7.1} \quad L_p = \frac{N_{\text{div}}}{N_p} D_L$$

where  $L_p$  is the length of a pixel in the image in microns,  $N_{\text{div}}$  is the number of divisions of the sample image used,  $N_p$  is the number of pixels across the number of division in the sample image, and  $D_L$  is the length between the divisions; in this case it is equal to 0.05  $\mu\text{m}$ . For the system described here, the area per pixel is  $\approx 30 \times 30 \mu\text{m}^2$ .

The emission from the activated fluorescent was collected by High NA objective through the Cube Beam splitter by a CCD camera. The settings used for the camera were selected to maximize the dynamic range of the CCD and reduce the camera read noise (exposure time of 250 ms at a gain of 1 for 1000 images). As the number of activated fluorescent molecules dwindled due to irreversible photobleaching, the activation laser was pulsed for 1 to 5 seconds to increase the specially resolved population density.

### 7.3.2. Sample Preparation

Silica membranes were synthesized using tetraethylorthosilicate (TEOS) silica sol-gel templated with the non-ionic tri-block copolymer Pluronic P123 ( $\text{EO}_{20}\text{PO}_{70}\text{EO}_{20}$ , MW = 5800, BASF) resulting in 5nm pore diameter.<sup>114</sup> The silica sol-gel was then dip coated onto Fisher Premium cover slips (25mm x 25mm -1)<sup>143</sup> as discussed above in CHAPTER 6. An 18mm Buna-n O-ring was sealed onto the final as synthesized samples using Cytoseal™ 60 Mounting Media to create a well. The well was filled with 2ml of 1  $\mu\text{M}$  concentrations of concentrations of fluorescein bis-(5-carboxymethoxy-2-nitrobenzyl) ether, dipotassium salt (CMNB-caged fluorescein) (invitrogen f-7103, shown in Figure 7.2), in spectroscopic grade pure n-hexane. The sample were placed in a humid environment ( $\approx 80\%$  RH) and aged for 24hrs. The capillary forces within the membrane systems are such that hexane solution has been known to wet the membranes.<sup>114, 117</sup> This dye has previously been used as a probe of lateral diffusion in both model and cellular lipid membranes<sup>144-147</sup>. The samples were washed twice with pure n-hexane, and blown dry between each wash, to remove any excess dye from the surface of the samples. Finally, the samples were mounted on a stage of the FPALM microscope<sup>10</sup>.

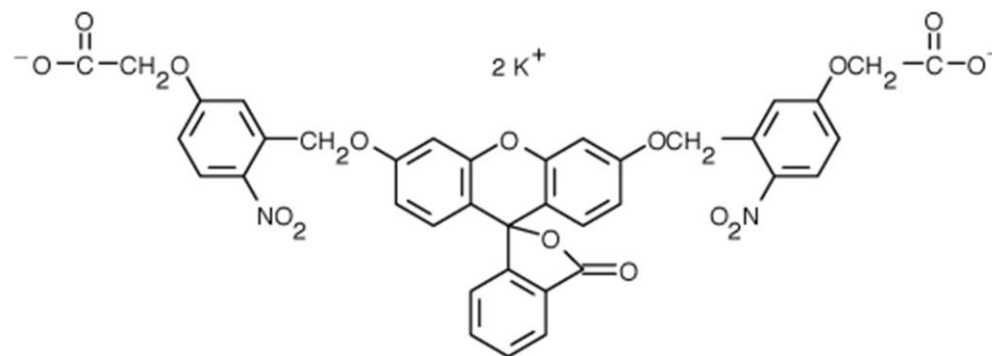


Figure 7.2 Molecular structure of fluorescein. bis-(5-carboxymethoxy-2-nitrobenzyl) ether, dipotassium salt

The doped membranes were placed into the confocal microscope and a wide field image was recorded on a CCD camera. After the wide field image was taken, the same area was pulsed with an activation laser to activate the fluorescent dye. After activation, the dye was excited with a second laser and the emission of the activated dyes was recorded in a video frame by frame via the CCD camera and computer (250 ms exposure 1000 frames). Once the sequential frame/images were recorded, a filtering software package was applied to localize the dyes 2D (xy) position, and remove any signal generated by electronic noise or aggregates recorded in each frame. All of the frames were compiled to generate a single image. The final compiled image was statically analyzed to elucidate any structural information about the sample, i.e. defect size, pore size, and pore density.

#### **7.4. Analysis**

Preliminary data recorded in a secondary lab show promise for spatially resolving surface features below the diffraction limit ( $< 200$  nm). An example image, generated by analysis is shown in Figure 7.3. After preliminary experiments demonstrated that FPALM techniques could be used to image mesoporous silica membranes, further experimentation was performed for analysis. The initial investigation used a surface radial distribution to measure differences of sample morphologies.



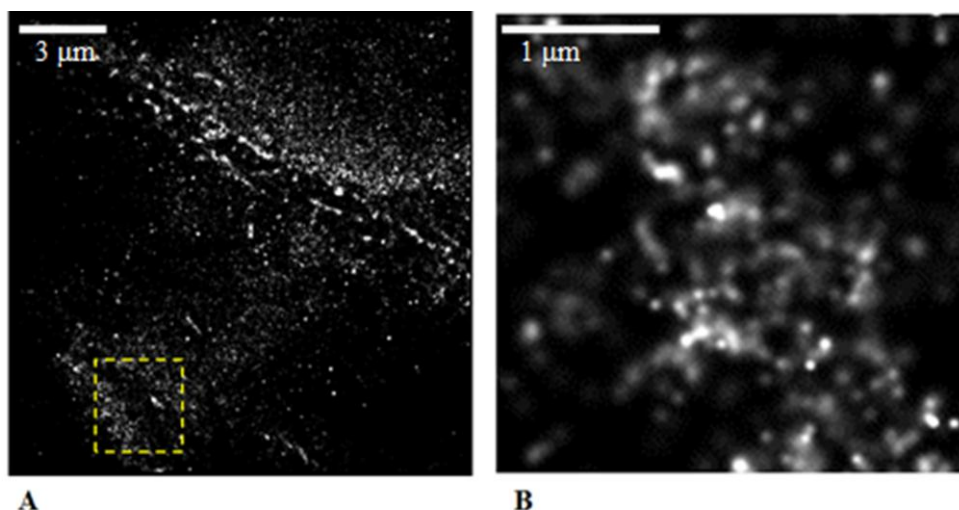


Figure 7.3 Sample FPALM images. A.) an example image of a 30 X 30  $\mu\text{m}$  area of mesoporous silica membrane. B). is 3 X 3  $\mu\text{m}$  area from image A. indicated by the dotted box.

Examples of the different morphologies investigated are shown in Figure 7.4. The figure shows two sample areas that contain a large fissure where Figure 7.4A is an area that has many visible micro fissures, and Figure 7.4 B appears to be free of micro fissures. Analysis of sample areas was performed by a 2-D radial distribution function described in Equation 7.2; where  $g(r)_i$  describes the molecular density of caged fluorescein molecules which vary as a function of distance from molecule  $i$ .  $\text{Hist}(n_j(r))$  is the histogram function that counts the number of molecules bound by a ring with an inner radius  $r$  and an outer radius of  $r + dr$  around molecule  $i$ . The results are normalized by the total number of molecules contained within the shell, described by radius  $r$  thickness  $dr$  and molecular surface density,  $\rho$ .

$$\text{Equation 7.2} \quad g(r)_i = \frac{\text{Hist}(n_j(r))}{2\pi r dr \rho}$$

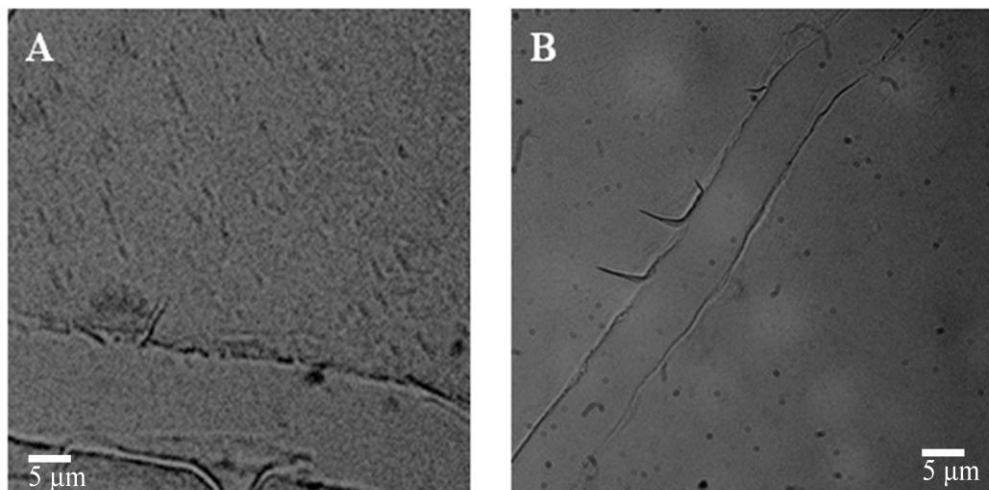


Figure 7.4 Shows two surface morphologies of mesoporous silica thin films. A) Is an area with many micro fissures, where image B.) appears relatively defect free.

The results from the radial distribution function shown, in Figure 7.5, show drastic differences between the two samples. In the sample shown in Figure 7.4 B, the radial distribution shows a small peak at  $\approx 60$  nm followed by a very homogeneous distribution. While the sample depicted in Figure 7.4 A demonstrates a vastly different distribution. In the distribution for this sample, the initial peak occurs at  $\approx 15$ nm followed by a series of decaying peaks. It is hypothesized that this behavior is due to the presence of micro fissures, seen in Figure 7.4 A.

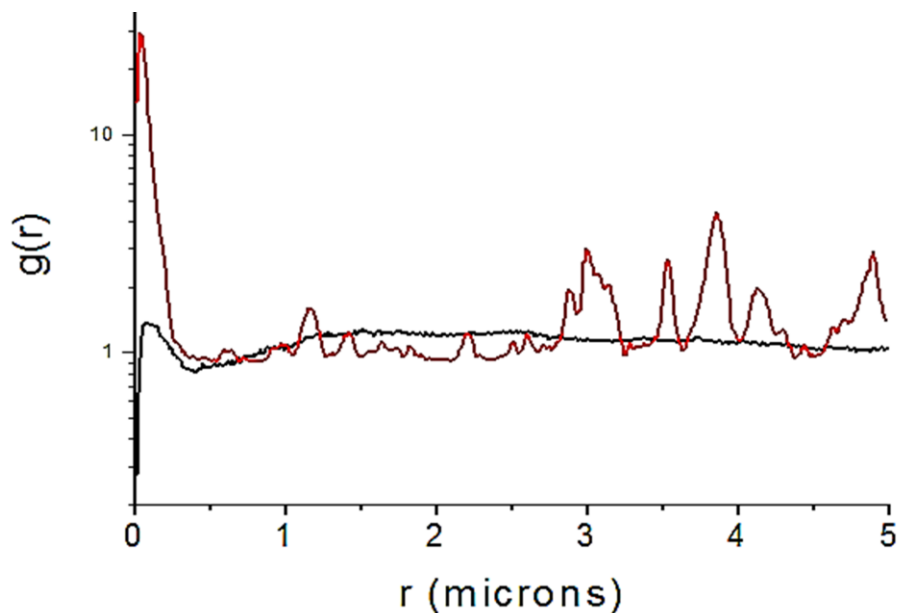


Figure 7.5 The resulting plot for the radial distribution analysis for two samples. The results for Figure 7.4 A is shown in red and the results for Figure 7.4 B is in black

It was determined that a larger data set was needed to validate this hypothesis. Due to the high demand for the FPALM system, scheduling experimental time on the existing system was not feasible. Therefore, an attempt was made to construct a new FPALM system dedicated to this project within Jenness Hall. A system analogous to that shown in Figure 7.1 was duly constructed and aligned. New samples were constructed by the procedure described above and were used to test the system and to verify its operation. Unfortunately, the new FPALM system did not respond as expected.

To simply the system for trouble shooting, a non-photoactivatable fluorescein was used in conjunction with an analogous sample membrane. The analogous membrane chosen was Whatman Anodisc with average pore size of 20 nm. The effect of photoactivation was represented by drop casting 200  $\mu\text{L}$  of nano molar concentrations of fluorescein onto the top side of a Whatman anodiscs, simultaneously the CCD camera was started to record sequential images

(200 ms exposures, 200 ms delays). The sequential images were post processed using Image-J<sup>148</sup> for troubleshooting parameters, i.e. number of saturated pixels average intensity per frame, etc.

Each frame's mean intensity for a sequential experimental run was plotted vs. frame number to monitor and determine potential errors. It was during the analysis that an unusual and unexpected result was observed. The expected result was a direct expression of photobleaching. Photobleaching occurs when a fluorophore loses its ability to fluoresce due to a photochemically induced reaction<sup>149, 150</sup>. This phenomenon is generally described using a stretched exponential decay shown in Equation 7.3.

$$\text{Equation 7.3} \quad I(t) = I_0 \Phi_{\text{ext}} C_i \left( A_0 \exp \left[ - \left\{ \frac{t}{\tau} \right\}^\beta \right] + y_0 \right)$$

Here,  $I(t)$ , the emission intensity observed at time  $t$ , which is the product of excitation energy,  $I_0$ , the collection efficiency,  $\Phi_{\text{ext}}$ , and the concentration of the fluorescent species,  $C_i$ .  $A_0$  is the molecular quantum efficiency,  $\tau$  is the lifetime,  $\beta$  is a fitting parameter for a stretched exponential (ideally 1), and  $y_0$  is the background fluorescence of the system. The observed results of photobleaching are shown in Figure 7.6.

The observed results for the porous discs used during the trouble shooting process for the new FPALM set up is shown in Figure 7.7. The significant and notable differences are the slower increase in fluorescent intensity in the beginning and the much slower rate of decay at long times.

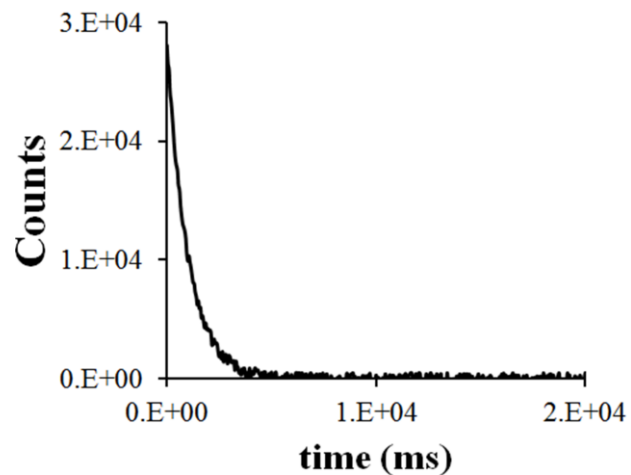


Figure 7.6 Sample photobleaching response of a fluorescent molecule. 100  $\mu$ l drop with a fluorescein concentration of 200 nM onto a coverslip.

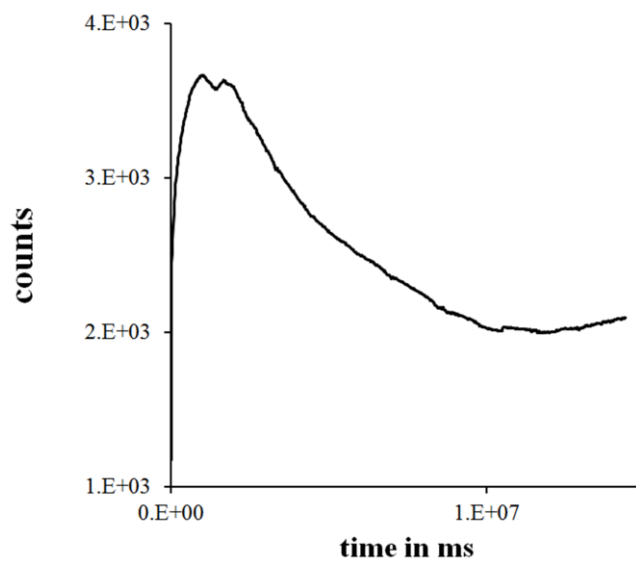


Figure 7.7 Shows the observed bleaching phenomenon. A 100  $\mu$ l drop of 200 nM fluorescein onto a 20 nm porous Whatman Anodisc.

## 7.5. Conclusion

Mesoporous membranes were successfully imaged at high resolution using FPLAM and analysis of the recorded molecular positions using a radial distribution function, which was able to identify significant differences of molecular positions of fluorescent molecules on mesoporous membranes. It has been hypothesized that these differences are due to the presence or absence of intrinsic defects, i.e. micro fissures. It was determined that a large sample set was needed to confirm this hypothesis. Standard photobleaching studies were performed to troubleshoot and verify that the newly constructed system was functioning properly. When comparing the photobleaching response of fluorescent molecules drop onto a blank slide glass and onto a model porous membrane another unexpected phenomenon was observed. The model membrane studies showed a lag time before maximum fluorescent intensity was reached, what is perceived to be a longer molecular lifetime and an overall reduction in fluorescent intensity. While at long observation times, a much slow rate of photobleaching was expressed by the model membrane samples. It is believed that these observations are related to a hold up of fluorescent molecules within the model membrane. These observations warranted further studies.

## **8. DEVELOPMENT OF A TIME-RESOLVED FLUORESCENCE IMAGING METHOD TO MEASURE CONCENTRATION PROFILES THROUGH POROUS MEMBRANES**

### **8.1. Chapter Abstract**

A simple fluorescence imaging method for measuring the time-resolved concentration profile of a fluorescent molecule diffusing through an anodic alumina membrane, with a pore diameter of 20 nm, is presented. Several concentration breakthrough curves were obtained to determine the system's dependence upon excitation power and concentration loading. The breakthrough curves were used to validate the stability and reproducibility of this new technique. Once the measurement system tested, the molecular diffusivity of fluorescein was extracted by analysis of the concentration breakthrough curves using a quasi-steady state model. The experimentally determined diffusivity was three orders of magnitude lower than reported bulk values. Due to the relative simplicity and ease of use, it is anticipated that this method can be applied to provide fundamental information for bio-molecular separations applications, membrane quality control studies, and membrane performance characterization. Several features of this technique may have industrial significance. The system generates the concentration breakthrough curves from the mean values of sequential images taken of the permeate side of the membrane directly. This approach allows one to measure specific responses caused by defects and heterogeneities in the membrane. In addition, the high sensitivity of this method at inter-cellular volumes may further broaden its future application to include the study of drug delivery and controlled cell growth.

### **8.2. Introduction**

The time-dependent concentration measurement of a molecule diffusing through a porous medium provides fundamental information for the design of separation and transport systems/devices. In the case of solute diffusion, practical applications include drug delivery<sup>151</sup>,<sup>152</sup>, cell growth via controlled nutrient delivery<sup>153</sup>, and molecular separations<sup>154-156</sup>. Until recently,

fluorescent time-dependent measurements have been studied by placing a pill-like vessel with an anodic alumina membrane surface containing a specified dye concentration into a larger vat. Periodically, liquid samples were withdrawn from the large vat and spectroscopic methods were used to determine the increase in concentration of the dye molecule<sup>136, 137</sup>. Other studies have used these methods, or a sweep flow measurement, coupled with the Hagen – Poiseuille flow model to ascertain the diffusivities of solute molecules<sup>157, 158</sup> and measure important membrane parameters<sup>157</sup> (i.e. pore density and mean pore radius). The time-dependent concentration measurement of a molecule diffusing through a porous medium provides fundamental information for the design of separation and transport systems/devices. In the case of solute diffusion, practical applications include drug delivery<sup>151, 152</sup>, cell growth via controlled nutrient delivery<sup>153</sup>, and molecular separations<sup>154-156</sup>. Although these methods have proved to be effective at measuring the bulk membrane/solution interactions and estimating drug delivery rates<sup>136, 137, 157, 158</sup>, they are difficult and labor intensive and not well suited to the acquisition of high resolution data at millisecond time scales. These methods also lack the sensitivity to measure subtle changes in diffusion dynamics such as physical-chemical surface interactions. These techniques employ concentration measurement at a significant distance from the permeate side of the membrane and are unable to measure the dynamics that may occur at the immediate outlet of the pores that may be crucial for biological systems, i.e. defects in the membrane surface.

Recently, optical methods, such as Fluorescence Recovery After Photobleaching (FRAP), have been successfully applied to measure the diffusivity in a variety of material systems including biofilms, fibers and membranes.<sup>159-162</sup> In FRAP, the fluorophore is photobleached in a known area and the time-dependent migration of non-bleached fluorophores is measured<sup>162</sup>. Unfortunately, with this technique, it is difficult to ensure concentration-driven diffusion and adsorption dynamics are observed because the photobleached molecules remain within the volume of interest. More recently, single-molecule imaging techniques have been applied to study diffusive transport through membranes, providing a highly-sensitive, spatially-correlated



picture of molecular movement through porous media<sup>163</sup>. Owing to the low signal levels, specific and often very costly instrumentation is required. Furthermore, strict sample preparations are mandated, and significant limitations on sample type and geometry exist. One challenge that needs to be met to further the understanding of the cause for observed effective diffusivities in porous medium is in the area of characterization. There are very few techniques capable of measuring molecular dynamics within a porous matrix that are sensitive enough to monitor changes in a diffusional response and to assign those changes to specific properties, i.e. adsorption, electrostatic responses, hydrodynamic hindrance, and defects.

A unique and relatively simple fluorescence imaging method was developed and tested to measure molecular breakthrough curves of an inorganic membrane at the exit surface. This method avoids many of the limitations of single-molecule methods, but still provides femto-molar sensitivities at the inter-cellular volumetric scale. Commercially available anodic alumina porous discs (Anodisc<sup>TM</sup>) were used as well defined model systems to ascertain the sensitivity for measuring the effects of diffusing fluorescein molecules and the dependence on environmental changes, i.e. concentration or excitation power. These membranes are characterized by a high pore density ( $10^9$  pores/m<sup>2</sup>), uniform pore size (20nm), and straight channel pores (tortuosity,  $\tau = 1$ ). In this study, we used anodic alumina membranes with a total diameter of 13 mm, mean pore diameter of 20 nm, thickness of 60  $\mu$ m, and porosity of 25-50%. Although not addressed here, the system developed can easily be modified for industrial applications, namely quality control of inorganic or polymer membrane. The power of this method comes from the direct analysis of the sequential images taken of the membrane's permeate face. The method employed and discussed here only images a relatively small area ( $\approx 100$  microns by  $\approx 100$  microns), but in an industrial application, the imaged area is only limited by the size of the CCD array and the computer processing power. This technique allows the simultaneous measurement of a membrane's bulk performance and its separate diffusional components (i.e. defect areas and defect free areas) to determine their individual significance. Figure 8.1 shows a schematic representation of how this

type of system could be used in an industrial quality control application. By breaking down a whole imaged area into parts that focus on defects and comparing the diffusion breakthrough curve of that area to the whole image or an area without defects, one would be able to quantify the amount bypass flow for given membrane. This approach allows for inline and real-time identification of large defect free areas to produce a high quality product.

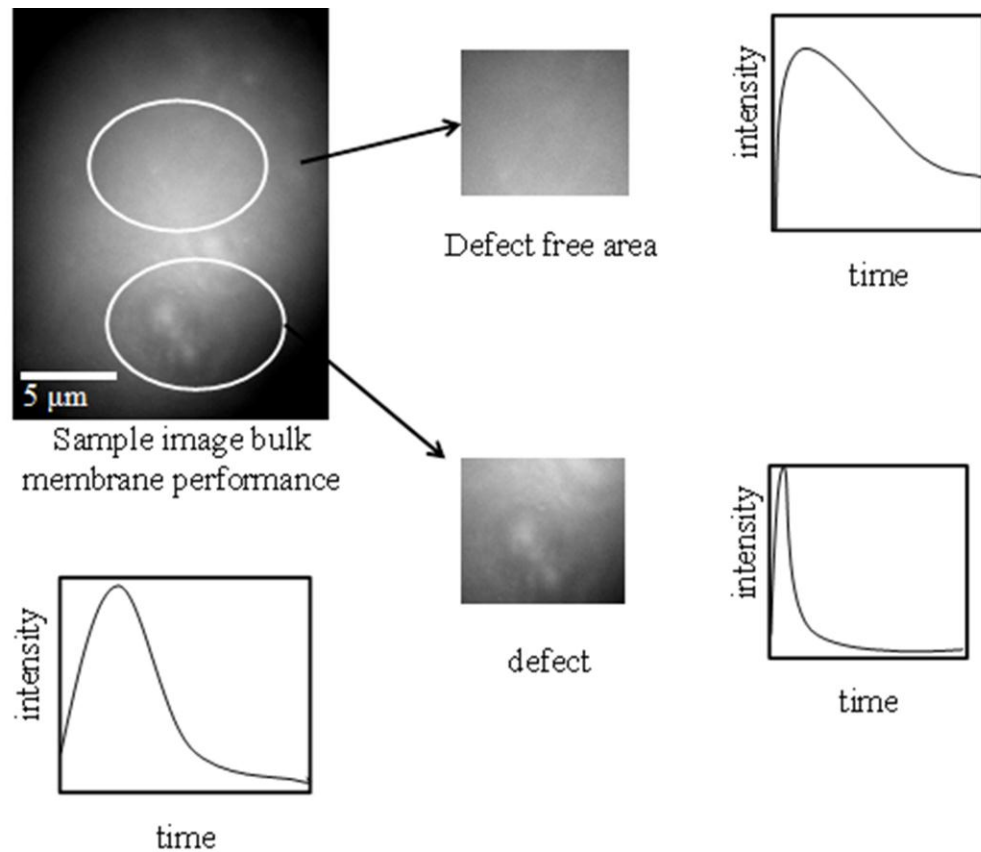


Figure 8.1 A suggested analysis and breakdown of an image for quality control.

## 8.3. Experimental

### 8.3.1. Instrument

All fluorescence data were collected on a custom built inverted laser microscope (ILM) using an Inverted Olympus IX71 (Figure 8.2). Uniform far field Kohler illumination of the constructed sample and excitation of fluorescein molecules was accomplished by the output of a 473 nm 100 mW (maximum) solid-state diode laser (LaserGlow technologies). A calibrated circular continuously variable metallic neutral density (ND) filter (Thorlabs) was used to adjust the excitation power as necessary.

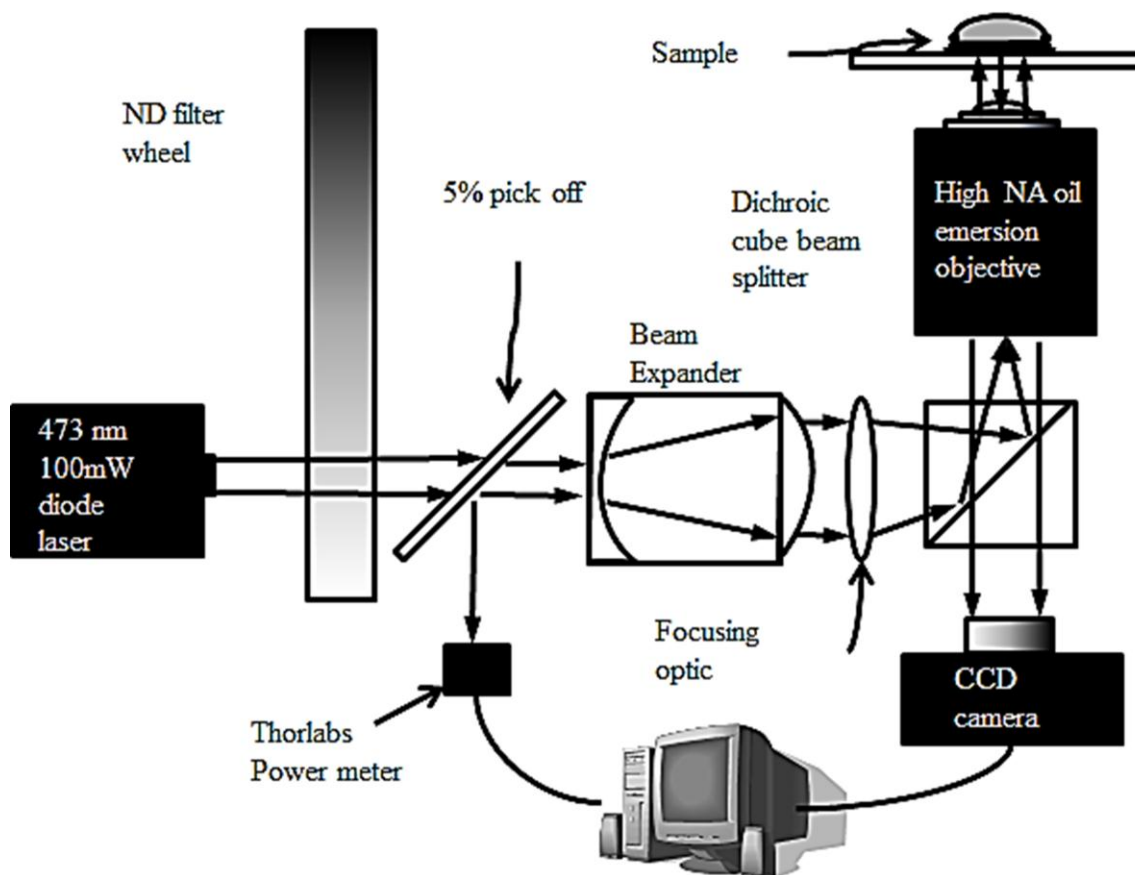


Figure 8.2 Diagram of the inverted wide field fluorescent microscope

To identify any fluctuations in the emission signal correctly, the excitation power must be known for each sample frame recorded. This was performed by sampling the excitation power using a 5 % beam splitter after the ND wheel. The beam-splitter was used to direct a continuous beam sample to a power meter, (Thorlabs PM100) continuously monitoring the excitation beam at a rate of 20 samples per second. The signal recorded by the power meter was corrected to represent the energy of the beam passing through the sample and was stored on the computer for later processing by a custom Labview 8.5 NI software package. The remainder of the excitation incident beam passed through a Galilean beam expander; constructed with a  $\text{\O} 25.4\text{mm}$ ,  $-25\text{mm}$  EFL plano concave from Newport optics and a  $\text{\O} 25.4\text{mm}$ ,  $f = 100\text{mm}$  plano convex lens from Thorlabs. The parallel expanded beam was directed to a focusing optic ( $\text{\O} 25.4\text{mm}$ ,  $150\text{mm}$  EFL from Newport optics) with the focal length to match the distance to the back of a high NA oil immersion objective (Olympus PlanApo N 60X/1.42 oil) through a dichroic beam splitting cube (u-mf2 Olympus). As the excited fluorescein molecules diffused into the focal volume, their emission was collected by High NA objective through the Cube Beam splitter by a Spot RT3 CCD camera. The settings used for the camera chosen maximized the dynamic range of the CCD and reduce the camera read noise (2 X 2 binning and a gain of 2).

### **8.3.2. Software Written**

Although the two programs written for this project are basic computer hardware interfacing routines, they were crucial for data analysis, trouble shooting, and useful for quickly determining and eliminating, poor data sets. The first software written controlled the power meter's settings and recorded the instantaneous laser powers during each run via the RS232 port. They enabled calculation of a sliding average of the laser excitation power, originally intended as a manner to remove any day-to-day fluctuations in the excitation power used in the different runs. This measurement of power fluctuations proved important for quickly determining the success of experimental runs data records prior to analysis. After numerous inconsistencies between data

sets recorded under the same experimental conditions, analysis of the power meter's records suggested the cause of the inconsistency was instability of the excitation source. All data sets with power fluctuations greater than 5% of the average power within the first 80 minutes were found to be problematic for numerical analysis. Further investigation determined that the root cause of the fluctuations was instability of the building electrical supply. Unfortunately, the solution to this problem is cost prohibitive. However, identifying the root cause of the inconsistent results allows for the utilization of a statistical solution to remove unexpected aberrations.

The fluctuations could be accounted for and removed from the image files by modifying the program listed above to record the timestamps of the power readings and creating a second algorithm to normalize the results of the imaging by the instantaneous excitation power records. By knowing the start time of the image records, their exposure time, and delay time each file was correlated to the power meter readings with the coinciding time stamps. The images were divided by the average power for its time window. In this manner, the different experimental runs could be compared and analyzed simultaneously. It is important to note that although this technique had reasonable success in removing emission intensity changes due to excitation fluctuations, it is not without its limitations. The image files were recording information representative of molecules diffusing into the interrogated volume and the removal of said molecules via bleaching simultaneously, and that these phenomena are dependent on excitation energy, time, and each other. The challenge arises when the excitation source's fluctuations increase to levels at which the fluorescent bleaching dynamics are significantly affected (variance  $\approx 5 - 8\%$ ). With high levels of prolonged fluctuations of excitation energy, the assumption that photobleaching dependence is dominated by excitation power begins to fail and one must account for the time of these fluctuations. Since the data analysis of simultaneously diffusing and bleaching molecules is not trivial, the addition of an unpredictable time-dependent excitation power makes the data impractical for modeling and analysis. Once the understanding of these systems is improved, the

fluctuations in excitation power may be beneficial. Until that time, these data sets are removed from the analysis. To improve successful data collection, an electrical power source stabilization unit needs to be added to the developed system. Once that was achieved, further studies monitoring these fluctuations and careful model corrections may prove useful in this endeavor.

### 8.3.3. Photobleaching Nanopure Water

All solutions and washes of materials were performed using photobleached nanopure water. 100 ml aliquots of nanopure water were exposed to a high intensity broadband source for 30 min to eliminate any contaminants that may increase the background fluorescent signal.

### 8.3.4. Sample Preparation

Size 012 viton O-rings (McMaster Carr) were sealed to Anopore inorganic membranes (13mm diameter, 60  $\mu\text{m}$  thick Whatman Anodiscs with a 0.02 $\mu\text{m}$  pore size, with  $\approx$ 30 to 35% porosity and a tortuosity of 1 as reported by Whatman) using Cytoseal-60 mounting medium to

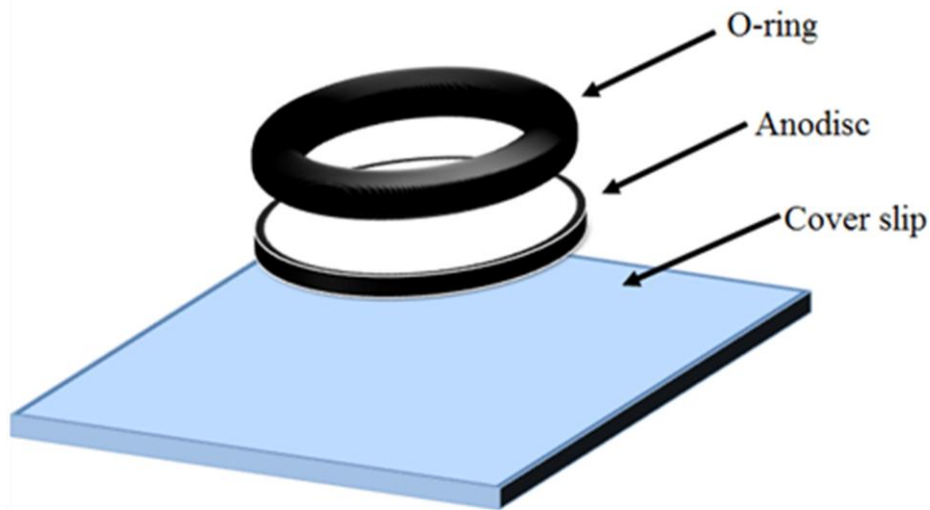


Figure 8.3 Shows the of components needed for the creation of a sample to be studied

create a well sample (Figure 8.3).

The samples were soaked in bleached nanopure water for 24 hrs to ensure that the pores of the Anodiscs were completely hydrated. The capillary forces within the nominal pore size of the Anodisc are such that water has been known to wet the anodiscs<sup>117, 164</sup>. After the aging process, each sample was removed from the bleached nanopure water. While the Anodisc was wet, it was sealed to a Esco Brand #0 optically clear silicate glass coverslip using Cytoseal-60 mounting medium (Figure 8.3). Care was taken to remove any excess water contained in the top well of the wetted sample, while leaving enough solvent to fill the void volume on the permeant side. This geometry and sample preparation allow solute diffusion driven by a concentration gradient from a bulk solution into a vessel of approximately 150nL (transport area  $\approx 1 \text{ cm}^2$ , vessel thickness  $\approx 1.5 \text{ }\mu\text{m}$ ). Emission from the fluorescein molecules diffusing through the membrane into the void volume was collected by CCD camera as described above in section 8.3.1. The settings used for the camera were chosen to maximize the dynamic range of the CCD and reduce the camera read noise (2 X 2 binning and a gain of 2). Typical Images were recorded with a 200 ms exposure and a 15.8-second delay between each image. Excitation was performed by running the laser at full power (100 mW). The neutral density filter was adjusted to produce a signal of 800  $\mu\text{W}$  at the 5% pick off mirror shown in Figure 8.2. This setting has been measured to produce an excitation power of 7 mW at the sample. The Camera and power meter were run simultaneously and continuously for 160 minutes (600 images).

### **8.3.5. Method**

Once the sample was placed into the microscope, an optimum site free of fluorescent defects was located in the Anodisc focal plane by selecting a site whose background signal was uniform and coincided with the excitation beam intensity at the focal plane. Figure 8.4 A. Shows an example of an area with defects and non-uniform illumination, where Figure 8.4 B. is an example of an ideal location for study.

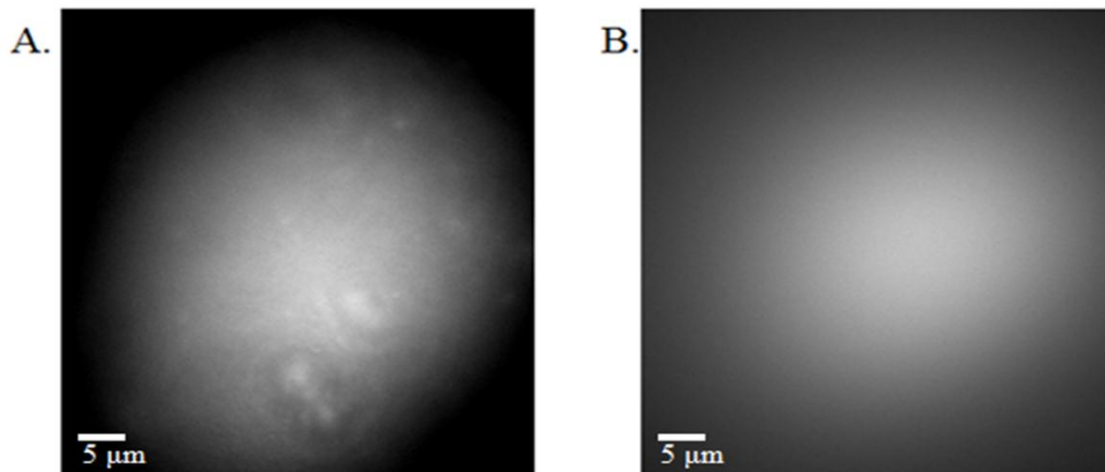


Figure 8.4 Show examples of defect areas. A.) In addition, non-defect areas are show in picture B.)

Using the focal adjustment the Z location of the focal plane of the cover slip ( $Z_g$ ), bottom of the Anodisc ( $Z_b$ ) and the top of the Anodisc ( $Z_t$ ) was recorded. This information was used to locate a focal plane within the void volume and to determine the depth of the void volume ( $\delta_v$ ) by the relationship shown in Equation 8.1, where  $\delta_a$  is the thickness of the Anodisc ( $\approx 60 \mu\text{m}$ ).

$$\text{Equation 8.1} \quad \delta_v = \left( \frac{Z_b - Z_g}{Z_t - Z_b} \right) \delta_A$$

The camera and the power meter were started and were allowed to run as described above. 200  $\mu\text{L}$  aliquots of fluorescein at concentrations of 170 or 340 nM were added to the top side of the prepared sample. A cover was placed over the top of the sample shown in Figure 8.5; this was done to limit any response of the fluorescent signal to ambient air currents and to reduce drying.



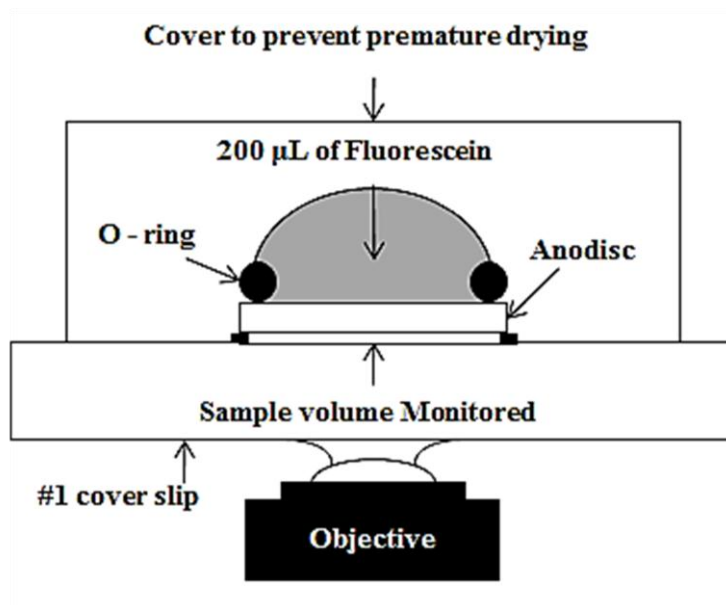


Figure 8.5 Depiction of the fabricated sample system. Showing the volume monitored for diffusivity measurements.

Four runs at each concentration and excitation power were recorded. After each run, each frame was analyzed independently utilizing the image-J<sup>148</sup> software package to find the mean intensity for each recorded image in the sample. The mean values of each frame were corrected for fluctuations in the emission signal generated by the excitation signal by dividing the average value of the power readings by time of each frames exposure time. Due to the high sensitivity of the system, the void volume of each fabricated sample, calculated by Equation 8.1, was used to normalize the data set for its corresponding experimental run. This was done to remove the emission signal's response to the focal point of the excitation source within the z plane.

The four separate experimental curves recorded for each for each concentration and excitation power were averaged together to eliminate aberrations due to fluorescent impurities of the Anodiscs and to reduce any effect from day to day fluctuations of the ambient condition. All experimental data sets were corrected for power fluctuation by using Equation 8.2.

Equation 8.2 
$$I(t)_{\text{corr}} = \frac{I(t)}{\langle I_0 \rangle} I_0^*$$

Where  $I(t)_{\text{corr}}$  is the corrected emission intensity,  $I(t)$  is the recorded raw emission intensity,  $\langle I_0 \rangle$  is the average excitation intensity for the run corresponding data set, and  $I_0^*$  is the average excitation energy for all duplicate data sets. After correcting for fluctuations due to the excitation source, the emission intensities of each sample type were plotted versus time. Figure 8.5 shows a diagram of the completed sample set-up used to collect breakthrough data for fluorescein through the alumina membranes. This geometry allowed for concentration-driven solution diffusion from a large bulk volume into a vessel of approximately 150 nL.

The Fluorescence signal was recorded using an inverted laser microscope (Olympus IX71) and a CCD camera. Images were recorded at 4 different excitation powers ( $\approx 0.4$ ,  $\approx 0.8$ ,  $\approx 1.9$ , and  $\approx 3.0$  mW) and two different fluorescein concentrations (170nM and 340nM) for exposures of 200ms with a 15.3 second delay between each image acquisition. Measurements at different incident power levels eliminated the effects of instrumentation on the breakthrough curves. The camera and power meter were run simultaneously and continuously for 155 minutes (600 images), until steady state, intensity was reached, indicating no further change in fluorescein concentration. The raw collected data is shown in Figure 8.6 for the four different excitation powers and includes photobleaching effects.

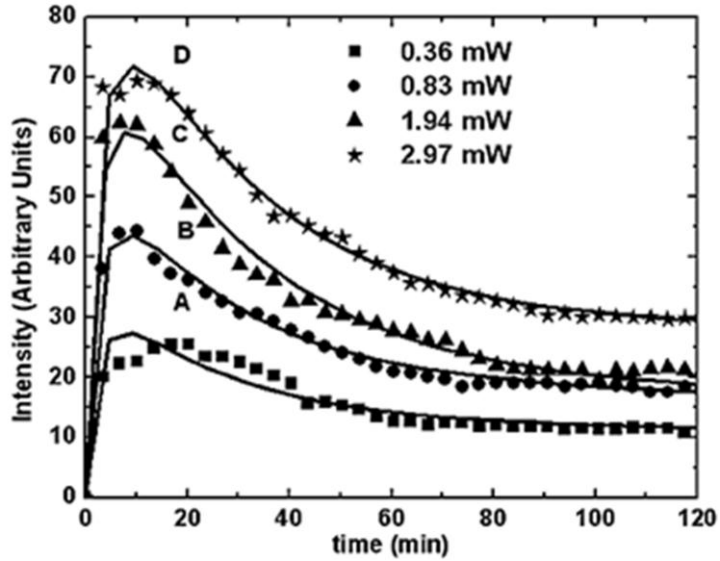


Figure 8.6 The mean intensity of each versus time in minutes for 340nM of fluorescein. Symbols represent raw data points for, A)  $\approx 0.36$  mW, B)  $\approx 0.83$  mW, C)  $\approx 1.94$  mW, and D)  $\approx 2.97$  mW, the results of the simultaneous fit of the model are depicted as solid lines. To simplify the figure every tenth point is shown for the first 120min of the raw data.

#### 8.4. Analysis

In the experimental set-up in Figure 8.5, it was assumed that the time required for diffusion through the membrane is short compared with the time required for the membrane to reach adsorption equilibrium. Therefore, a quasi-steady state system can be applied to the mass balance across the membrane. For a membrane with a porosity  $\epsilon$  and cross-sectional area  $A$ , the balance is shown in Equation 8.3,

$$\text{Equation 8.3} \quad V_i \frac{dC_i}{dt} = J\epsilon A$$

where  $V_i$  is the collection volume at the exit of the membrane,  $C_i$  is the concentration and  $J$  is the flux leaving the membrane. The flux in the membrane can be expressed by Fick's first law shown in Equation 8.4,

$$\text{Equation 8.4} \quad J = -\frac{D}{\tau_r} \frac{dc}{dx}$$

where  $D$  is the diffusivity and  $\tau_r$  the tortuosity of the pore network. Assuming that loading concentration ( $C_0$ ) remains constant and that both the concentration and the lower membrane surface ( $C_i$ ) is well mixed, the following boundary conditions in Equation 8.5 were applied:

$$\begin{aligned} \text{Equation 8.5} \quad & @ \ x = 0, \ c = c_0, \ \text{for all } t \\ & @ \ x = l, \ C = C_i, \ \text{at } t = 0 \\ & @ \ x = l, \ C_i \rightarrow C_0 \ \text{as } t \rightarrow \infty \end{aligned}$$

For a constant Diffusivity, integrating the flux over the membrane thickness,  $l$  and the bulk concentration,  $C_0$  to  $C_i$  and solving Equation 8.3, yields a model for transport through the membrane, Equation 8.6:

$$\text{Equation 8.6} \quad \frac{C_i(t)}{C_0} = 1 - \exp\left[-\left(\frac{\varepsilon DA}{\tau_r V_i l}\right)t\right]$$

In addition to transport, photobleaching of the molecules must be accounted for as described by Equation 8.7.

$$\text{Equation 8.7} \quad I(t) = I_0 \Phi_{\text{ext}} C_i \left( A_0 \exp\left[-\left\{\frac{t}{\tau}\right\}^\beta\right] + y_0 \right)$$

Here,  $I(t)$ , the emission intensity observed at time  $t$ , which is the product of excitation energy,  $I_0$ , the collection efficiency,  $\Phi_{\text{ext}}$ , and the concentration of the fluorescent species,  $C_i$ .  $A_0$  is the molecular quantum efficiency,  $\tau$  is the lifetime,  $\beta$  is a fitting parameter for a stretched exponential (ideally 1), and  $y_0$  is the background fluorescence of the system. The time-dependent extent of bleaching,  $EB(t)$ , in our continuous system is then shown in Equation 8.8.

$$\text{Equation 8.8} \quad EB(t) = I(t)/I(0)$$

The final expression for transport as measured by the fluorescence signal, including photobleaching effects is given in Equation 8.9.

$$\text{Equation 8.9} \quad I(t) = I_0 \Phi_{\text{ext}} C_i(t) EB(t)$$

The raw data shown in Figure 8.6 were fitted to the model above. The defined parameters were  $I_0$ , the excitation energy used to produce the raw data and  $C_0$ , the loading concentration of fluorescein. The shared, undefined parameters between all experiments were  $\Phi_{\text{ext}}$ , the excitation efficiency of the system,  $D$ , the effective diffusion constant,  $\tau$ , and  $\beta$ . The parameters that were independently fitted for each data set were  $\varepsilon$ , the porosity of the alumina membranes (bounded by 30% to 35% as reported by Whatman),  $A$ , the area accessible to the fluorescent molecules,  $\ell$ , the thickness of the disc (reported by Whatman),  $V_i$ , the volume between the alumina membrane and glass slide shown in Figure 8.5. Where  $y_0$  and  $A_0$ , is the mathematical representations of the background fluorescent signal described in Equation 8.7. Figure 8.7 shows the breakthrough curve for the alumina membrane, determined from the averaging of the data shown in Figure 8.6, normalized by excitation energy for each initial concentration of fluorescein. The experimental breakthrough curve is similar to data obtained from molecules diffusing from porous media.

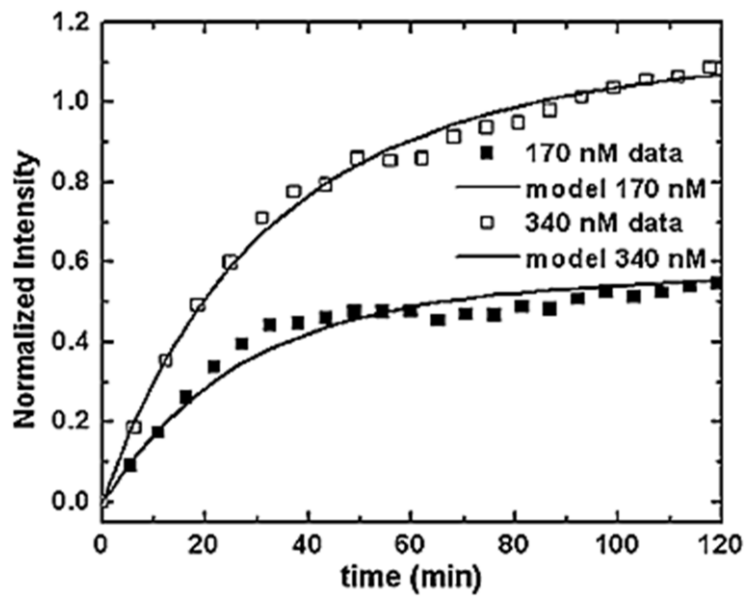


Figure 8.7 The observed raw averaged diffusion breakthrough curves. Fluorescein concentrations of 170 nM and 340 nM, normalized by excitation energy shown as symbols; and the modeled diffusion breakthrough shown as solid lines. To simplify the figure every tenth point is shown for the first 120min of the raw data.

## 8.5. Discussion

The diffusivity of fluorescein, determined from our data and model in anodic alumina membranes, was  $(7.0 \pm 0.1) \times 10^{-10} \text{ cm}^2 \text{ s}^{-1}$ ; considerably slower than the bulk diffusivity of fluorescein measured in pure water ( $5.6 \times 10^{-6} \text{ cm}^2 \text{ s}^{-1}$ )<sup>159</sup>. Our results compare favorably to those of Jiang, et al.<sup>152</sup>; who measured diffusivities of caffeine, methyl orange and malachite green oxalate through 40 nm porous anodic alumina membranes. In addition, our results compared to the diffusivity of fluorescein measured by FRAP in collagen fibrils with an estimated interstices of 1.6 nm ( $D = 1 \times 10^{-10} \text{ cm}^2 \text{ s}^{-1}$ )<sup>159</sup> nylon 66 ( $D = 6.9 \times 10^{-11} \text{ cm}^2 \text{ s}^{-1}$ )<sup>165</sup> and biofilms ( $D = 7.7 \times 10^{-8} \text{ cm}^2 \text{ s}^{-1}$ )<sup>161</sup>. Here, binding of the fluorescein to the fiber surface also contributed to the reduced diffusivity. In addition, Fowlkes, et al.<sup>160</sup> measured a diffusivity of fluorescein isothiocyanate through a carbon nanofiber membrane using FRAP ( $D = 7.5 \times 10^{-7} \text{ cm}^2 \text{ s}^{-1}$ ). The decrease in diffusivity of fluorescein in our alumina membranes could result from either size effects or

surface effects. The hydrodynamic radius of fluorescein has been estimated at 0.4 nm<sup>159</sup>, smaller than the pore diameter of 20 nm, yet still close enough to the pore diameter to have significant interaction with the pore walls. According to Brunelle, J. P.<sup>166</sup>, the isoelectric point of  $\alpha$ -alumina is 8 and 7 to 9 for other forms<sup>166-168</sup>. Membranes in our experiments had a positive surface charge. The pKa of Fluorescein is 6.4<sup>169</sup>, dissolved in nanopure water with a pH of  $\approx 7.2$  leaves the molecule with a small negative charge. Therefore, electrostatic interactions could also play a role in decreasing diffusivity relative to bulk diffusivity.

## 8.6. Conclusions

In conclusion, we have demonstrated a relatively simple fluorescence imaging method for measuring the time-resolved concentration profile of a fluorescent molecule diffusing through an alumina membrane. The integrated system allowed for the imaging of highly dilute concentrations at inter-cellular volumes, applicable to many biological applications including drug delivery and controlled cell growth. In addition, this system provides a relatively simple method for determining fundamental information useful for designing separation systems. While not specifically addressed here, fluorescence imaging the sample area allows for direct correlation between measured diffusivities and local macroscopic morphology. In this way, defect areas can be measured separately (or excluded completely) during analysis providing additional information of membrane integrity. It is within this ability that heterogeneous areas can be measured and quantified with the hopes of linking these variations to synthesis conditions and performance.

## **9. BREAKTHROUGH CURVES OF UNMODIFIED ANODICS AND ATOMIC LAYER DEPOSITION MODIFIED ANODISC VIA TIME-RESOLVED FLUORESCENCE MICROSCOPY**

### **9.1. Chapter Abstract**

The fluorescence imaging method reported in chapter 8 and published in Applied Physics Letters (R. Kennard, W.J. DeSisto, M.D. Mason, Molecular diffusivity measurement through an alumina membrane using time-resolved fluorescence imaging, Applied Physics Letters, 97 213701-213703)<sup>170</sup> for measuring the time-resolved concentration of a fluorescent molecule diffusing through an anodic alumina membrane with a pore size of 20nm has been expanded and descriptive models have been improved. In this chapter, Anodiscs of 20, 100, 200 nm, and modified 20nm pore sized discs by 50 and 100 Atomic Layer Deposition (ALD) cycles were studied and modeled by several different methods. A comparative study that utilized hindered diffusion models and a partial differential solution model for time dependent breakthrough curves was applied to the collected data and used to estimate adsorptive capacities.

### **9.2. Introduction**

To further the understanding of the transport mechanisms that accurately describe the diffusional behavior of fluorescein through a commercial membrane, three different anodic alumina porous discs (Anodisc<sup>TM</sup>) were studied. These membranes are characterized by a high pore density ( $10^9$  pores/m<sup>2</sup>), uniform pore size (range 20-200nm), and straight channel pores (tortuosity,  $\tau = 1$ ) with 13mm disc diameters, mean pore sizes of 20, 100, and 200 nm, thicknesses of 60  $\mu$ m and porosities of  $\approx 30$  to 35%,  $\approx 40\%$ , and  $\approx 50\%$  respectively. Two new pores sizes were created by modifying 20nm Anodisc with 50 and 100 cycles of atomic disposition of alumina (average 0.16 nm thickness/cycle), resulting in new pore sizes of approximately 12 and 4 nm respectively. In this chapter, we elaborate on the time resolved



fluorescent molecular diffusion characterization (TIF MODIF), demonstrating that the method continues to be a simple, non-labor intensive approach to characterizing transport phenomena of solute diffusion driven by a concentration gradient. While utilizing an ideal membrane, this method provides a stable and predictable means to characterize in-house modified membranes.

In chapter 8, a relatively straightforward fluorescence imaging method to measure molecular diffusion breakthrough curves from an inorganic membrane was presented<sup>170</sup>. By fitting a function that describes fluorescent dye bleaching as a function of time and concentration, coupled with a quasi-steady state Fickian diffusion expression, diffusivities of porous membranes were extracted. The model used to describe the diffusion breakthrough curves was sufficient for a 1<sup>st</sup> order approximation. However, the model discussed in chapter 8 is only valid with a uniform concentration gradient through the membrane system, as shown in Equation 9.1.

$$\text{Equation 9.1} \quad \frac{dC}{dx} = \frac{C_o - C_i}{l}$$

This equation is only valid when the accumulation of the diffusing species within the membrane is negligible compared to the accumulation of the diffusing species within the receiver vessel. The receiver vessel has a measured volume of approximately 150 nL. The membranes used have a diameter of 13mm, thickness of 65  $\mu\text{m}$  and porosities as reported by Whatman, thus the void volume is estimated to be approximately 4.3  $\mu\text{L}$ . This means that the receiver volume is negligible compared to the membrane volume and, essentially, there is no flux. Given these parameters, the membrane outlet and the concentration gradient at  $x = l$  must always be zero. Since the concentration gradient is a function of both  $x$  within the membrane and time, a partial differential equation description must be considered.

Since the void volume ( $V_i$ ) is almost 30 times smaller than the membrane volume lets one assume  $V_i$  is assumed to be zero. With that assumption, the system is equivalent to a porous slab with a step change in concentration at the top surface at time zero. The boundary condition at the

lower surface is zero concentration gradient (i.e. no flux for all t). To predict the time dependence of fluorescein concentration at the lower surface of the membrane, the system was modeled as a porous slab subjected to a step change in concentration at the surface at time zero with a zero concentration gradient at the lower surface i.e. flux is zero at  $x = \ell$ . To predict the time dependence of fluorescein concentration at the lower surface of the membrane, the well-known mathematical solution to the transient diffusion equation for a parallel sided slab presented by Crank, J.<sup>171</sup> was applied, to further our understanding of the system and to quantify the effect that adsorption dynamics have on the observed diffusional response. The results obtained from the solution to the modified model of Crank describing diffusion of an adsorbing species through a parallel slab was compared to hindered transport models of solute molecules within liquid filled pores, which describe the diffusion of species through a material that experiences just steric hindrance and the previous described quasi-steady state approximation.

### 9.3. Application of the Solution for Transient Diffusion in a Parallel-Sided Slab

Using Fick's second law of diffusion shown in Equation 9.2,

$$\text{Equation 9.2} \quad \frac{\partial C}{\partial t} = D \frac{\partial^2 C}{\partial x^2}$$

In addition, applying the boundary condition for the system defined as follows in Figure 9.1. The solution in the form of a trigonometrical series shown by Crank<sup>171</sup> is shown in Equation 9.3.

$$\text{Equation 9.3} \quad \frac{C}{C_0} = 1 - \frac{4}{\pi} \sum_{n=0}^{\infty} \frac{(-1)^n}{(2n+1)} \exp\left[\frac{-D(2n+1)^2 \pi^2 t}{4l^2}\right] \cos\left[\frac{(2n+1)\pi x}{2l}\right]$$

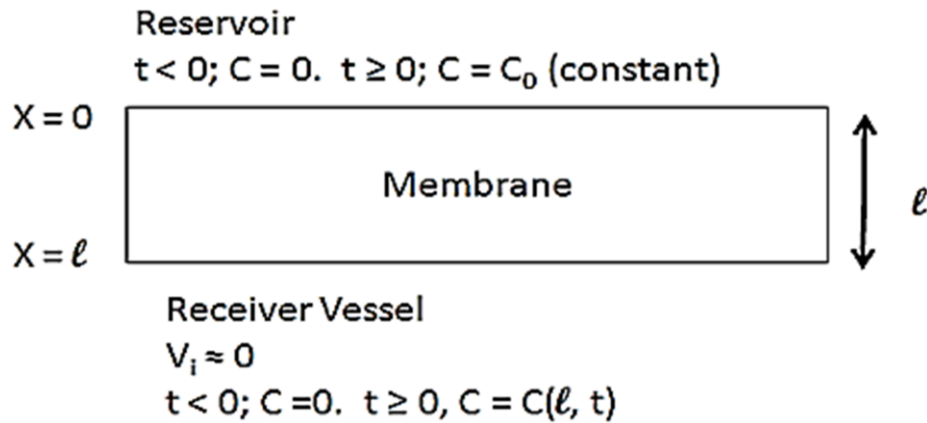


Figure 9.1 Depiction of the membrane system. Boundary conditions applied for the transient solution of diffusion within a porous parallel slab.

At  $x = 0$  the expression Equation 9.3 simplifies to Equation 9.4:

$$\text{Equation 9.4} \quad \frac{C}{C_0} = 1 - \frac{4}{\pi} \sum_{n=0}^{\infty} \frac{(-1)^n}{(2n+1)} \exp\left[\frac{-D(2n+1)^2 \pi^2 t}{4l^2}\right]$$

In most cases, the exact solution of Equation 9.4 can easily be solved numerically when coupled with the expression for photobleaching (Equation 8.7), to generate an expression that simultaneously describes the diffusional and bleaching processes present within the system. The numerical answer becomes extremely time intensive to solve and fraught with rounding errors. Therefore Equation 9.4 was broken down into two components; a solution for short times ( $C/C_0 < 0.5$ ) and one for long times ( $C/C_0 > 0.5$ ).

At long time ( $C/C_0 > 0.5$ ), only the first term is significant and Equation 9.4 can be reduced further, Equation 9.5.

$$\text{Equation 9.5} \quad \frac{C}{C_0} = 1 - \frac{4}{\pi} \exp\left[\frac{-D\pi^2 t}{4l^2}\right]$$

The useful solution for the system described above for short times ( $C/C_0 < 0.5$ ) is shown in Equation 9.6.

$$\text{Equation 9.6} \quad \frac{C}{C_0} = \sum_{n=0}^{\infty} (-1)^n \operatorname{erfc}\left[\frac{(2n+1)l-x}{2\sqrt{Dt}}\right] + \sum_{n=0}^{\infty} (-1)^n \operatorname{erfc}\left[\frac{(2n+1)l+x}{2\sqrt{Dt}}\right]$$

In addition, at  $x = 0$  Equation 9.6 can be simplified to Equation 9.7.

$$\text{Equation 9.7} \quad \frac{C}{C_0} = 2\operatorname{erfc}\left[\frac{l}{2\sqrt{Dt}}\right]$$

Using the expressions for long time and short time shown in Equation 9.5 and Equation 9.7, each recorded data set can be simultaneously fit to extract diffusional constants for fluorescein molecules within each alumina membrane system. A similar calculation was described in section 8.4 using Equation 8.8. The contribution of adsorption to the decrease of the diffusion coefficients predicted by the parallel slab model can be quantified by comparing the results with a hindered diffusion model that accounts for just physical restriction of diffusing particles within a pore. Careful analysis of these two models also yields the saturation capacities for the anodic membranes.

#### 9.4. Hindered Diffusion

In cases where the solute is assumed to act as a hard sphere and is much larger than the solvent, the resistance to Brownian motion may be equated to the Stokes-Einstein equation that was derived from equating the diffusional velocity to the viscous drag according to Stokes' Law. In cases where the solute particles are not spherical, the Wilke-Chang correlation provides a more accurate approximation of the diffusional coefficient.

For solute particles, whose sizes approach the pore radii, hindered diffusion occurs when the chemical physical interactions between the solute and pore wall cause the molecular friction coefficient to exceed the value of a free solution. This hindered diffusion is dependent on size of the molecule, pore size, electrostatic interactions, and shape of the molecule and pore. This phenomenon is largely observed in biological systems, such as renal and extrarenal microcirculation<sup>35-44</sup>, with applications to separations for enzyme and size exclusion chromatography<sup>45-49</sup>.

Under steady state conditions and low solvent flow rates; (i.e.  $Pe \ll 1$ , the Peclet number based on the pore length), the effective diffusivity ( $D_{eff}$ ) for a solute diffusing through a membrane with long cylindrical pores, orthogonal to the membrane surface, can be separated into four parts; the porosity ( $\epsilon$ ), the partition coefficient ( $\Phi$ ), a function of pore radius ( $r_p$ ) and solute radius ( $r_s$ ), Equation 9.8, the bulk diffusivity, and the hydrodynamic hindrance factor ( $H$ ).

Equation 9.8

$$D_{eff} = \epsilon \Phi D_{\infty} H$$

where

$$\Phi = \left[ 1 - \frac{r_s}{r_p} \right]^2$$

The only component that is unknown for a system under these conditions is the hydrodynamic hindrance factor. Due to the vast sensitivities of diffusional responses to many other parameters, it is difficult to completely understand and account for the individual components such that an explicitly derived expression can be found. Therefore, a number of numerical approximations have been developed that yield fairly accurate predictions<sup>50</sup> of diffusion within a liquid filled pore. A review covering the most widely accepted expressions for the hydrodynamic hindrance factors, along with treatments of the hindrance effect of convective diffusion ( $Pe \rightarrow 1$ ), and the effect of electrostatic interactions has been presented by W. M. Deen<sup>51</sup>. By examining these models in conjunction with a model that accounts for both diffusion and adsorption processes, it may be possible to extract, mathematically, the adsorption capacities for the systems in question.

## **9.5. Experimental Section**

### **9.5.1. Atomic Layer Deposition of Anodic Alumina Membranes**

Whatman Anodiscs (0.02  $\mu\text{m}$ ) were placed inside a Nor-cal chamber for modification. ALD was carried out at 100°C and  $\leq 5$  mTorr using trimethyl aluminum (TMA, Sigma Aldrich) and H<sub>2</sub>O as reactants.<sup>172</sup> The TMA and H<sub>2</sub>O were held at 0°C, producing vapor pressures of 2.56 and 4.60 Torr, respectively. The membrane was dosed with each precursor for 1 second over the top of the membrane. These exposure times approach the minimal interlude for alumina ALD.<sup>173</sup> To evacuate the cell, it was held under vacuum for 2 minutes. Then, N<sub>2</sub> was purged for 30 seconds at 30 sccm. This purge cycle was repeated to remove all non-adsorbed reactant from the pore network. The typical coating cycle sequence was; dose TMA, evacuate excess TMA, N<sub>2</sub> purge, evacuate, N<sub>2</sub> purge, evacuate, dose H<sub>2</sub>O, evacuate excess H<sub>2</sub>O, N<sub>2</sub> purge, evacuate, N<sub>2</sub> purge, and evacuate. This complete cycle resulted in one monolayer of Al<sub>2</sub>O<sub>3</sub> deposited within the pores. The membranes were modified by 50 and 100 cycles. These samples will be further referred to as 50 ALD and 100 ALD respectively.

### 9.5.2. Fluorescence Measurements

All 5 disc types were prepared and studied in the same manner as described in sections 8.3.3 and 8.3.5. Since the stability and the response of the microscope had been characterized in chapter 8, only one excitation power (800  $\mu\text{W}$ ) and one loading concentration (340 nM) was used for this study.

## 9.6. Results and Discussion

### 9.6.1. Parallel Sided Slab

The analysis described above was applied to the data sets that were collected. The defined parameters that were held constant for the step wise curve fit were as follows;  $I_0$  (800  $\mu\text{W}$ ) is the excitation energy used to produce the raw data in watts,  $C_0$  is the loading concentration of fluorescein (340 nM),  $\epsilon$  is the membrane porosity;  $A$  is the active cross sectional transport area ( $1 \text{ cm}^2$ );  $l$  is the membrane thickness (60  $\mu\text{m}$ ). The shared undefined parameters between all experiments were  $\Phi_{\text{ext}}$ , the excitation efficiency of the system;  $V$ , the estimate void volume ( $\text{cm}^3$ );  $\tau$ , the lifetime of the fluorescent molecule in the system ( $\text{s}^{-1}$ ); and  $\beta$ , the stretched exponential fitting parameter. The remaining parameters:  $D$ , the molecular diffusivities ( $\text{cm}^2 \text{ s}^{-1}$ );  $y_0$ , the system fluorescent background; and  $A_0$ , molecular quantum efficiency were allowed to independently float within predetermined ranges for each data set. Once the fits were completed, the results were used to produce a model curve to represent the raw data. Each raw data set and its model representation was then divided by the  $EB(t)$  function to remove the effects of bleaching, Equation 8.8, using the parameters from that curves' model fit. This produced a set of diffusion breakthrough curves for each Anodisc studied. The results from the solution presented in Equation 9.7 for short times are shown in Figure 9.2. The resulting diffusivities for the 100 ALD, 50 ALD, 20, 100, and 200nm Anopore discs from the simultaneous fits are shown in Table 9-1. In order to explain these discrepancies, compared to literature values, further analysis of the diffusion breakthrough curves was performed.

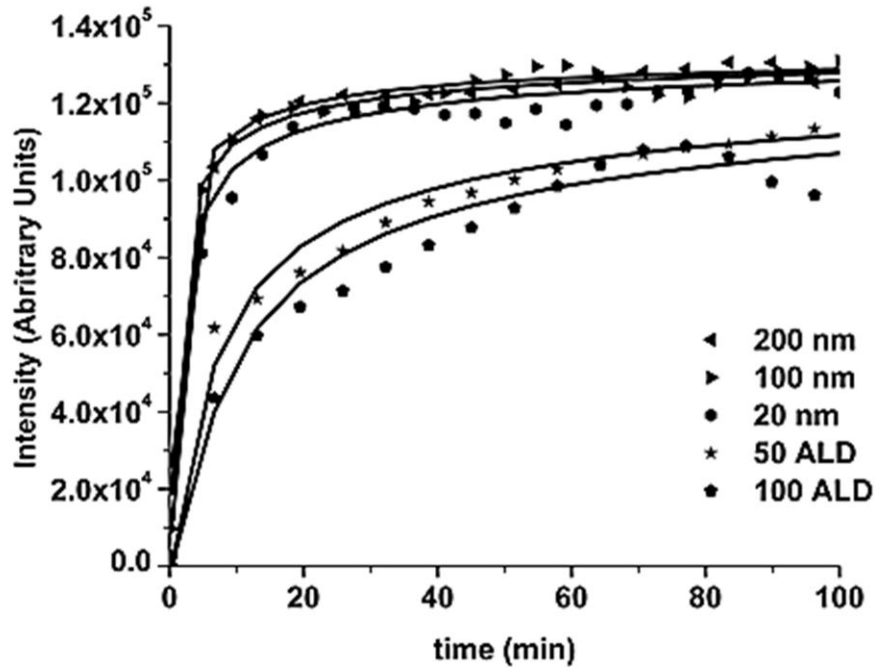


Figure 9.2 The plot shows the corrected diffusion data. The data is shown as points and simultaneous fit of the model described for short times shown as solid lines. To simplify the figure for viewing every tenth point is shown for the first 100 min

### 9.6.2. Hindered Diffusion

Using the Stokes-Einstein equation (Equation 3.14) and the Wilke –Chang correlation (Equation 3.15), the bulk diffusivity constant for fluorescein in water was estimated. Assuming fluorescein has a hydrodynamic radius of 0.4nm, and in water at 20 °C, the diffusivity was determined to be  $5.35 \times 10^{-5} \text{ cm}^2 \text{ s}^{-1}$  using the Stokes-Einstein expression<sup>99</sup> and  $4.9 \times 10^{-6} \text{ cm}^2 \text{ s}^{-1}$  using the Wilke-Chang correlation<sup>34</sup>.

As a solute particle moves from a free solution matrix to a constricted cylindrical tube, whose radius begins to approach the molecular radius of the particle, drag affects and collision between the molecule and the wall of the cylinder begin to slow the diffusion of these solute particles. Numerous models and approximations have been used to account for the difference



between the observed hindered diffusivities and the unhindered diffusivity predicted by the Stokes-Einstein or Wilke-Chang relationships<sup>50, 51, 174</sup>. Two different forms of hindered diffusion approximations, dependent on the solute transport mechanism, are dominated by diffusion for low solvent velocities, or convection for high solvent velocities, have been discussed by Deen, W.M.(1987)<sup>51</sup>. Since the solvent's mean velocity in this study is zero, we have assumed that all hindered diffusion is due to steric hindrance of solute molecules and have employed the diffusion dominated approximation for hindered diffusion shown in Equation 9.9

$$\text{Equation 9.9} \quad D_{\text{eff}} = HD_0$$

Where  $D_0$  is the Stoke-Einstein or Wilke-Chang free diffusivity,  $H$  is the hindered hydrodynamic coefficient, and  $D_{\text{eff}}$  is the effective diffusivity. Since the distribution coefficient ( $\phi = (1 - \lambda)^2$ , where  $\lambda = r_s/r_p$ ,  $r_s$  is the solute radii and  $r_p$  is the pore radii) in all five cases (assuming the ALD layer thickness is  $\leq 1.6 \text{ \AA/cycle}$ ) is greater than 0.9; the approximation for  $H$  (Equation 9.10) given by Brenner and Gaydos<sup>175</sup> applies.

$$\text{Equation 9.10} \quad H = 1 - \left[ \frac{9}{8} \right] \lambda \ln \lambda^{-1} - 1.539\lambda$$

Diffusivities ( $\text{m}^2\text{s}^{-1}$ )					
Average pore radii (nm)	Quasi-steady state $D_f \times 10^{-13}$	Short time $D_f \times 10^{-11}$	Long time $D_f \times 10^{-11}$	Hindered Diffusivities <sup>‡</sup> $D_h \times 10^{-9}$	Hindered Diffusivities <sup>†</sup> $D_h \times 10^{-10}$
200	1.42	6.60	3.35	5.26	4.82
100	1.00	4.08	2.32	4.15	3.80
20	0.76	2.31	0.77	3.30	3.02
50 ALD	0.57	0.42	0.35	3.08	2.81
100 ALD	0.31	0.28	0.28	2.20	2.02

Table 9-1 Summary of all measured and calculated diffusivities. ‡ Diffusivities calculated using Equation 3.14 using the free Diffusivities predicted from the Stokes-Einstein equation. † Diffusivities calculated using Equation 3.15 and the freed diffusivity predicted via the Wilke-Chang correlation.

Using the calculated hydrodynamic coefficients for each Anodisc, the new diffusivity coefficients calculated for Anodisc 50ALD, 100ALD, 20, 100, and 200 nm respectively are reported in Table 9-1. It is important to note that the diffusion constant predicted by the parallel sided slab model correlates with previously reported literature values<sup>101</sup>. Using these diffusivities and those predicted by Equation 9.5 and Equation 9.7 for long and short times respectively, expected diffusion breakthrough curves were generated for each disc.

Comparing the experimental breakthrough curve with the calculated curve assuming only hindered diffusion (Figure 9.3) indicates a significant lag in the breakthrough (20nm membrane). It is the difference between these two breakthrough curves that is used to investigate the physical and chemical changes between the Anodiscs and the ALD modified surfaces. Since the parallel-sided slab model accounts for both diffusion and adsorption, and the hindered diffusion model only accounts for increase in diffusional lag time due to steric hindrance, the difference between the two breakthrough curves must be due to solute adsorption by the porous structure. In order to find the values of the loading capacity of each Anodisc system, the

difference in the dye “hold-up” within the membrane (saturation capacity) was calculated using Equation 9.11;

$$\text{Equation 9.11} \quad M_{\infty} = \left\{ \int_0^{\infty} C_h(t) dt - \int_0^{\infty} C_f(t) dt \right\} V$$

where  $C_h(t)$  is the function of concentration at the outlet of the membrane for short and long times, using the hindered diffusion constant,  $C_f(t)$  is the fluorescent measured diffusion breakthrough curve and  $V$  is the volume of the doping solution. The saturation capacity of the Anodisc predicted by the results of Equation 9.11 was compared to a theoretical maximum loading of dye molecules onto the surface of a cylinder with a surface hydroxyl concentration<sup>73, 176</sup> of 9.6% to verify that the physical limits have not been exceeded. This theoretical physical limit of adsorption was an order of magnitude higher than the experimental values calculated by the above model, indicating an upper limit to adsorption was not exceeded. However, an unexpected phenomenon was uncovered during this analysis. In calculation of the surface area of each disc, based on information reported by Whatman, it has been assumed that the 200nm pore discs are 60  $\mu\text{m}$  thick resulting in a calculated area of 300  $\text{cm}^2$ . The 100nm disc are a bi-layer system made of 58  $\mu\text{m}$  thick layer with 200 nm pores and the last 2  $\mu\text{m}$  are the 100nm pores. This produces a surface area of 306  $\text{cm}^2$ . The 20 nm discs are actually a tri-layer system with 56 $\mu\text{m}$  of 200nm pores, 2 $\mu\text{m}$  of 100 nm pores, and 2 $\mu\text{m}$  of 20nm pores resulting in a surface area of 366  $\text{cm}^2$ . When calculating the surface area of the ALD modified disc it was assumed that either the pores of the disc were uniformly coated, or the alumina layer was solid and the layer thickness was constant for all layers of ALD modification. Using this assumption, the calculated surface areas of the 20nm ALD modified Anodisc with 50 and 100 layers were found to be 326 and 285  $\text{cm}^2$  respectively. When comparing the individual saturation capacities of each of the five discs, the capacity for the modified disc with 50 and 100 ALD layers actually have an

increased saturation capacity compared to their decreased area, these values are shown in Table 9-2. There are several possible explanations for the increase in surface loading. One

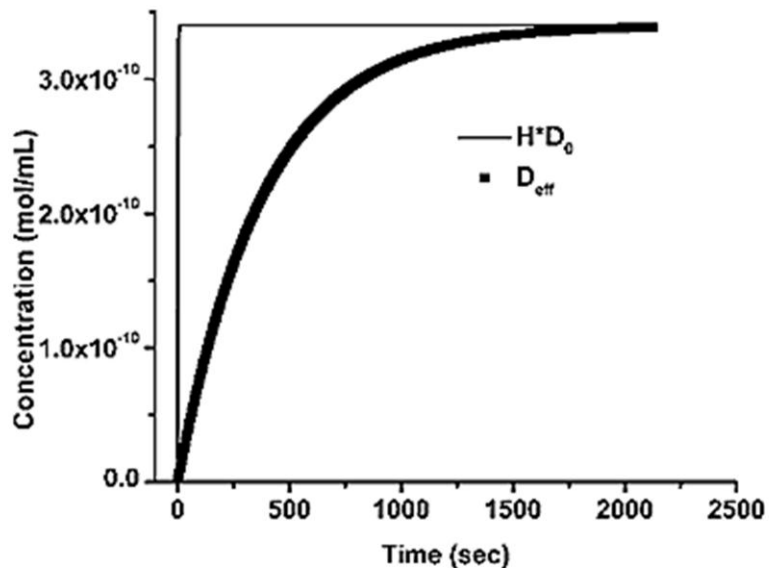


Figure 9.3 Plot showing two breakthrough curves. The data breakthrough curve is shown by the thick line and hindered diffusion breakthrough curve is shown by the thin line

explanation is that the ALD modification has increased the amount of binding groups on the alumina surface. It has been shown that the adsorption of carboxylic groups onto alumina is very strong with adsorption energies larger than those of most organic compounds<sup>177</sup>. Although only recently have carboxylic acid adsorption dynamics been studied in aqueous solutions<sup>71, 72</sup>. It has been suggested that adsorption dynamics between the alumina and carboxylic acid is a dissociative process<sup>71</sup>. The adsorbed carboxylic acid may interact with the alumina surface in a manner that a hydrogen atom is shared between each oxygen atom in the carboxylic group and the oxygen atom on the alumina surface forming a strong hydrogen bond<sup>73, 176</sup>.

In order to demonstrate that the observed decrease in diffusivity of the ALD modified anodiscs is due to a change in the physical structure, and not to a change in the chemical structure (increasing the surface adsorption sites), plots of equilibrium adsorption times as a function of the

Average pore radii (nm)	Surface Area (cm <sup>2</sup> ) <sup>A</sup>	q x 10 <sup>-11</sup> (mol/cm <sup>2</sup> ) <sup>B</sup>	q x 10 <sup>-11</sup> (mol/cm <sup>2</sup> ) <sup>C</sup>	Numerical approximation q x 10 <sup>-10</sup> (mol/cm <sup>2</sup> ) <sup>D</sup>
200	300	3.10	2.06	2.59
100	306	3.03	2.03	2.80
20	366	2.24	1.69	3.65
50 ALD	326	2.49	1.90	3.46
100 ALD	285	3.21	2.18	3.23

Table 9-2 Adsorption capacities predicted by various models. A.) shows the estimated surface areas assuming 1.6 nm average ALD layer thickness. Maximum adsorptive capacities calculated from Equation 9.11 with Wilke-Chang correlation for short times B.) and long times C.) In addition, D.) estimated maximum capacities based on surface area approximations of 9.6% surface hydroxyl coverage.

number of ALD layers were generated under the assumption that the adsorption site density and chemical composition of the ALD layer were the same as that of the 20nm Anodisc. Four average layer thickness per ALD cycle were chosen; 1.0, 1.5, 2.1, and 4.1nm. This allows for the calculation a theoretical maximum loading of an ALD modified disc based on the disc's surface area, which is a function of number of layers added and the thickness of each layer. The adsorption equilibrium time can be found numerically using this calculation in conjunction with Equation 9.9 and, assuming that the bulk reduction of the observed diffusion constant is directly proportional to the reduction of surface area and the hindered diffusion prefactor. The results of this study; shown in Figure 9.4; demonstrate that, with a uniform and constant ALD layer thickness, equilibrium time should increase linearly until the pore size is reduced to approximately 4nm. At this point, the equilibrium increases exponentially and the system becomes diffusion controlled. This analysis is consistent with observations in literature of decreasing growth rates with pore size reduction<sup>178</sup>, and demonstrates that a complete uniform ALD layer modification cannot explain the resulting increase of saturation capacity for the 50 and 100 layer-modified discs.

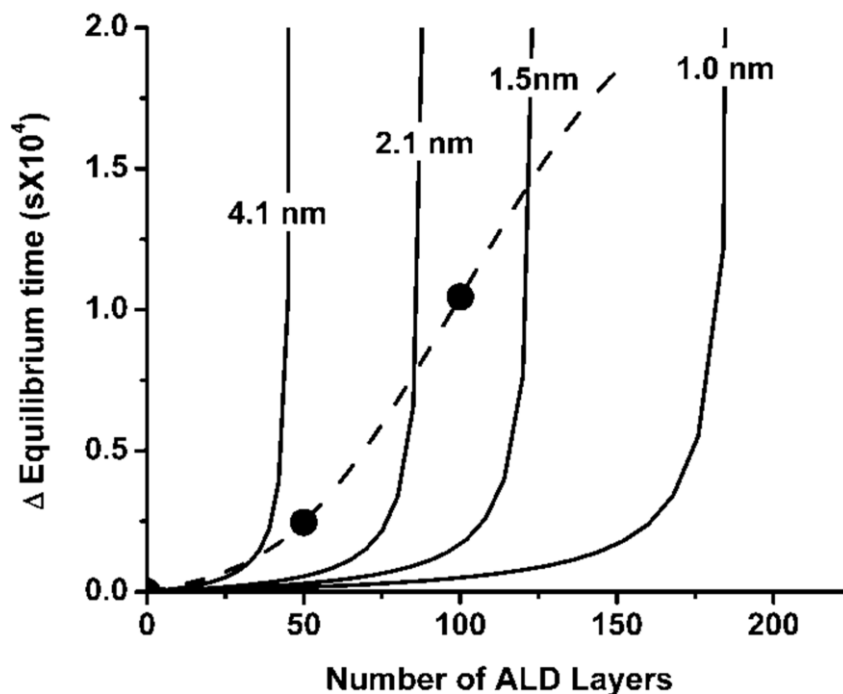


Figure 9.4 Theoretical curves showing the increase of equilibrium times. Each solid line represents the effect of average ALD layer thickness of 4.1, 2.1, 1.5, and 1.0nm respectively. The points are the measured increase of equilibrium times for a 50 and 100 layer ALD modified disc. The dashed line is the estimated response of ALD layers based on measured values, and is only used as a visual aid.

### 9.6.3. Lag-Time Analysis

To ensure the observed behavior is due to adsorption, a lag-time analysis was applied to the bleach corrected data. The lag time analysis was developed by Daynes (1920) and Barrer (1951)<sup>179</sup> and is useful in determining the diffusion constant of a species by monitoring stationary and non-stationary flow through a membrane. This technique is similar to the methods discussed in chapter 8 and in this chapter. By comparing the measured diffusivities of the fluorescent concentration breakthrough curve to the time lag analysis, one may be able to confirm the presence of adsorption within the membrane system.

A modified time-lag analysis proposed by Frisch(1957) suggests that not only the diffusion constant but also the solubility constant of the diffusant within the membrane system<sup>180</sup>,

<sup>181</sup> can be determined. This approach has been utilized several systems such as radon diffusion and solubility constant within membranes<sup>182</sup>, as well as helium diffusion in PTFE tubes<sup>183</sup>. The modified time-lag expression can be derived if the diffusion coefficient remains constant over time and if there is a linear relationship between the concentration of the diffusing species and the concentration of the species within the membrane. Due to the lack of high resolution at short time, the results from this analysis are not considered reliable but they are nevertheless included in Appendix E.

## 9.7. Conclusions

Further analysis of concentration breakthrough curves for fluorescein diffusing through several different commercially available Anodiscs and in house modified discs has demonstrated that the new system can accurately measure these membranes. With careful analysis, diffusion coefficients can be extracted that correlate with previously reported values. The observed aberrations from hindered diffusional models and parallel-sided models can be attributed to the hold up of diffusion due to adsorption of the solute particles within the membrane. The results suggest a direct relationship between the increase in adsorption capacity and the extent of modification via ALD. It is important to note that this result is counter intuitive, i.e. a decrease in surface area should correlate to a decrease in adsorption capacity. It has been reported that as much as 5% of the anodized portion of the anodic alumina membrane are acid aluminum oxalate anions incorporated into the surface during anodizing<sup>184-186</sup>. These oxalate anions are thermally stable up to 900°C but have been shown to be coated via ALD<sup>187</sup>. If the oxalate anions are present, there is a fundamental chemical difference between an unmodified disc and an ALD modified disc. It is hypothesized that the aluminum oxalate contamination limits the amount of fluorescein, adsorption on to the surface alumina surface. This fundamental chemical surface change could explain the increase in adsorption capacity for fluorescein, despite the decreasing surface area with ALD modification. However, this explanation does not account for the increase

in adsorption capacity between 50 to 100 ALD modified discs. In order to explain this observation another hypothesis must be entertained. It is believed that the ALD modification process implemented did not effectively modify the entire pore length. Instead, only the top section was affected. After each subsequent layer, the modification was able to penetrate further into the pore, see Figure 9.5. If the reaction time did not account for the high aspect ratio of the pore diameter to pore length (20nm vs. 2  $\mu\text{m}$ , 1:100), each the reactant for ALD layer would not have enough time to diffuse into the membrane system and effectively modify the Anodisc with a full monolayer. If in fact, the modifications were partial monolayers, the following layers would complete the areas deep within the membrane with partial coverage. Over time the contaminated Anodisc surface would become covered and increase its adsorption capacity.

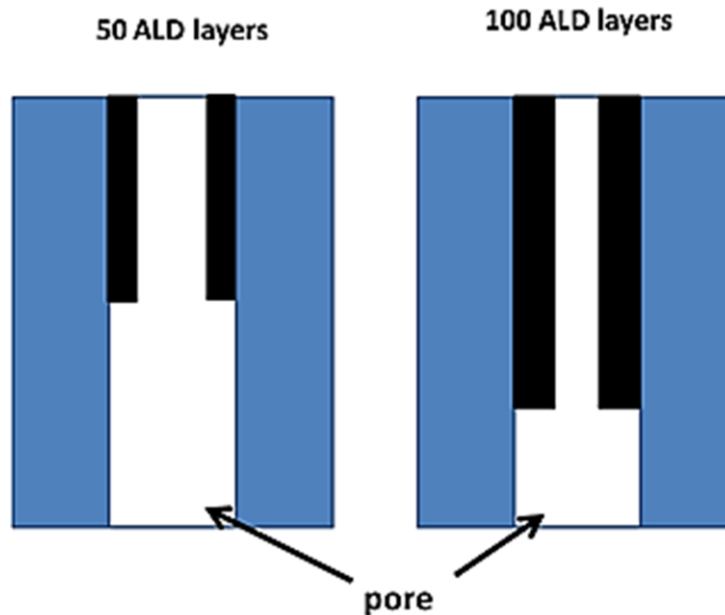


Figure 9.5 How ALD may increase adsorption site density and reduce surface area.



In conclusion, we have expanded the capabilities of a relatively simple fluorescence imaging method for measuring the time-resolved concentration profile of a fluorescent molecule diffusing through an alumina membrane. The integrated system allows for the imaging of highly dilute concentrations at inter-cellular volumes, applicable to many biological applications including drug delivery and controlled cell growth. In addition, this system provides a relatively simple method for determining fundamental information useful for designing separation systems. The fluorescence imaging of the sample area allows for direct correlation between measured diffusivities and local macroscopic morphology such as ALD growth and its effects on adsorptive behavior. However, more studies need to be performed to determine the reason for the change in adsorption capacity. It is recommended to have an ALD modified cross-sectional SEM image recorded to determine the uniformity of the modification. Alternatively, the fluorescent technique could be utilized by performing transient measurements with a larger number of modified ALD membranes, with varying pH to determine the effects of electrostatic interactions.

## 10. SUMMARY AND FUTURE WORK

### 10.1. Summary

This thesis describes the novel application of previously developed single molecule imaging spectroscopy to characterize the local intrinsic heterogeneity in inorganic systems in such a manner that leads to the methods sensitive enough to link synthesis conditions to physical and chemical properties and elucidate their connections to transport properties. Our goals were to:

1. Determine the viability of applying fluorescent spectroscopic methods to porous inorganic membrane systems.
2. Measure an intrinsic property of a porous membrane on the molecular level, i.e. Henry law constants.
3. Develop a new fluorescent technique to measure dynamic membrane properties based on near single molecule concentrations, such as diffusion rates and adsorptive behavior.

It was shown in CHAPTER 6 that using single molecule imaging spectroscopy to characterize, quantitatively, the interaction between the probe molecule and the interior of the pore within mesoporous silica membranes is viable. This approach is radically different from typical membrane characterization methods in that it has the potential to sample, spatially, the underlying pore structure distribution, the surface energy, and the transport properties. The potential to use this new fundamental knowledge can be quantitatively linked to both the preparation and the performance of membranes leading to the advancement of membrane science and technology.

CHAPTER 7 demonstrated the ability for Fluorescent Activation Localization Microscopy (FPALM) to spatially map and identify membrane defects smaller than the optical diffraction limit. This technique provides a quick and cheap alternative to characterize membrane

homogeneity with direct applications to membrane synthesis quality control for industrial processes.

The contents of CHAPTER 8 and CHAPTER 9 presents a new simple fluorescence imaging method for measuring the time-resolved concentration of a fluorescent molecule diffusing through a anodic alumina membrane with a pore diameter of 20 nm, 100nm, 200nm, and ALD modified Anodisc allowing the measurement of diffusion constants of molecules within a liquid filled pore with near sub ensemble condition. Further analysis of the time dependent breakthrough diffusion curve allowed for the extraction of adsorption capacities. By comparing, the change in adsorption capacities of the each disc with respect to surface area measured, a chemical change in the surface adsorption site concentration via ALD modification was observed.

## **10.2. Future Work**

The preliminary work in this thesis has demonstrated the sensitivity of fluorescent spectroscopy to measure key properties of inorganic membranes such as adsorption constants, adsorption capacities, and diffusion on a local and molecular sub ensemble level. However to be able to correlate any changes in these properties to specific synthesis conditions, more intensive characterization should be performed. Suggested studies include:

1. Vary the dye concentration for the method described in CHAPTER 8 and CHAPTER 9 to construct adsorption isotherms
2. Vary the temperature for the method described in CHAPTER 8 and CHAPTER 9 to measure the Henry law constant for each type of membrane
3. Vary the dye size and chemical structure for all of the fluorescent techniques presented here
4. Chemically modify membrane (sol-gel and amine modification) and repeat concentration, temperature and pore size studies

- a. It should be noted that studies of isopropyl amine modified anodiscs has already begun. Preliminary results suggest that the adsorptive behavior of fluorescein to the Anodisc surface has been greatly reduced.
5. Construct flow cell geometry for the method described in CHAPTER 8 and CHAPTER 9

This thesis and the suggested further studies has the potential to characterize the local intrinsic heterogeneity in inorganic systems with details and the sensitivities to link synthesis conditions to physical and chemical properties and elucidate their connections to transport properties and create a guide for creating a successful membrane system.

## BIBLIOGRAPHY

1. A. J. Burggraaf and L. Cot, in *Membrane Science and Technology Series, 4*, edited by A. J. Burggraaf and L. Cot (Elsevier, Amsterdam, 1996).
2. L. Reimer and H. Kohl, *Transmission Electron Microscopy: Physics of Image Formation*. (Springer, Berlin/Hiedelberg, 2008).
3. F. W. D. Rost, *Fluorescence microscopy*. (Cambridge University Press, 1995).
4. Y. Fu, F. Ye, W. G. Sanders, M. M. Collinson and D. A. Higgins, *Journal of Physical Chemistry B* **110** (18), 9164-9170 (2006).
5. E. A. J. Reits and J. J. Neefjes, *Nat Cell Biol* **3** (6), E145-E147 (2001).
6. B. L. Sprague and J. G. McNally, *Trends in Cell Biology* **15** (2), 84-91 (2005).
7. W. E. Moerner, *Journal of Physical Chemistry B* **106** (5), 910-927 (2002).
8. E. Betzig, G. H. Patterson, R. Sougrat, O. W. Lindwasser, S. Olenych, J. S. Bonifacino, M. W. Davidson, J. Lippincott-Schwartz and H. F. Hess, *Science* **313** (5793), 1642-1645 (2006).
9. T. J. Gould and S. T. Hess, in *Methods in Cell Biology*, edited by J. C. Dr. John and Dr. H. William Detrich, III (Academic Press, 2008), Vol. Volume 89, pp. 329-358.
10. S. T. Hess, T. P. K. Girirajan and M. D. Mason, *Biophysical Journal* **91** (11), 4258-4272 (2006).
11. P. Aptel, J. Armor, R. Audinos, R. W. Baker, R. Bakish, G. Belfort, B. Bikson, R. G. Brown, M. Bryk, J. J. Burke, I. Cabasso, R. T. Chern, M. Cheryan, E. L. Cussler and R. H. Davis, *Journal of Membrane Science* **120** (2), 149-159 (1996).
12. A. L. Z. Leos J. Zeman, *Microfiltration and Ultrafiltration, Principles and Applications*. (CRC, New York, 1996).
13. G. P. H. Dietz and M. Bhr, *Molecular and Cellular Neuroscience* **27** (2), 85-131 (2004).

14. D. J. Eilbott, N. Peress, H. Burger, D. LaNeve, J. Orenstein, H. E. Gendelman, R. Seidman and B. Weiser, *Proceedings of the National Academy of Sciences* **86** (9), 3337-3341 (1989).
15. K. C. Williams and W. F. Hickey, *Annual Review of Neuroscience* **25** (1), 537-562 (2002).
16. S. L. Glynn and M. Yazdanian, *Journal of Pharmaceutical Sciences* **87** (3), 306-310 (1998).
17. J. Marchand-Brynaert, *Encyclopedia of Surface and Colloid Science: Second Edition*, 4854 - 4873 (2006).
18. Y. S. Lin, J. Meijerink, H. W. Brinkman, K. J. de Vries and A. J. Burggraaf, Montpellier, Fr, 1991 (unpublished).
19. Y. S. Lin, *Separation and Purification Technology* **25** (1-3), 39-55 (2001).
20. A. W. Ott, J. W. Klaus, J. M. Johnson, S. M. George, K. C. McCarley and J. D. Way, *Chemistry of Materials* **9** (3), 707-714 (1997).
21. A. A. Dameron, S. D. Davidson, B. B. Burton, P. F. Carcia, R. S. McLean and S. M. George, *The Journal of Physical Chemistry C* **112** (12), 4573-4580 (2008).
22. B. B. Lakshmi, C. J. Patrissi and C. R. Martin, *Chemistry of Materials* **9** (11), 2544-2550 (1997).
23. J. C. Hulteen and C. R. Martin, *Journal of Materials Chemistry* **7** (7), 1075-1087 (1997).
24. S. P. Sutera and R. Skalak, *Annual Review of Fluid Mechanics* **25** (1), 1-20 (1993).
25. M. Knudsen, *Annalen der Physik* **333** (1), 75-130 (1909).
26. Y. Yampolskii and B. Freeman, (Wiley, 2010).
27. W. Henry, *Philosophical Transactions of the Royal Society of London* **93**, 29-274 (1803).
28. I. Langmuir, *Journal of the American Chemical Society* **37** (5), 1139-1167 (1915).

29. I. Langmuir, *Journal of the American Chemical Society* **40** (9), 1361-1403 (1918).
30. S. Brunauer, P. H. Emmett and E. Teller, *Journal of the American Chemical Society* **60** (2), 309-319 (1938).
31. W. T. Thomson, *Phil. Mag* **42**, 448-448 (1871).
32. P. Chang and C. R. Wilke, *The Journal of Physical Chemistry* **59** (7), 592-596 (1955).
33. A. Akgerman, *Industrial and Engineering Chemistry, Fundamentals* **15** (1), 78-79 (1976).
34. S. A. Rani, B. Pitts and P. S. Stewart, *Antimicrobial Agents And Chemotherapy* **49** (2), 728-732 (2005).
35. R. C. K. Blantz, K. S.; Tucker, B. J., *The Journal of Clinical Investigation* **57** (2), 16 (1976).
36. W. M. Deen, M. P. Bohrer and B. M. Brenner, *Kidney Int* **16** (3), 353-365 (1979).
37. B. M. Brenner, M. P. Bohrer, C. Baylis and W. M. Deen, *Kidney Int* **12**, 229-237 (1977).
38. W. M. Deen, M. P. Bohrer, C. R. Robertson and B. M. Brenner, *Fed Proc* **36**, 2614-2618 (1977).
39. W. M. Deen, I. F. Ueki and B. M. Brenner, *Am J Physiol* **231**, 283-291 (1976).
40. E. M. Landis and J. F. Pappenheimer, *Handbook of Physiology* **2**, 961-1034 (1963).
41. J. R. Pappenheimer, *Physiol Rev* **33**, 387-423 (1953).
42. E. M. Renkin, *Circ Res* **41**, 735-743 (1977).
43. E. M. Renkin, *Microvasc Res* **15**, 123-135 (1978).
44. E. M. Renkin and J. P. Gilmore, (*International Society of Nephrology*, 1973), pp. 185-248.

45. M. M. Hossain, D. D. Do and J. E. Bailey, *AIChE Journal* **32** (7), 1088-1098 (1986).
46. E. Ruckenstein and M. C. Tsai, *AIChE Journal* **27** (4), 697-699 (1981).
47. D. C. Prieve and P. M. Hoysan, *Journal of Colloid and Interface Science* **64** (2), 201-213 (1978).
48. E. F. Casassa and Y. Tagami, *Macromolecules* **2** (1), 14-26 (1969).
49. E. Klein, F. F. Holland and K. Eberle, *Journal of Membrane Science* **5**, 173-188 (1979).
50. J. M. Nitsche and G. Balgi, *Industrial and Engineering Chemistry Research* **33** (9), 2242-2247 (1994).
51. W. M. Deen, *AIChE Journal* **33** (9), 1409-1425 (1987).
52. D. M. Ruthven, *Principles of Adsorption and Adsorption Processes*, 1st ed. (Wiley Interscience, 1984).
53. M. C. Blanco, J. Iturriaga, H. Maspoch, S. De la Pezuela, C., *ANALYST -LONDON-SOCIETY OF PUBLIC ANALYSTS THEN ROYAL SOCIETY OF CHEMISTRY* **123** (8), 135R-150R (1998).
54. R. Ikan, B. Crammer and A. M. Robert, in *Encyclopedia of Physical Science and Technology* (Academic Press, New York, 2001), pp. 459-496.
55. M. Forina, M. Casale, P. Oliveri, D. B. Stephen, Rom, x00E, Tauler and W. Beata, in *Comprehensive Chemometrics* (Elsevier, Oxford, 2009), pp. 75-128.
56. Y. J. Chabal, *Surface Science* **168** (1-3), 594-608 (1986).
57. V. A. Burrows, Y. J. Chabal, G. S. Higashi, K. Raghavachari and S. B. Christman, *Applied Physics Letters* **53** (11), 998 (1988).
58. Y. Piao, H. Lim, J. Y. Chang, W.-Y. Lee and H. Kim, *Electrochimica Acta* **50** (15), 2997-3013 (2005).



59. P. P. Mardilovich, A. N. Govyadinov, N. I. Mukhurov, A. M. Rzhetskii and R. Paterson, *Journal of Membrane Science* **98** (1-2), 131-142 (1995).
60. M. H. Hassan, J. Douglas Way, P. M. Thoen and A. C. Dillon, *Journal of Membrane Science* **104** (1-2), 27-42 (1995).
61. N. Agoudjil, S. Kermadi and A. Larbot, *Desalination* **223** (1-3), 417-424 (2008).
62. M. Q. Snyder, B. A. McCool, J. DiCarlo, C. P. Tripp and W. J. DeSisto, *Thin Solid Films* **514** (1-2), 97-102 (2006).
63. M. Zhang, A.-Q. Zhang, B.-K. Zhu, C.-H. Du and Y.-Y. Xu, *Journal of Membrane Science* **319** (1-2), 169-175 (2008).
64. S. Koga, T. Yakushiji, M. Matsuda, K.-i. Yamamoto and K. Sakai, *Journal of Membrane Science* **355** (1-2), 208-213.
65. S. Wijaya, M. C. Duke and J. C. Diniz da Costa, *Desalination* **236** (1-3), 291-298 (2009).
66. H.-C. Chiu, C.-H. Liu, S.-C. Chen and S.-Y. Suen, *Journal of Membrane Science* **337** (1-2), 282-290 (2009).
67. A. Bottino, G. Capannelli, V. D'Asti and P. Piaggio, *Separation and Purification Technology* **22-23**, 269-275 (2001).
68. J. Weichart and J. Müller, *Journal of Membrane Science* **86** (1-2), 87-93 (1994).
69. C. Hibshman, C. J. Cornelius and E. Marand, *Journal of Membrane Science* **211** (1), 25-40 (2003).
70. F. Meng, B. Liao, S. Liang, F. Yang, H. Zhang and L. Song, *Journal of Membrane Science* **361** (1-2), 1-14.
71. Y. Mao and B. M. Fung, *Journal of Colloid and Interface Science* **191** (1), 216-221 (1997).
72. H. Uslu and I. s. İnci, *Journal of Chemical & Engineering Data* **54** (7), 1997-2001 (2009).

73. J. E. Crowell, J. G. Chen and J. T. Yates Jr, *Journal of Electron Spectroscopy and Related Phenomena* **39**, 97-106 (1986).
74. M. E. Karaman, D. A. Antelmi and R. M. Pashley, *Colloids and Surfaces A: Physicochemical and Engineering Aspects* **182** (1-3), 285-298 (2001).
75. R. J. Jouet, A. D. Warren, D. M. Rosenberg, V. J. Bellitto, K. Park and M. R. Zachariah, *Chemistry of Materials* **17** (11), 2987-2996 (2005).
76. B. McCool, L. Murphy and C. P. Tripp, *Journal of Colloid and Interface Science* **295** (1), 294-298 (2006).
77. G. Z. Cao, J. Meijerink, H. W. Brinkman and A. J. Burggraaf, *Journal of Membrane Science* **83** (2), 221-235 (1993).
78. W. E. Moerner, *Journal of Physical Chemistry B* **106**, 910-927 (2002).
79. S. A. Weiss, *Science* **283**, 1676-1683 (1999).
80. Y. Jung, E. Barkai and R. J. Silbey, *The Journal of Chemical Physics* **117** (24), 10980-10995 (2002).
81. I. J. Tinoco and C. Bustamante, *Biophysical Chemistry* **101** (1), 512-533 (2002).
82. A. M. van Oijen, *Science* **301**, 1235-1238 (2003).
83. M. D. Mason, K. Ray, R. D. Grober, G. Pohlers and J. F. Cameron, *Physical Review Letters* **93** (7) (2004).
84. C. R. Viteri, J. W. Gilliland and W. T. Yip, *Journal of the American Chemical Society* **125** (7), 1980-1987 (2003).
85. J. R. Lakowicz, (Springer Science, 2006).
86. D. A. Skoog, S. R. Crouch and F. J. Holler, *Principles of Instrumental Analysis*, 6th ed. (Cengage Learning, Inc, CA, 2006).

87. K. Drexhage, in *Dye Lasers*, edited by F. Schäfer (Springer Berlin / Heidelberg, 1973), Vol. 1, pp. 155-200.
88. Invitrogen, in *Fluorescence Tutorials*: (2010), Vol. 2010.
89. M. Kasha, *Discussions of the Faraday Society* **9**, 14-19 (1950).
90. G. G. Stokes, *Phil Trans R Soc (London)* **142** (1852).
91. Y. Hiraoka, J. R. Swedlow, M. R. Paddy, D. A. Agard and J. W. Sedat, *Seminars In Cell Biology* **2** (3), 153-165 (1991).
92. J. S. A. Minden, D.A.; Sedat, J.W.; Alberts, B.M., *J Cell Biol* **109**, 505-516 (1989).
93. Y. M. Hiraoka, J.S.; Swedlow, J.R., Sedat, J.W.; Agard, D.A., *Nature* **342**, 293-296 (1989).
94. W. M. Sullivan, J.S.; Alberts, B.M., *Development* **110**, 311-323 (1990).
95. L. Wegley, P. Mosier-Boss, S. Lieberman, J. Andrews, A. Graff-Baker and F. Rohwer, *Environmental Microbiology* **8** (10), 1775-1782 (2006).
96. J. A. F. Rachel T. Noble, *Aquat Microb Ecol* **14**, 113-118 (1998).
97. E. Abbe, *Journal of the Royal Microscopical Society* **23** (1), 23 (1883).
98. T. R. Corle and G. S. Kino, in *Confocal Scanning Optical Microscopy and Related Imaging Systems* (Academic Press, Burlington, 1996), pp. 1-66.
99. A. Ekani-Nkodo and D. K. Fygenson, *Physical Review E* **67** (2), 021909 (2003).
100. J. R. Lawrence, G. M. Wolfaardt and D. R. Korber, *Appl. Environ. Microbiol.* **60** (4), 1166-1173 (1994).
101. J. D. Fowlkes, B. L. Fletcher, S. T. Retterer, A. V. Melechko, M. L. Simpson and M. J. Doktycz, *Nanotechnology* **19** (41), 415301 (415312 pp.) (2008).

102. A. L. Doadrio, E. M. B. Sousa, J. C. Doadrio, J. Perez Pariente, I. Izquierdo-Barba and M. Vallet-Regi, *Journal of Controlled Release* **97** (1), 125-132 (2004).
103. C. Boissiere, M. U. Martines, A. Larbot and E. Prouzet, *Journal of Membrane Science* **251** (1-2), 17-28 (2005).
104. D. M. Ford, E. E. Simanek and D. F. Shantz, *Nanotechnology* **16** (7), 458-475 (2005).
105. K. Kuraoka, N. Kubo and T. Yazawa, 10th International Workshop on Glass and Ceramics, Hybrids and Nanocomposites from Gels, Sep 20-Sep 24 1999  
*Journal of Sol-Gel Science and Technology* **19** (1-3), 515-518 (2000).
106. R. Krishna and R. Baur, *Chemical Engineering Journal* **97** (1), 37-45 (2004).
107. R. Krishna, *Gas Separation & Purification* **7** (2), 91-104 (1993).
108. T. Q. Gardner, J. L. Falconer and R. D. Noble, *Desalination* **149** (1-3), 435-440 (2002).
109. T. Q. Gardner, J. L. Falconer, R. D. Noble and M. M. P. Zieverink, *Chemical Engineering Science* **58** (10), 2103-2112 (2003).
110. F. P. Cuperus, D. Bargeman and C. A. Smolders, Sixth International Symposium on Synthetic Membranes in Science and Industry, Sep 4-8 1989  
*Journal of Membrane Science* **61**, 73-83 (1991).
111. S. R. Chowdhury, R. Schmuhl, K. Keizer, J. E. Ten Elshof and D. H. A. Blank, *Journal of Membrane Science* **225** (1-2), 177-186 (2003).
112. E. Betzig, J. K. Trautman, T. D. Harris, J. S. Weiner and R. L. Kostelak, *Science* **251** (1991), 1468-1471 (1991).
113. W. P. Ambrose and W. E. Moerner, *Nature* **349** (6306), 225-227 (1991).
114. S. Higgins, R. Kennard, N. Hill, J. DiCarlo and W. J. DeSisto, *Journal of Membrane Science* **279** (1-2), 669-674 (2006).

115. C. Hellriegel, J. Kirstein, C. Brauchle, V. Latour, T. Pigot, R. Olivier, S. Lacombe, R. Brown, V. Guieu, C. Payrastra, A. Izquierdo and P. Mocho, *Journal of Physical Chemistry B* **108** (38), 14699-14709 (2004).
116. K. S. McCain, D. C. Hanley and J. M. Harris, *Analytical Chemistry* **75** (17), 4351-4359 (2003).
117. F. P. Cuperus, D. Bargeman and C. A. Smolders, *Journal of Membrane Science* **71** (1-2), 57-67 (1992).
118. C.-Y. Wei, Y. H. Kim, R. K. Darst, P. J. Rossky and D. A. Vanden Bout, *Physical Review Letters* **69**, 173001 (2005).
119. J. T. Fourkas, *Optics Letters* **26** (4), 211-213 (2001).
120. S. R. Inamdar, J. R. Mannekutla, B. G. Mulimani and M. I. Savadatti, *Chemical Physics Letters* **429**, 141-146 (2006).
121. R. S. Moog, M. D. Edlger, S. G. Boxer and M. D. Fayer, *The Journal of Chemical Physics* **86** (24), 4694-4700 (1982).
122. G. B. Dutt and G. Rama Krishna, *Journal of Chemical Physics* **115** (10), 4732-4741 (2001).
123. X. S. Xie and R. C. Dunn, *Science* **265** (1994).
124. J. F. C. Kingman, *Poisson Processes (Oxford Studies in Probability)*. (Oxford University Press, USA), 1993).
125. W. E. Moerner and D. Fromm, P., *Review of Scientific Instruments* **74** (8), 3597-3619 (2003).
126. *NIST/SEMATECH e-Handbook of Statistical Methods*, <http://www.itl.nist.gov/div898/handbook/>, 6/23/2010.
127. T. E. Clark, H. W. Deckman, D. M. Cox and R. R. Chance, *Journal of Membrane Science* **230** (1-2), 91-98 (2004).

128. P. Huang, N. Xu, J. Shi and Y. S. Lin, *Journal of Membrane Science* **116** (2), 301-305 (1996).
129. T. Tsuru, T. Hino, T. Yoshioka and M. Asaeda, *Journal of Membrane Science* **186** (2), 257-265 (2001).
130. C. W. Chu, D. P. Kirby and P. D. Murphy, *Journal of Adhesion Science and Technology* **7** (5), 417-433 (1993).
131. P. Van Der Voort and E. E. Vansant, *Polish Journal of Chemistry* **71** (5), 550 (1997).
132. B. Fubini, V. Bolis, A. Cavenago, E. Garrone and P. Ugliengo, *Langmuir* **9** (10), 2712-2720 (1993).
133. M. L. Hair and W. Hertl, *Journal of Physical Chemistry* **73** (12), 4269-4276 (1969).
134. S. Judd and B. Jefferson, *Filtration and Separation* **40** (7), 38-40 (2003).
135. S. B. Lee, D. T. Mitchell, L. Trofin, T. K. Nevanen, H. S  nderlund and C. R. Martin, *Science* **296** (5576), 2198-2200 (2002).
136. S. Kipke and G. Schmid, *Advanced Functional Materials* **14** (12), 1184-1188 (2004).
137. D. Gong, V. Yadavalli, M. Paulose, M. Pishko and C. A. Grimes, *Biomedical Microdevices* **5** (1), 75-80 (2003).
138. J. Andersson, J. Rosenholm, S. Areva and M. Linden, *Chemistry of Materials* **16** (21), 4160-4167 (2004).
139. *Membrane Formation and Modification*. (American Chemical Society, 1999).
140. S. Che, K. Lund, T. Tatsumi, S. Iijima, S. H. Joo, R. Ryoo and O. Terasaki, *Angewandte Chemie International Edition* **42** (19), 2182-2185 (2003).
141. S. Che, Z. Liu, T. Ohsuna, K. Sakamoto, O. Terasaki and T. Tatsumi, *Nature* **429** (6989), 281-284 (2004).

142. R. Erni, M. D. Rossell, C. Kisielowski and U. Dahmen, *Physical Review Letters* **102** (9), 096101 (2009).
143. R. Kennard, W. J. DeSisto, T. P. Giririjan and M. D. Mason, Submitted to *The Journal of Chemical Physics* (2007).
144. H. Matsui, S. H. Randell, S. W. Peretti, C. W. Davis and R. C. Boucher, *The Journal of Clinical Investigation* **102** (6), 1125-1131 (1998).
145. J. C. Ritland Politz, R. A. Tuft and T. Pederson, *Mol. Biol. Cell* **14** (12), 4805-4812 (2003).
146. S. Serowy, S. M. Saparov, Y. N. Antonenko, W. Kozlovsky, V. Hagen and P. Pohl, *Biophysical journal* **84** (2), 1031-1037 (2003).
147. P. Xia, P. M. Bungay, C. C. Gibson, O. N. Kovbasnjuk and K. R. Spring, *Biophysical journal* **74** (6), 3302-3312 (1998).
148. W. S. Rasband, edited by U. S. N. I. o. Health (Bethesda, Maryland, USA, 1997-2011).
149. D. M. Soumpasis, *Biophysical Journal* **41** (1), 95-97 (1983).
150. R. Swaminathan, C. P. Hoang and A. S. Verkman, *Biophysical Journal* **72** (4), 1900-1907 (1997).
151. D. Gong, V. Yadavilla, M. Paulose, M. Pishko and C. A. Grimes, *Biomedical Microdevices* **5** (1), 75-80 (2003).
152. X. Jiang, N. Mishra, J. N. Turner and M. G. Spencer, *Microfluid Nanofluid* **5**, 695-701 (2008).
153. B. Wolfrum, Y. Mourzina, F. Sommerhage and A. Offenhausser, *Nano Letters* **6** (3), 453-457 (2006).
154. B. B. Lakshmi and C. R. Martin, *Nature* **388**, 758-760 (1997).
155. S. B. Lee, D. T. Mitchell, L. Trofin, T. K. Nevanen, H. Soderlund and C. R. Martin, *Science* **296**, 2198-2200 (2002).

156. I. Vlassiouk, A. Krasnoslobodtsev, S. Smirnov and M. Germann, *Langmuir* **20**, 9913-9915 (2004).
157. S. K. Dalvie and R. E. Baltus, *Journal of Membrane Science* **71** (3), 247-255 (1992).
158. X. Jiang, N. Mishra, J. N. Turner and M. G. Spencer, *Microfluidics and Nanofluidics* **5** (5), 695-701 (2008).
159. A. Ekani-Nkodo and D. K. Fygenson, *Physical Review E* **67**, 021909(021901)-021909(021907) (2003).
160. J. D. Fowlkes, E. D. Hullander, B. L. Fletcher, S. T. Retterer, A. V. Melechko, D. K. Hensley, M. L. Simpson and M. J. Doktycz, *Nanotechnology* **17**, 5659-5668 (2006).
161. J. R. Lawrence, G. M. Wolfaardt and D. R. Korber, *Applied and Environmental Microbiology* **60** (4), 1166-1173 (1994).
162. E. A. J. Reits and J. J. Neefjes, *Nature Cell Biology* **3**, E145-E147 (2001).
163. J. Kirstein, B. Platschek, C. Jung, R. Brown, T. Bein and C. Brauchle, *Nature Materials* **6**, 303 (2007).
164. D. A. Higgins, D. A. Vanden Bout, J. Kerimo and P. F. Barbara, *Journal of Physical Chemistry* **100** (32), 13794-13803 (1996).
165. Y. Song, M. Srinivasasao, A. Tonelli, C. M. Balik and R. McGregor, *Macromolecules* **33**, 4478 (2000).
166. J. P. Brunelle, P. G. P. J. B. Delmon and G. Poncelet, in *Studies in Surface Science and Catalysis* (Elsevier, 1979), Vol. Volume 3, pp. 211-232.
167. B. H. Winkler and R. E. Baltus, *Journal of Membrane Science* **226** (1-2), 75-84 (2003).
168. J. A. Yopps and D. W. Fuerstenau, *Journal of Colloid Science* **19** (1), 61-71 (1964).
169. L. D. Lavis, T. J. Rutkoski and R. T. Raines, *Analytical Chemistry* **79** (17), 6775-6782 (2007).



170. R. Kennard, W. J. DeSisto and M. D. Mason, *Applied Physics Letters* **97** (21), 213701-213703 (2010).
171. J. Crank, *The Mathematics of Diffusion*, 2nd ed. (Oxford University Press, Bristol, 1975).
172. B. S. Berland, I. P. Gartland, A. W. Ott and S. M. George, *Chemistry of Materials* **10** (12), 3941-3950 (1998).
173. R. A. Adomaitis, *Journal of Crystal Growth* **312** (8), 1449-1452.
174. J. Gutenwik, B. Nilsson and A. Axelsson, *Journal of Chromatography A* **1048** (2), 161-172 (2004).
175. H. Brenner and L. J. Gaydos, *Journal of Colloid and Interface Science* **58** (2), 312-356 (1977).
176. J. E. Crowell, J. G. Chen and J. T. Yates, *Journal of Chemical Physics* **85** (5), 3111 (1986).
177. L. R. Snyder, *Journal of Chromatography A* **23**, 388-402 (1966).
178. D. Cassidy, S. Higgins, B. A. McCool and W. J. DeSisto, *ECS Transactions* **16** (4), 151-157 (2008).
179. R. M. Barrer, *Diffusion in and through solids*, 4th ed. (The University Press, 1951).
180. H. L. Frisch, *The Journal of Physical Chemistry* **61** (1), 93-95 (1957).
181. H. L. Frisch, *The Journal of Physical Chemistry* **62** (4), 401-404 (1958).
182. M. Wojcik, *Nuclear Instruments and Methods in Physics Research Section B: Beam Interactions with Materials and Atoms* **61** (1), 8-11 (1991).
183. Y. V. Sytyi, B. I. Molchanov, M. M. Gudimov, Y. V. Zherdev, A. I. Soshko, E. S. Golovastov, A. N. Tynnyi and N. G. Kalinin, *Materials Science* **7** (4), 457-458 (1974).
184. T. Z. Xu, J.Z.; Cheng, J. M.; Dang, H. X.; , j. *Trace Microprobe Tech.* **15** (1997).

185. G. E. Thompson and G. C. Wood, *Nature* **290** (5803), 230-232 (1981).
186. J. P. O'Sullivan and G. C. Wood, *Proceedings of the Royal Society of London. A. Mathematical and Physical Sciences* **317** (1531), 511-543 (1970).
187. G. Xiong, J. W. Elam, H. Feng, C. Y. Han, H. H. Wang, L. E. Iton, L. A. Curtiss, M. J. Pellin, M. Kung, H. Kung and P. C. Stair, *Journal of Physical Chemistry B* **109** (29), 14059-14063 (2005).

## APPENDICES

### Appendix A: Patent Application

System and method for Determining Transport properties of solutes in a liquid

STATEMENT REGARDING FEDERALLY SPONSORED RESEARCH OR

DEVELOPMENT

Invention was developed with funds received from NSF CAREER Grant No. 0457103.

#### BACKGROUND OF THE INVENTION

This invention relates in general to time-dependent measurement of the concentration of a molecule diffusing through a porous medium and in particular to measurement of a time-resolved concentration of a fluorescent molecule diffusing through a porous membrane.

The time-dependent measurement of the concentration of a molecule diffusing through a porous medium provides fundamental information for the design of separation and transport systems/devices. In the case of solute diffusion, practical applications include drug delivery cell growth via controlled nutrient delivery and molecular separations. Recently developed optical methods, such as Fluorescence Recovery After Photo-bleaching (FRAP), have been successfully applied to measure the diffusivity in a variety of material systems including bio-films, fibers and membranes. In FRAP, the fluorophore is photo-bleached in a known area, and the time-dependent migration of non-bleached fluorophores is measured. Unfortunately, with this technique, it is difficult to ensure concentration-driven diffusion is observed because the photo-bleached molecules remain within the volume of interest. More recently, single-molecule imaging techniques have been applied to study diffusive transport through membranes, providing a highly sensitive, spatially correlated picture of molecular movement through porous media.

Owing to the low signal levels present specific and often very costly instrumentation is required. Strict sample preparations are mandated, and significant limitations on sample type and geometry exist for single-molecule imaging techniques. Accordingly, a simpler measurement method and system would be desirable.

#### SUMMARY OF THE INVENTION

This invention relates to measurement of a time-resolved concentration of a fluorescent molecule diffusing through a porous membrane.

The present invention contemplates a system for measuring the diffusion profile of a fluorescent molecule that includes an inorganic membrane disc having opposite first and second parallel surfaces. The system also includes an O-ring disposed about the circumference of the first surface of the disc with a volume of fluorescein disposed within the O-ring and upon the first disc surface. The system further includes a supporting surface disposed adjacent to the second disc surface and a device for measuring the diffusion of fluorescein molecules through the membrane disc.

The present invention also contemplates a method for measuring the diffusion profile of a fluorescent molecule that includes providing an inorganic membrane disc having opposite first and second parallel surfaces, the membrane having an O-ring disposed about the circumference of the first disc surface. The method also includes disposing a volume of fluorescein within the O-ring and upon the first disc surface and placing a sample volume of a material to be measured between a supporting surface and the second disc surface. Additionally, the method includes measuring the diffusion of all suitable fluorescent molecules, such as fluorescein, or semiconductor quantum dots, such as CdSe, through the membrane disc. In the preferred embodiment, the method utilizes an inverted laser microscope and a charge coupled device camera within an integrated system for the diffusion measurement.

Various objects and advantages of this invention will become apparent to those skilled in the art from the following detailed description of the preferred embodiment, when read in light of the accompanying drawings.

#### BRIEF DISCRPTION OF THE DRAWINGS

(The drawings referenced here are found in the main body of the thesis in the chapter 8.)

Figure 8.2 is a diagram of a system for collection of data for fluorescent molecules diffusing through selected membranes in accordance with the present invention.

Figure 8.5 is an enlarged portion of the diagram shown in Figure 8.2

Figure 8.6 is a graph illustrating raw data obtained for a sample with the system shown in Figure 8.2.

Figure 8.7 is a graph illustrating the breakthrough curve for the alumina membrane utilized in the system shown in Figure 8.2 as determined from the averaging of the data shown in Figure 8.6.

#### DETAILED DISCRPTION OF THE PREFERRED EMBODIMENT

The present invention is directed toward a simple method for measuring the time-resolved concentration of fluorescent molecules diffusing through an anodic alumina membrane with a pore diameter of 20 nm. From a concentration breakthrough curve, a molecular diffusivity of the fluor can be extracted that is three orders-of-magnitude lower than reported bulk values. This method can be applied to provide fundamental information for bio-molecular separations applications. One feature of the present invention is the high sensitivity at inter-cellular volumes, which broadens its application to drug delivery and controlled cell growth.

The present invention utilizes an integrated system designed to measure the time-dependent concentration changes of molecules in solution diffusing through porous media. The present invention is relatively simple, robust, and inexpensive relative to optical systems and is based on the optical detection of fluorescent molecules. The present invention contemplates an integrated system that enables, for the first time, measurement of molecular diffusivities within volumes about

10 to 100 biological cells, thereby scaling the measurement to many relevant biotechnology applications, including drug delivery and artificial cell growth. The present invention also allows, through measurement, the determination of relevant design parameters for sizing membrane units for separating molecular components in solution. Measurement of these parameters in solution has previously proven challenging due to the complexity of interactions between the molecule and membrane. It is envisioned that this technology can be applied to assessing the ability of membranes to achieve desired separations in the pharmaceutical industry for example, where molecular separations are often quite challenging (for example enantiometric separations).

Referring now to the drawings, there is illustrated in Figure 8.2 a diagram of a measuring system 10 that is accordance with the present invention. The system 10 includes a measurement cell 12, optical bench 14, and associated software. The measurement cell 12 utilizes a commercial (Anopore, Whatman) membrane with a highly uniform pore size distribution. The measurement cell 12 can be configured in co-current, cross or counter-current flow; arrangements used in industrial membranes. Time-dependent measurements of molecule concentration are made providing data that can, when appropriately modeled, provide parameters that will enable the design of drug delivery systems (small scale) to separation processes (large scale). The optical bench 14 is comprised of a system designed for measuring the concentration of fluorescent molecules within the measurement cell 12. The system hardware is coupled to a computer control system 16 that enables the measurement and quantifies the output of concentration over time.

The unique aspects of the system 10 include the continuous monitoring a change photon emission representative of a change in atto moles of fluorescent molecules (13000 molecules) in a volume estimated to be 10 pL, a volume on the order of 100 cells. These values can be lowered by simple modifications to fluorescent doping procedures and physically reducing the size of the frit. Although current technology has achieved stochastic measurement of single molecule measurement of enzymatic assays, this method not only allows for these measurements, but the system can easily measure the kinetics of single and multicomponent enzyme pathways by the

utilization of multiple excitation wavelengths. The system 10 is able to take these measurements to a more inclusive level by starting at a feed rate about single molecule level and slowly increasing the feed rate to encompass the ability of both single molecule stochastic measurements and bulk time-dependent measurements.

All fluorescence data is collected in a custom-built, Inverted Olympus IX71 Laser Microscope (IVLM) 20. Uniform far field kohral illumination of the constructed sample and excitation of fluorescent molecules is accomplished by the output of a solid-state diode laser 22. The laser 22 generates an excitation beam 23 that is directed through a calibrated, round, continuously variable, metallic, and neutral-density filter wheel 24 that controls the excitation intensity of the laser beam. A beam sampler 26 is located after the neutral-density filter wheel 24 and is operative to direct a continuous beam sample to a power meter 28, such as a commercially available Thorlabs Power Meter. The power meter 28, which is connected to the computer control system 16, is utilized to quantify fluctuations in the emission signal by monitoring the excitation power in the laser beam 23. The power meter 28 is integrated with the entire system 10 by a software package within the computer control system 16. The remainder of the excitation incident beam 23 is passed through a Galilean beam expander 30. The resulting parallel expanded beam is then directed through a focusing optic 32 with the focal length to match the distance to the back of a high NA oil emersion objective 34. The beam also passes through a dichroic beam splitting cube 36 that is positioned between the focusing optic 32 and the oil emersion objective 34. The excitation beam 23 is then focused into the void volume created in the constructed sample. As the fluorescent molecules diffuse into the void volume, they become excited and emit a signal with the emission collected back through high NA objective 34 and the cube beam splitter 36 onto to a Charge Coupled Device (CCD) camera 38 that is connected to the computer control system 16. The camera settings 38 are chosen to maximize the CCD dynamic range and reduce the camera read. The camera 38 and power meter 28 are run simultaneously

and continuously for a desired time frame in a controlled and integrated manner with software in the computer control system 16 in order to obtain the sufficient data.

Details of the well sample 12 are shown in Figure 8.5 where an O-ring 40 is sealed to a porous inorganic membrane 42 with a mounting medium. In the preferred embodiment, an anodic alumina membrane with a pore diameter of 20 nm, such as an Anopore disc, is utilized for the porous membrane 42. A sample volume 44 to be monitored is disposed between the membrane 42 and a microscope cover glass 46. The well sample 12 is loaded with 200  $\mu\text{L}$  aliquots of fluorescein 48 with a concentration within a range of 170 to 340 nL. A cover 50 is placed over the sample to prevent drying. This configuration generates a fritted volume of 150 nL (surface area of  $1 \text{ cm}^2$ , depth of 1.5  $\mu\text{m}$ ). Taking into account the surface area monitored by the microscope system ( $5900 \mu\text{m}^2$ ) due to the magnification; the volume that is continuously measured is =10 pL. This volume is approximately 100 cells, assuming approximately 100fL per cell. By physically reducing the surface area by sealing the outer perimeter with the mounting medium, these dimensions can easily be reduced by two orders of magnitude. The unique and novel application of the Anopore disc takes advantage of slowing the transport kinetics of a target fluorescent tag. By adding nanomolar concentrations of a fluorescent tag to the exterior of the fritted vessel, i.e., on the top of the porous disc, and continuously monitoring the total change of the fluorescent signal over time, a response in intensity is recorded that is representative of atto moles (13000 molecules) in 15 sec. This results in transient measurement of dye concentration in the fitted volume.

#### EXAMPLE

The inventors utilized the system 10 to study the transport of fluorescein through a commercial anodic alumina porous disc (Anodisc<sup>TM</sup>). These membranes are characterized by a high pore density ( $10^9$  pores/ $\text{m}^2$ ), uniform pore size (range 20-200nm), and straight channel pores (tortuosity,  $\tau = 1$ ). In their study, the inventors used anodic alumina membranes with a total diameter of 13 mm, mean pore diameter of 20 nm, thickness of 60  $\mu\text{m}$  and porosity of 25 to 50%.



The system 10 illustrated in Figure 8.2 was used to collect breakthrough data for diffusion of fluorescein molecules through anodic alumina porous membranes. The system geometry allowed for concentration driven solution diffusion from a large bulk volume into a vessel of approximately 150 nL. Prior to sealing in the measurement cell 12, the membranes 42 were soaked in bleached nanopure water for 24 hrs to ensure pore filling. To load the cell, 200  $\mu$ L aliquots of fluorescein at concentrations of 170 and 340 nL were added to the top side of the prepared sample.

Fluorescence was recorded using an inverted laser microscope (Olympus IX71) 20 and a CCD camera 38. Images were recorded at 4 different excitation energies, namely,  $\approx 0.4$  mW,  $\approx 0.8$  mW,  $\approx 1.9$  mW, and  $\approx 3.0$  mW) and two different fluorescein concentrations (170nm and 340nm) for exposures of 200ms with a 15.3 second delay between each image acquisition. Measurements at different incident power levels eliminated effects of instrumentation on the resulting breakthrough curves. The camera and power meter were run simultaneously and continuously for 155 minutes (600 images), until steady state intensity was reached, indicating no further change in fluorescein concentration. The raw collected data is shown in Figure 8.5 for the four different excitation energies and includes photo-bleaching effects.

The system 10 shown in Figure 8.2 was modeled by applying a mass balance to across the membrane 42. For a membrane with a porosity  $\epsilon$  and cross-sectional area A the balance is:

$$V_i [dC_i/dt] = J \epsilon A$$

where  $V_i$  is the collection volume at the exit of the membrane;  $C_i$  is the concentration; and J is the flux leaving the membrane.

The flux in the membrane can be expressed by Fick's first equation:

$$J = (D/\tau_r) / (dC/dx) \quad (\text{Eq. 1});$$

where D is the diffusivity and  $\tau_r$  the tortuosity of the pore network. Integrating the flux over the membrane thickness,  $e$  and the bulk concentration,  $C_o$  to  $C_i$  and solving Eq. 1, yields a model for

transport through the membrane:

$$C_i(t)/C_0 = 1 - \exp[-(\varepsilon DA / \tau_r V_i) t] \quad (\text{Eq. 2}).$$

In addition to transport, photo bleaching of the molecules must be accounted for as described by equation 4 that is shown below. The photo-bleaching is described by the following equation :

$$I(t) = I_0 \Phi_{\text{ext}} C_i [ A_0 \exp[-(t/\tau) \beta] + y_0 ] \quad (\text{Eq. 3})$$

where,  $I(t)$ , the emission intensity observed at time  $t$ , is the product of excitation energy;  $I_0$ , the external scalar of the system,  $\Phi_{\text{ext}}$ ; the concentration of the fluorescent species,  $C_z$ .  $A_0$  is the molecular fluorescent efficiency;  $\tau$  is of the molecule lifetime;  $\beta$  is a fitting parameter for the stretched exponential that ideally is 1; and  $y_0$  is the background fluorescent efficiency of the system.

The extent of bleaching,  $EB(t)$ , in the invention's continuous system is:

$$EB(t) = I(t)/I(0) \quad (\text{Eq. 4.})$$

The final expression for transport including photo-bleaching effects is then given as:

$$I(t) = I_0 \Phi_{\text{ext}} C(t) EB(t) \quad (\text{Eq. 5}).$$

The raw data shown in Figure 8.6 were fitted to the model above. The defined parameters were  $I_0$ , the excitation energy used to produce the raw data and  $C_0$ , the loading concentration of fluorescein. The shared, undefined parameters between all experiments were  $\Phi_{\text{ext}}$ , the excitation efficiency of the system,  $D$ , the effective diffusion constant,  $\tau$ , and  $\beta$ . The parameters allowed to freely flow for each data set were  $\varepsilon$ , the porosity of the alumina membranes, bounded by 20% to 50%;  $A$ , the area accessible to the fluorescent molecules,  $l$ , the thickness of the disc,  $V_i$ , the volume between the alumina membrane 42 and glass slide 46 shown in Figure 8.5; and,  $y_0$  and  $A_0$ , the mathematical representation of the background fluorescent signal. Figure 8.7 shows the breakthrough curve for the alumina membrane determined from the averaging of the data shown in Figure 8.6 for each initial concentration of fluorescein. The breakthrough curve is similar to data obtained from molecules diffusing from porous media.

The diffusivity of fluorescein determined from the data and model in anodic alumina membranes was  $1.0 \times 10^{-9} \text{ cm}^2 \text{ s}^{-1}$ ; which is considerably slower than the bulk diffusivity measured in pure water ( $5.6 \times 10^{-6} \text{ cm}^2 \text{ s}^{-1}$ ). The results compare favorably to prior art measurements of diffusivities of caffeine, methyl orange and malachite green oxalate through 40nm porous anodic alumina membranes. In addition, the results compare to diffusivity of fluorescein previously measured by FRAP in collagen fibrils with an estimated interstices of 1.6 nm ( $D = 1 \times 10^{-10} \text{ cm}^2 \text{ s}^{-1}$ ), nylon 66 ( $D = 6.9 \times 10^{-11} \text{ cm}^2 \text{ s}^{-1}$ ) and biofilms ( $D = 7.7 \times 10^{-8} \text{ cm}^2 \text{ s}^{-1}$ ). Furthermore, previous measurements of diffusivity of fluorescein isothiocyanate through a carbon nanofiber membrane using FRAP ( $D = 7.5 \times 10^{-7} \text{ cm}^2 \text{ s}^{-1}$ ) compare with the results obtained by the inventors. The decrease in diffusivity of fluorescein in the alumina membranes could result from either size effects or surface effects. The hydrodynamic radius of fluorescein have been estimated at 0.4nm, smaller than the pore diameter of 20 nm that was utilized in the example, yet still close enough to the pore diameter to have significant interaction with the pore walls. Since the isoelectric point of  $\alpha$ -alumina is 9<sup>166</sup> and 7 to 9 for other forms<sup>168</sup>, membranes in the inventor's experiments had a positive surface charge. This could also play a role in decreasing diffusivity relative to bulk diffusivity.

The present invention would be of interest to a wide variety of businesses. Companies that manufacture membranes, for example, can use this technology to develop new membranes and more completely characterize their existing membranes. Information they obtain would be valuable to their customers and enhance their products. Companies that develop drug delivery modules would be interested in this technology to quantify their modules performance. Companies that are developing technology for artificial cell growth would also be interested in order to quantify platforms used for cell growth (i.e. nutrient delivery control to cells). Companies that sell integrated optical systems would be interested in adding a new product to their inventory.

The uniqueness of the present invention is that it lies in between single molecule imaging and larger volume bulk measurements of solute molecules, resulting in novel applications. The system 10 described above is robust and simple to construct. The system 10 allows for the time-dependent bulk measurement of solute molecules in volumes approaching  $10^2$  to  $10^3$  biological cells, a scale that is appropriate for mimicking transport in biological systems. The system also allows a method for measuring the effects of pore geometry and pore surface chemistry on parameters necessary for the design of separation operations; for example, the direct determination of separation factors, permeance, and diffusivity of solutes through porous media. Fundamental properties of solute diffusion in liquid systems have been traditionally difficult to measure. The system can take measurements in co-current, cross-flow, and counter-current geometries to simulate industrial membrane systems.

By taking advantage of commercially available porous membranes with very narrow pore size distributions, a fitted vessel with volumes in the range of pico-liters to micro-liters can be constructed to accommodate different flow cell geometries. Fluorescent molecules moving through the cell can then be studied with a custom built inverted laser microscope. The capabilities of the present invention allow one to measure dynamics in a fluid based system that has yet to be probed. Taking advantage of the correct dosing of a fluorescent tag and the transport restriction and regulation of these fluorescent-tagged materials due to the porous membrane, various systems can be directly and indirectly measured (including but not limited to fluid dynamics of a single or multiple solute(s) under a pressure or concentration gradient, enzyme kinetics, etc.). These physical and chemical properties of the pores within the specific fritted vessels can be further tuned to encompass larger dynamic ranges for cutoff, surface affects and transport control by utilizing developed chemistry to slowly and accurately grow new layers on the interior of fit.

The present invention has the unique characteristics with the sensitivity of monitoring concentration changes analogous to consumption rates on the same magnitude of an enzyme. The system and method of operation has the potential to further the understanding of enzyme kinetics with applications including but not limited to bioinformatics, biotechnology, and bioreactors. Additionally, the present invention can provide the measurement of kinetics of dilute solutes through nanoporous structures, critical for design engineering in many emerging technologies including controlled molecular delivery and highly specific molecular separations (including but not limited by drug delivery, and isometric separations).

In conclusion, the present invention demonstrates a relatively simple fluorescence imaging method for measuring the time-resolved concentration profile of a fluorescent molecule diffusing through an inorganic membrane, such as an alumina membrane. The present invention avoids many limitations of single-molecule methods, but still provides femto-molar sensitivities at the inter-cellular volumetric scale. The integrated system allows for the imaging of highly dilute concentrations at inter-cellular volumes, applicable to many biological applications including drug delivery and controlled cell growth. In addition, the present invention provides a relatively simple method for determining fundamental information useful for designing separation systems. While not specifically addressed here, fluorescence imaging the sample area allows for direct correlation between measured diffusivities and local macroscopic morphology. In this way, defect areas can be measured separately (or excluded completely) during analysis providing additional information of membrane integrity.

In accordance with the provisions of the patent statutes, the principle and mode of operation of this invention have been explained and illustrated in its preferred embodiment. However, it must be understood that this invention may be practiced otherwise than as specifically explained and illustrated without departing from its spirit or scope.

What is claimed is:

1. An integrated system for measuring the diffusion profile of a fluorescent molecule, the system comprising:
  - an inorganic membrane disc having opposite first and second parallel surfaces;
  - an o-ring disposed about the circumference of said first surface of said disc;
  - a volume of fluorescein disposed within said o-ring and upon said first surface of said disc;
  - a supporting surface disposed adjacent to said second surface of said disc;
  - a sample volume of material to be measured disposed between said supporting surface and said second surface of said disc; and
  - a device for measuring the diffusion of fluorescein molecules through said membrane disc.
2. The system according to claim 1 wherein said disc is a porous anodic alumina membrane.
3. A method for measuring the diffusion profile of a fluorescent molecule, the method comprising the steps of:
  - (a) providing an inorganic membrane disc having opposite first and second parallel surfaces, the membrane having an o-ring disposed about the circumference of the first disc surface;
  - (b) disposing a volume of fluorescein within the o-ring and upon the first disc surface;
  - (c) placing a sample volume of a material to be measured between a supporting surface and the second disc surface; and
  - (d) measuring the diffusion of fluorescent molecules through the membrane disc.
4. The method according to claim 3 wherein measurement in step (d) utilizes an inverted laser microscope and a charge coupled device camera.

#### ABSTRACT OF THE DISCLOSURE

A system and a method for measuring the diffusion profile of fluorescent molecules through an inorganic membrane disc.

**Appendix B: Receipt of Patent Application**

1-52204



UNITED STATES PATENT AND TRADEMARK OFFICE

UNITED STATES DEPARTMENT OF COMMERCE  
United States Patent and Trademark Office  
Address: COMMISSIONER FOR PATENTS  
P.O. Box 1450  
Alexandria, Virginia 22313-1450  
www.uspto.gov

APPLICATION NUMBER	FILING or 371(c) DATE	GRP ART UNIT	FIL FEE REC'D	ATTY..DOCKET.NO	TOT CLAIMS	IND CLAIMS
61/372,593	08/11/2010		110	2010-0010		

DOCKETED  
By [Signature] File To [Signature]

CONFIRMATION NO. 7777

**FILING RECEIPT**

4859  
MACMILLAN SOBANSKI & TODD, LLC  
ONE MARITIME PLAZA FIFTH FLOOR  
720 WATER STREET  
TOLEDO, OH 43604-1619



Date Mailed: 08/23/2010

Receipt is acknowledged of this provisional patent application. It will not be examined for patentability and will become abandoned not later than twelve months after its filing date. Any correspondence concerning the application must include the following identification information: the U.S. APPLICATION NUMBER, FILING DATE, NAME OF APPLICANT, and TITLE OF INVENTION. Fees transmitted by check or draft are subject to collection. Please verify the accuracy of the data presented on this receipt. **If an error is noted on this Filing Receipt, please submit a written request for a Filing Receipt Correction. Please provide a copy of this Filing Receipt with the changes noted thereon. If you received a "Notice to File Missing Parts" for this application, please submit any corrections to this Filing Receipt with your reply to the Notice. When the USPTO processes the reply to the Notice, the USPTO will generate another Filing Receipt incorporating the requested corrections**

**Applicant(s)**

Raymond Kennard, Old Town, ME;  
William DeSisto, Orono, ME;  
Michael Mason, Orrington, ME;

**Power of Attorney:**

John Molnar--31914

**If Required, Foreign Filing License Granted: 08/19/2010**

The country code and number of your priority application, to be used for filing abroad under the Paris Convention, is **US 61/372,593**

**Projected Publication Date:** None, application is not eligible for pre-grant publication

**Non-Publication Request:** No

**Early Publication Request:** No

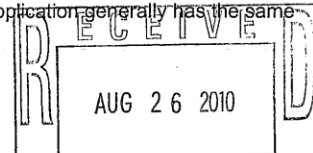
**\*\* SMALL ENTITY \*\***

**Title**

SYSTEM AND METHOD FOR DETERMINING TRANSPORT PROPERTIES OF SOLUTES IN A LIQUID

**PROTECTING YOUR INVENTION OUTSIDE THE UNITED STATES**

Since the rights granted by a U.S. patent extend only throughout the territory of the United States and have no effect in a foreign country, an inventor who wishes patent protection in another country must apply for a patent in a specific country or in regional patent offices. Applicants may wish to consider the filing of an international application under the Patent Cooperation Treaty (PCT). An international (PCT) application generally has the same



effect as a regular national patent application in each PCT-member country. The PCT process **simplifies** the filing of patent applications on the same invention in member countries, but **does not result** in a grant of "an international patent" and does not eliminate the need of applicants to file additional documents and fees in countries where patent protection is desired.

Almost every country has its own patent law, and a person desiring a patent in a particular country must make an application for patent in that country in accordance with its particular laws. Since the laws of many countries differ in various respects from the patent law of the United States, applicants are advised to seek guidance from specific foreign countries to ensure that patent rights are not lost prematurely.

Applicants also are advised that in the case of inventions made in the United States, the Director of the USPTO must issue a license before applicants can apply for a patent in a foreign country. The filing of a U.S. patent application serves as a request for a foreign filing license. The application's filing receipt contains further information and guidance as to the status of applicant's license for foreign filing.

Applicants may wish to consult the USPTO booklet, "General Information Concerning Patents" (specifically, the section entitled "Treaties and Foreign Patents") for more information on timeframes and deadlines for filing foreign patent applications. The guide is available either by contacting the USPTO Contact Center at 800-786-9199, or it can be viewed on the USPTO website at <http://www.uspto.gov/web/offices/pac/doc/general/index.html>.

For information on preventing theft of your intellectual property (patents, trademarks and copyrights), you may wish to consult the U.S. Government website, <http://www.stopfakes.gov>. Part of a Department of Commerce initiative, this website includes self-help "toolkits" giving innovators guidance on how to protect intellectual property in specific countries such as China, Korea and Mexico. For questions regarding patent enforcement issues, applicants may call the U.S. Government hotline at 1-866-999-HALT (1-866-999-4158).

**LICENSE FOR FOREIGN FILING UNDER  
Title 35, United States Code, Section 184  
Title 37, Code of Federal Regulations, 5.11 & 5.15**

**GRANTED**

The applicant has been granted a license under 35 U.S.C. 184, if the phrase "IF REQUIRED, FOREIGN FILING LICENSE GRANTED" followed by a date appears on this form. Such licenses are issued in all applications where the conditions for issuance of a license have been met, regardless of whether or not a license may be required as set forth in 37 CFR 5.15. The scope and limitations of this license are set forth in 37 CFR 5.15(a) unless an earlier license has been issued under 37 CFR 5.15(b). The license is subject to revocation upon written notification. The date indicated is the effective date of the license, unless an earlier license of similar scope has been granted under 37 CFR 5.13 or 5.14.

This license is to be retained by the licensee and may be used at any time on or after the effective date thereof unless it is revoked. This license is automatically transferred to any related applications(s) filed under 37 CFR 1.53(d). This license is not retroactive.

The grant of a license does not in any way lessen the responsibility of a licensee for the security of the subject matter as imposed by any Government contract or the provisions of existing laws relating to espionage and the national security or the export of technical data. Licensees should apprise themselves of current regulations especially with

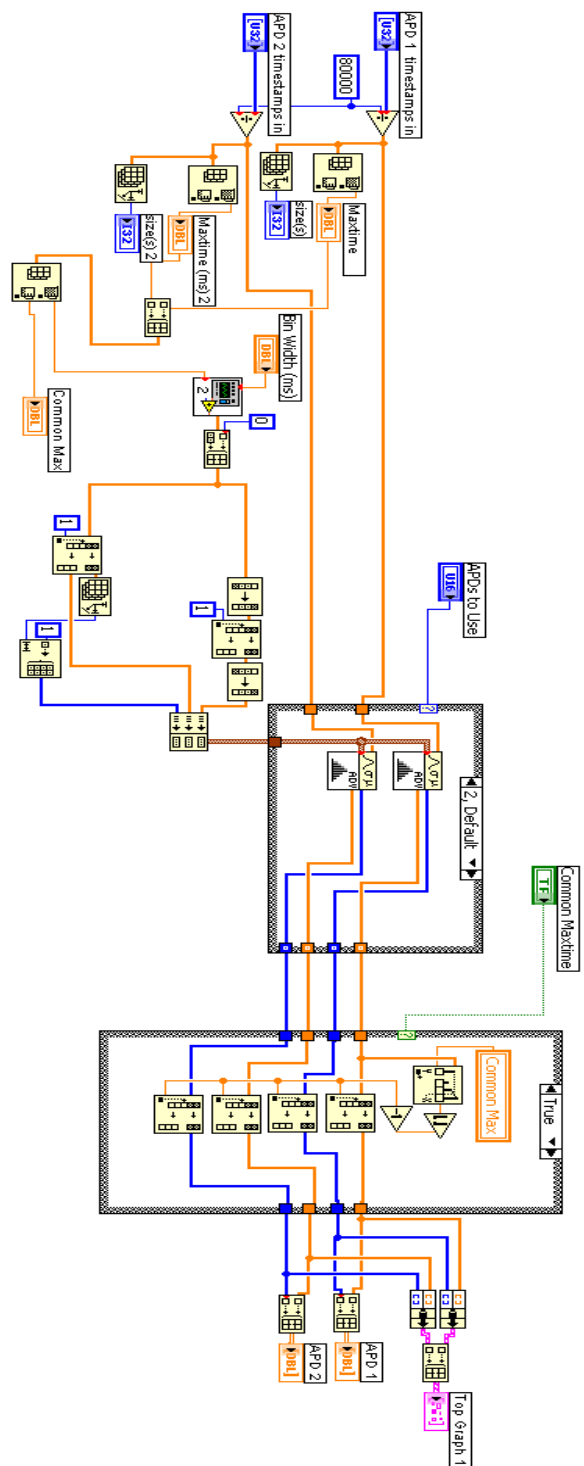


respect to certain countries, of other agencies, particularly the Office of Defense Trade Controls, Department of State (with respect to Arms, Munitions and Implements of War (22 CFR 121-128)); the Bureau of Industry and Security, Department of Commerce (15 CFR parts 730-774); the Office of Foreign Assets Control, Department of Treasury (31 CFR Parts 500+) and the Department of Energy.

**NOT GRANTED**

No license under 35 U.S.C. 184 has been granted at this time, if the phrase "IF REQUIRED, FOREIGN FILING LICENSE GRANTED" DOES NOT appear on this form. Applicant may still petition for a license under 37 CFR 5.12, if a license is desired before the expiration of 6 months from the filing date of the application. If 6 months has lapsed from the filing date of this application and the licensee has not received any indication of a secrecy order under 35 U.S.C. 181, the licensee may foreign file the application pursuant to 37 CFR 5.15(b).

## Appendix C: Labview Wiring Diagram



## Appendix D: Mathematica Code

### READING THE FILES

```
file: "C:\\Documents and Settings\\Raymond Kennard\\Desktop\\data\\10c intensity plot.dat";
Do[image$data: Transpose[Import[file], 1];
Dimensions[image$data]
ListDensityPlot[image$data, Mesh -> False, PlotRange -> {Automatic, Automatic, {0, 50}}, ColorFunction -> {Hue, .65, .85} &]
height$: Dimensions[image$data][1]
```

Calculating the threshold values

```
Dimensions[image$data][2];
total$N: Plus@@Table[Plus@@image$data[i], {i, 1, Dimensions[image$data][1]}];
mean$N: Dimensions[image$data][2];
i$data$N: image$data;
mean$N$A: 0;
u$N: 0;
u$N: Sqrt[Dimensions[image$data][2]];

While[Abs[mean$N - 2 u$N] > | mean$N$A - 2 u$N$A | > .001,
mean$N$A: mean$N;

u$N: Sqrt[mean$N$A];
i$data$N: i$data$N;
total$N: Plus@@Table[Plus@@i$data$N[i], {i, 1, Dimensions[i$data$N][1]}];
mean$N: Plus@@Table[i + Plus@@Transpose[i$data$N][i], {i, 1, Length[i$data$N][1]}] / total$N;
u$N: Sqrt[mean$N];
i$data$N: Transpose[Take[Transpose[i$data$N], Ceiling[mean$N - 2 u$N]]];

N$tave: mean$N
Nthres: | N$tave - 2 Sqrt[N$tave] | 4
Nthres$10c: | N$tave - 2 Sqrt[N$tave] |

NTH$Data: Table[Nthres, {i, 1000}, {i, 1000}];
LP$1: ListPlot[NTH$Data, Axes -> False]
```

## THE CALCULATION OF AVERAGE P AS A FUNCTION OF N

```

P$image$data: Transpose| image$data| ;
scale$: | 0, 1| | Dimensions| image$data| | 1| · 1| | ;
height$: Dimensions| image$data| | 1| ;

worki$$: | image$data| height$| + scale$| 1| , image$data| height$· 1| + scale$| 2| | ;
For| i: 2, i: Dimensions| image$data| | 1| · 1, i: | ;
  scale$: Append| scale$, | i· 1| | | height$· 1| | |

p$mean$: | 0| ;
For| i: 1, i: Dimensions| P$image$data| | 1| · 1, i: | ;
  p$sc$: scale$| P$image$data| i| ;

If| Total| P$image$data| i| | > 0,
  w$mean$: Plus| | p$sc$| Total| P$image$data| i| | ,
  w$mean$: 0| ;
  p$mean$: AppendTo| p$mean$, w$mean$| |

p$vari$: | 0| ;
p$std$: | 0| ;
For| i: 1, i: Dimensions| P$image$data| | 1| · 1, i: | ;
  p$sc$mean: p$mean$| i| + P$image$data| i| ;
  p$sc$: scale$· p$mean$| i| ;

If| Total| P$image$data| i| | > 0,
  w$vari$: Total| | | scale$· p$mean$| i| | 2 + P$image$data| i| | | / Total| P$image$data| i| | ;
  w$std$:  $\sqrt{w$vari$}$  ,
  w$vari$: 0;
  w$std$: 0| ;

p$vari$: AppendTo| p$vari$, w$vari$| ;
p$std$: AppendTo| p$std$, w$std$| |

neg$p$mean$: p$mean$· p$std$;
pos$p$mean$: p$mean$+ p$std$;

stat$mean: Table|  $\sqrt{i/ 100}$  , | i, 1, 27 000| | ;
Dimensions| P$image$data|

```

## FUNCTION FOR BINNING THE THRESHOLED VALUES OF AVERAGE P INTO A 1-D HISTOGRAM AND SAVING THE RESULTS AS TEXT FILES

```

Nt$binned$data: Table| Table| Plus|| Take| image$data| i| , | j, j+ 3| | , | j, 1, 268, 4| | , | i,
P$image$data: Transpose| Nt$binned$data| ;
scale$: | 0, 1| | Dimensions| Nt$binned$data| | 1| · 1| | ;
height$: Dimensions| Nt$binned$data| | 1| ;
worki$$: | Nt$binned$data| height$| + scale$| 1| , Nt$binned$data| height$· 1| + scale$| 2| | ;
For| i: 2, i| Dimensions| Nt$binned$data| | 1| · 1, i| + ;
  scale$: Append| scale$, | i· 1| | | height$· 1| | | ;
p$mean$: | 0| ;
For| i: 1, i| Dimensions| P$image$data| | 1| · 1, i| + ;
  p$sc$: scale$+ P$image$data| i| ;

If| Total| P$image$data| i| | > 0,
  w$mean$: Plus|| p$sc$| Total| P$image$data| i| | ,
  w$mean$: 0| ;
  p$mean$: AppendTo| p$mean$, w$mean$| |
p$mean$;
p$vari$: | 0| ;
p$std$: | 0| ;
For| i: 1, i| Dimensions| P$image$data| | 1| · 1, i| + ;
  p$sc$mean: p$mean$| i| + P$image$data| i| ;
  p$sc$: scale$· p$mean$| i| ;
  If| Total| P$image$data| i| | > 0,
    w$vari$: Total| | | scale$· p$mean$| i| | 2, P$image$data| i| | | Total| P$image$data| i| | ;
    w$std$:  $\sqrt{w$vari$}$  ,
    w$vari$: 0;
    w$std$: 0| ;
  p$vari$: AppendTo| p$vari$, w$vari$| ;
  p$std$: AppendTo| p$std$, w$std$| |

neg$p$mean$: p$mean$· p$std$;
pos$p$mean$: p$mean$: p$std$;

stat$mean: Table|  $\sqrt{i/ 100}$  , | i, 1, 27 000| | ;

```

## INITIALIZATION OF RANDOM WALK MODEL

```
(( Graphics`Graphics3D`
(( Graphics`Graphics`
(( Statistics`DataManipulation`

F$T: .8;
$step: 25;
R$sphere : 50;
max$step: $step/ R$sphere;
Result$random$walk: | max$step, max$step| ;
phi$i: Random| Real, | 0, max$step| | ;
step$i: phi$i/ R$sphere;
step$theta$i:  $\sqrt{\$step^2 \cdot step{i}^2}$ ;
th$i: step$theta$i/ R$sphere+ | 1- 2+ Random| Integer| | ;
If| 0! | | Result$random$walk| 1| + th$i| | | , theta$i: th$i, theta$i: - th$i| ;
Result$random$walk: Append| | Result$random$walk| ,
| | Result$random$walk| 1| + theta$i, Result$random$walk| 2| + phi$i| | ;

Last| Result$random$walk| ;
Result$random$walk|| MatrixForm;
rrw: Result$random$walk;
```

## GENERATION OF THE RANDOM WALK OF A MOLECULE IN A BOUNDED SPHERE

```

Result$random$walk: rrw;
For i: 0, Length Result$random$walk ( 10 000, i+1,
  phi$i: Random Real, (. max$step, max$step) | ;
  step$i: phi$i R$sphere;
  step$theta$i:  $\sqrt{\$step^2 \cdot step\$i^2}$ ;
  th$i: step$theta$i/ R$sphere | 1.. 2+ Random Integer | | ;
  If 0: | Last Result$random$walk | 1 | + th$i ( t, theta$i: th$i, theta$i: . th$i) ;
  If .001: | R$sphere Sin Last Result$random$walk | 1 | + theta$i
    + Cos Last Result$random$walk | 2 | + phi$i | ^2 +
    | R$sphere Sin Last Result$random$walk | 1 | + theta$i +
    Sin Last Result$random$walk | 2 | + phi$i | ^2: F$T+ R$sphere^2,
  Result$random$walk: Append Result$random$walk,
    | Last Result$random$walk | 1 | + theta$i, Last Result$random$walk | 2 | + phi$i | | |

xyz$point: Transpose | R$sphere Sin Transpose Result$random$walk | 1 |
  + Cos Transpose Result$random$walk | 2 | | | N, R$sphere
  + Sin Transpose Result$random$walk | 1 | + Sin Transpose Result$random$walk | 2 |
  | | N, R$sphere Cos Transpose Result$random$walk | 1 | | | N | ;

Dimensions Result$random$walk ;
Dimensions xyz$point ;
Length Transpose Result$random$walk | 1 | ;
xyz$point // MatrixForm;

```

**ADDITION OF POISON DISTRIBUTED NOISE TO THE DATA CREATED BY  
RANDOM WALK MODEL**

```
r$xyz={Random[REAL,{-√ Abs Transpose xyz$point | 1, 1| ,
√ Abs Transpose xyz$point | 1, 1| }],Random[REAL,{-
√ Abs Transpose xyz$point | 2, 1| ,√ Abs Transpose xyz$point | 2, 1|
}],Random[REAL,{-√ Abs Transpose xyz$point | 3, 1| ,
√ Abs Transpose xyz$point | 3, 1| }]};
```

```
r$xyz=Append[{r$xyz},{Random[REAL,{-√ Abs Transpose xyz$point | 1, 2| ,
√ Abs Transpose xyz$point | 1, 2| }],Random[REAL,{-
√ Abs Transpose xyz$point | 2, 2| ,√ Abs Transpose xyz$point | 2, 2|
}],Random[REAL,{-√ Abs Transpose xyz$point | 3, 2| ,
√ Abs Transpose xyz$point | 3, 2| }]}];
```

```
For[i=2,i< Length[Transpose[xyz$point]□1[RightDoubleBracket]],i++;
```

```
r$xyz=Append[r$xyz,{Random[REAL,{-√ Abs Transpose xyz$point | 1, i| ,
√ Abs Transpose xyz$point | 1, i| }],Random[REAL,{-
√ Abs Transpose xyz$point | 2, 1| ,√ Abs Transpose xyz$point | 2, 1|
}],Random[REAL,{-√ Abs Transpose xyz$point | 3, 1| ,
√ Abs Transpose xyz$point | 3, 1| }]}];
```

```
XYZ$N: Transpose | Transpose xyz$point | 1| + Transpose r$xyz | 1| ,
      Transpose xyz$point | 2| + Transpose r$xyz | 2| , Transpose xyz$point
      | 3| + Transpose r$xyz | 3| | | ;
xyz$point: XYZ$N;
```



## Appendix E: Lag-Time Analysis

To ensure the observed behavior is due to adsorption. A lag-time analysis was applied to the bleach corrected data. The lag time analysis was developed by Daynes (1920) and Barrer (1951)<sup>179</sup> and is useful to determine the diffusion constant of a species by monitoring stationary and non-stationary flow through a membrane. This technique is similar to the methods discussed in chapter 8 and within this chapter. The lag time approach monitors the concentration profile of a permeating species downstream of a membrane. The solution for a non-adsorbing species as  $t \rightarrow \infty$  is shown here and is discussed in detail by Crank<sup>171</sup>.

$$\text{Equation. E.1} \quad Q_t = \frac{D_\epsilon C_0}{l} \left( t - \frac{l^2}{6D_\epsilon} \right)$$

Where  $D$ ,  $C$ ,  $t$ , and  $l$  have the usual meaning and  $Q_t$  is the mass accumulation as a function of time. By extrapolating the upper part of the  $Q(t)$  down to zero concentration, one is able to ascertain an effective diffusivity from the slope ( $D_\epsilon C_0/l$ ) if the loading concentration and membrane thickness is known. In addition, the time intercept is referred to the lag time ( $l^2/6D_\epsilon$ ). By comparing, the measured diffusivities of the fluorescent concentration breakthrough curve to the time lag analysis one may be able to determine the presence of adsorption within the membrane system.

A modified time-lag analysis proposed by Frisch(1957) suggests that the not only the diffusion constant but also the solubility constant of the diffusant within the membrane system<sup>180</sup>,<sup>181</sup> can be determined. This approach has been utilized several systems such as radon diffusion and solubility constant within membranes<sup>182</sup>, helium diffusion in ptfе tubes<sup>183</sup>. The modified time-lag expression can be derived if Diffusion coefficient is constant in time and if there is a linear relationship between the concentration of the diffusing species and the concentration of the species within the membrane then:

Equation. E.2

$$C' = SC$$

Where  $C'$  is the surface concentration in the membrane,  $C$  is the equilibrium solution concentration and  $S$  is the solubility. By substituting Equation E.2 into Equation E.1, the resulting expression for time-lag accounting for adsorption is:

Equation. E.3

$$Q_t = \frac{D_\epsilon SC_0}{1} \left( t - \frac{l^2}{6D_\epsilon} \right)$$

The following approach was applied by integrating the bleach corrected diffusion breakthrough curves shown calculated from the simultaneous fits with short time solutions, Figure E.1. By applying a best-fit straight line to the upper portion of the curves,

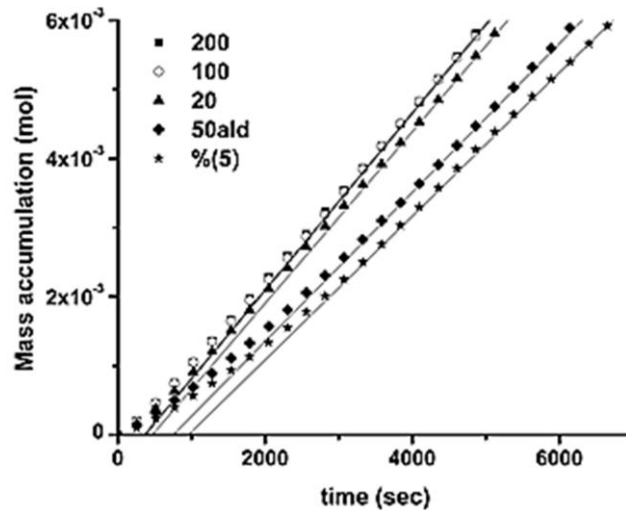


Figure. E.1 Resulting plot of time-lag analysis for short time approximate solutions

both slope and time intercept were determined for each Anodisc measured. The resulting slopes and intercepts were used to calculate the diffusivity coefficients, solubility coefficients, and time intercepts. These values are shown in Table E.1

	200	100	20	50 ALD	100 ALD
Intercept ( $10^{-4}$ )	-4.621	-4.765	-5.802	-8.079	-9.953
slope ( $10^{-6}$ )	1.283	1.28	1.242	1.079	1.04
$R^2$	1	0.99	0.99	0.99	0.99
Lag time = (Intercept /Slope)	360.2	372.3	467.1	748.7	957.0
D ( $m^2/s$ ) x $10^{-13}$	16.6	16.1	12.8	8.01	6.27
S x $10^5$	13.5	14.0	17.1	23.8	29.3

Table. E.1 Summary of the lag time analysis.

The resulting data from the lag time analysis suggests that there is in fact adsorption of fluorescein in the anodic alumina based on the fact that the diffusion coefficients are two orders of magnitude higher than the resulting fit for the short time solution and in fact are in closer agreement to the results from the quasi steady state solution discussed in chapter 8. It is important to note that the solubility coefficients are extraordinarily high for all of the discs; this may be due to poor determination of time zero of the experimental data. It is recommended future studies carefully determine time zero and use a higher sampling rate.

## **BIOGRAPHY OF THE AUTHOR**

Raymond Kennard was born in Norway, Maine on June 28, 1977. He was raised in South Paris, Maine and graduated from Oxford Hills High School in 1995. He attended Ithaca College and graduated in 1999 with a Bachelor's degree in Chemistry. He returned to Maine where he taught Chemistry and Physics at Fryeburg Academy from 1999 to 2003. In fall 2003, he enrolled in the Chemical Engineering graduate program at The University of Maine. After receiving his degree, Raymond will be joining Orono Spectral Solutions, Inc., a private research and development company for development of trace level detection and identification of chemical and biological targets. Raymond is a candidate for the Doctor of Philosophy Degree in Chemical Engineering from The University of Maine in December 2011.